SLAC–PUB–8985
September 2001

Highlights of the SLD Physics Program at the SLAC Linear Collider*

P.C. Rowson and Dong Su

Stanford Linear Accelerator Center, Stanford University, Stanford, California 94309;
e-mail: rowson@slac.stanford.edu, sudong@slac.stanford.edu

Stéphane Willocq

University of Massachusetts, Physics Department, Amherst, Massachusetts 01003;
e-mail: willocq@physics.umass.edu

KEYWORDS: standard model, electroweak, polarization, heavy flavor, CP violation

ABSTRACT: Starting in 1989, and continuing through the 1990s, high-energy physics witnessed a flowering of precision measurements in general and tests of the standard model in particular, led by e^+e^- collider experiments operating at the Z^0 resonance. Key contributions to this work came from the SLD collaboration at the SLAC Linear Collider. By exploiting the unique capabilities of this pioneering accelerator and the SLD detector, including a polarized electron beam, exceptionally small beam dimensions, and a CCD pixel vertex detector, SLD produced a broad array of electroweak, heavy-flavor, and QCD measurements. Many of these results are one of a kind or represent the world's standard in precision. This article reviews the highlights of the SLD physics program, with an eye toward associated advances in experimental technique, and the contribution of these measurements to our dramatically improved present understanding of the standard model and its possible extensions.

*Work supported in part by Department of Energy contract DE-AC03-76SF00515.

CONTENTS

INTRODUCTION 3

THE SLAC LINEAR COLLIDER 6

SLC Operation with Polarized Electron Beams 6

Energy Spectrometers 8

Luminosity Improvements 9

Impact on the SLD Physics Program 10

THE SLD DETECTOR 10

Overall Description 10

The Tracking and Vertexing System 12

The Cherenkov Ring Imaging Detector 17

Polarimetry 17

THE PHYSICS ANALYSIS TOOLS 22

Monte Carlo Simulation 22

Vertexing Algorithm 23

b and c Tagging 24

Hadron Identification 27

Lepton Identification 27

ELECTROWEAK PHYSICS: Z^0 BOSON COUPLINGS 28

Introduction 28

Lepton Couplings 32

Quark Couplings 42

B_s^0–$\overline{B}_s^0$ MIXING 55

Introduction 55

Theory 56

Experimental Ingredients 57

Analysis Methods 57

Results 62

INTERPRETATION OF RESULTS 64

B_s^0–$\overline{B}_s^0$ Mixing 64

Electroweak – Quark Couplings 66

Electroweak – Lepton Couplings 68

CONCLUSIONS 74

1 INTRODUCTION

During the 1990s, experimental particle physics underwent a quiet revolution. Tests of electroweak physics in the standard model (1) to unprecedented precision, in some cases at the part-per-mil level or better, established the standard model as one of the most successful physical theories ever devised. At the center of this activity, starting in 1989, were the experimental programs at the Z^0 boson resonance in e^+e^- colliders at the Stanford Linear Accelerator Center, SLAC [using the SLAC Linear Collider (SLC)], and at the European particle physics laboratory, CERN [home to the Large Electron Positron (LEP) storage ring]. We review highlights of the physics program at the SLC, where a longitudinally polarized electron beam proved to be a particularly powerful tool for Z^0 physics and was critical to an incisive experimental program.

The weak neutral current, and hence the existence of the Z^0 boson, is perhaps the most significant prediction of the electroweak standard model. Maximal parity violation in charged-current weak interactions, implying that the W boson couples only to left-handed fermions, was well established and was incorporated by the architects of the standard model. But unlike the charged W boson, the neutral Z^0 boson couples with both left- and right-handed fermions (with different strengths), and the experimental determination of these couplings reveals much about the details of the theory. In addition, left-handed and right-handed fermions carry different values of a new quantum number, weak isospin, with value $I_W = 1/2$ for left-handed fermions and $I_W = 0$ for right-handed fermions. The left-handed fermions are grouped into weak-isospin doublets, where the upper members (up, charm, and top quarks, and the three neutrinos in the lepton case) carry a weak isospin third component $(I_W)_3 = +1/2$, and the lower members (down, strange, and bottom quarks, and the charged leptons) carry the value $(I_W)_3 = -1/2$. All right-handed fermions are weak-isospin singlets. A consequence of the model is that left- and right-handed fermions behave as different particles, underlining the pivotal role of helicity. The relative strengths of the left- and right-handed couplings to the Z^0 depend on the electroweak mixing parameter, $\sin^2\theta_W$, as follows:

$$g_L = (I_W)_3 - q\sin^2\theta_W \qquad \text{and} \qquad g_R = q\sin^2\theta_W, \tag{1}$$

where q is the electric charge. It is useful to define the linear combinations given by

$$g_V = g_L - g_R \qquad \text{and} \qquad g_A = g_L + g_R, \tag{2}$$

where g_V and g_A then appear as the vector and axial-vector couplings, respectively, in the

neutral-current Lagrangian density,

$$\mathcal{L}_{\rm NC} \sim \overline{\psi}(g_V - g_A\gamma^5)\gamma^\mu\psi Z_\mu. \tag{3}$$

Here ψ and Z_μ are the fermion and Z^0 boson fields. Note that the left-handed and right-handed terms are included, since $(g_V - g_A\gamma^5) = (g_V + g_A)\frac{1}{2}(1-\gamma^5) + (g_V - g_A)\frac{1}{2}(1+\gamma^5)$, explicitly exhibiting the helicity projection operators. The utility of a longitudinally polarized e^- beam for the study of the weak neutral current is clear: With a polarized beam, one can separately generate the two different "particles" e^-_L and e^-_R, and directly measure their couplings to the Z^0 boson.

The relatively large peak cross section (30.5 nb for hadronic final states) at the Z^0 pole, the clean and well-controlled e^+e^- environment, and the universality of Z^0 boson interactions (the Z^0 couples to all known fermions with comparable strength) combine to make an ideal environment for a broad experimental program. As we will demonstrate, when beam polarization is available as it was at the SLC, one has a perfect laboratory for testing the standard model.

At the time of the 1988 International Conference on High Energy Physics (2), direct and indirect data led to an uncertainty on the Z^0 mass of 0.7 GeV, the limit on the number of light Dirac neutrinos was $N_\nu < 6.7$ at a 90% confidence level (CL), the error on the electroweak mixing parameter of the standard model was ± 0.048 from a combination of all available data, the allowed range for the top quark mass was about 50 to 200 GeV, and there was essentially no constraint at all on the standard-model Higgs boson mass (~ 5 GeV $< m_H <$ ~ 1 TeV).

Contrast this situation with the present state of affairs (3): thanks to LEP precision measurements of the Z^0 resonance, the Z^0 mass is known to 2.1 MeV and the Z^0 "invisible" width determines $N_\nu = 2.9841 \pm 0.0083$; the precise measurement of $\sin^2\theta^{\rm eff}_W$, from the SLC Large Detector (SLD) experiment at SLAC and from the LEP experiments at CERN, comes with an error of ± 0.00017. Electroweak data can now be used to predict the top quark mass with remarkable precision ($m_t = 181^{+11}_{-9}$ GeV). In addition, the discovery of the top quark at Fermilab in 1994 and the subsequent determination that $m_t = 174.3 \pm 5.1$ GeV (4), in excellent agreement with the current standard-model prediction, has greatly improved the predictive power of the theory. The standard-model Higgs boson mass is now constrained by the worldwide electroweak data to be < 195 GeV at a 95% CL, where Z^0-pole weak mixing angle results are the leading contributors. Direct searches performed at the higher-energy LEP-II machine constrain this mass to be > 114.1 GeV (5)—hence, the allowed window for the standard-model Higgs has shrunk dramatically.

Table 1: SLD data samples for the various data-taking periods

Year	1992	1993	1994–1995	1996	1997–1998
$Z^0 \rightarrow$ hadrons events	10K	49K	94K	52K	332K
Polarization	22%	63%	77%	76%	73%

The e^+e^- Z^0-pole programs also contributed to significant advances in heavy-flavor (bottom and charm) physics, in particular at the SLC. The unique features of SLC operation led to superlative decay-vertex reconstruction in the SLD detector and to highly efficient identification of the short-lived bottom and charm hadrons. Thanks to the polarized electron beam, the SLC program provides the only direct measurements of parity violation in the bottom and charm neutral-current couplings. Heavy-flavor data from LEP, along with current data on the leptonic neutral-current couplings (coming from SLC and LEP), can be combined with the SLD results. The resulting uncertainties are 2.4% and 1.0% for the vector and axial-vector bottom couplings, and 3.7% and 1.1% for the vector and axial-vector charm couplings. The corresponding results from the 1988 International Conference were one to two orders of magnitude less precise; for example, about 260% and 13% for bottom vector and axial-vector couplings, respectively.

The most impressive marriage of all of the special features of Z^0 physics, linear collider operation, sophisticated detector instrumentation, and beam polarization is evident in the study of B_s^0–$\overline{B}_s^0$ mixing at the SLC. These measurements are sensitive to the details of quark mixing, which are parameterized by the Cabibbo-Kobayashi-Maskawa (CKM) mixing matrix (6) in the standard model. These data significantly constrain one of the least-known elements of the CKM matrix and thereby contribute to our understanding of CP violation. The B_s^0–$\overline{B}_s^0$ mixing measurements were also performed at LEP with comparable precision owing to the much larger event totals of these experiments. The 1988 International Conference predated these first successful B_s^0–$\overline{B}_s^0$ mixing results, but it is safe to say that the quality of the initial- and final-state heavy-flavor identification and the decay vertex resolutions achieved at the Z^0, particularly at the SLC, were not anticipated.

The SLD collaboration collected data at the SLC during the period 1992–1998. Table 1 shows a breakdown of the data samples, along with the average electron beam polarization at the interaction point. Since 1996, data were recorded with the upgraded vertex detector VXD3 (see Section 3.2). In what follows, we summarize the highlights of the physics program in precision electroweak measurements and heavy-flavor physics. The reader is referred to published work

for studies of τ (7) and QCD (8) physics at SLD.

2 THE SLAC LINEAR COLLIDER

The SLC is, so far, the only e^+e^- linear collider. Consequently, the SLC/SLD program was both a particle physics experiment and an accelerator R&D project, and key features of these parallel activities were closely intertwined. A linear collider is a "single-pass" device—the e^+ and e^- bunches are generated anew for every single collision—and hence the operation of the SLC introduced technical challenges in the control of bunch trajectory, intensity, energy, and focusing not common to the more forgiving storage ring design. Commissioning of the machine began in 1987 and lasted about two years. The SLC luminosity was initially far below expectations, although the brief Mark II physics program (1989–1990) (9) produced some important early results before being eclipsed by the much higher-luminosity LEP e^+e^- storage ring. A breakthrough for the SLC came in 1992, when a longitudinally polarized ($\sim 25\%$) electron beam first became available. Because of advances in photocathode technology, the electron beam polarization was increased to $\sim 75\%$ by 1994. Over the years, the luminosity of the machine improved steadily, most dramatically during the final run (1997–1998), when a peak of about 3×10^{30} cm^{-2}s^{-1} was reached and roughly 70% of the entire SLD dataset was accumulated.

The cornerstone of the SLC program at the Z^0 pole was the polarized electron beam, which proved essential not only for precision electroweak measurements but for most heavy-flavor physics as well. The basic operation of the SLC is described below, where we highlight features most relevant to the SLD physics, particularly polarized beam production and transport. More complete descriptions are available in an earlier review (10) and in a more recent technical report (11).

2.1 SLC Operation with Polarized Electron Beams

Figure 1 illustrates the basic layout of the SLC. The machine produced e^+e^- collisions at a repetition rate of 120 Hz. Longitudinally polarized electrons were produced by illuminating a GaAs photocathode with a circularly polarized Ti-Sapphire laser (12). Since the advent of high-polarization "strained lattice" GaAs photocathodes in 1994 (13), where mechanical strain induced in a thin (0.1 μm) GaAs layer lifts an angular-momentum degeneracy in the valence band of the material, the average electron polarization at the e^+e^- interaction point (slightly lower than the value produced at the source) was in the range 73% to 77%. Corresponding values were about 22% in 1992 using an unstrained "bulk" GaAs cathode, and 63% in 1993 using a

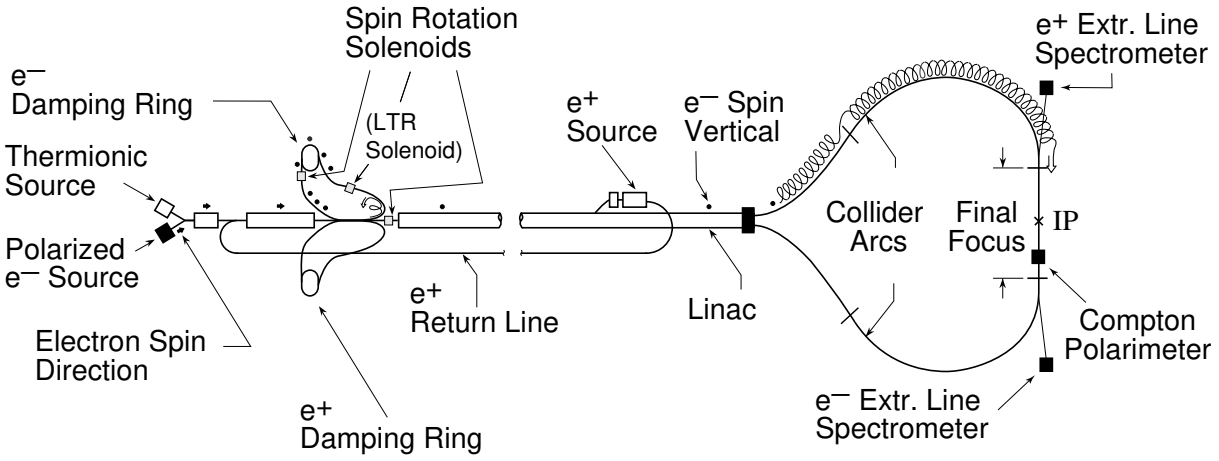

Figure 1: Layout of the SLC.

thicker (0.3 μm) strained layer cathode design. The electron helicity was chosen randomly pulse to pulse at the machine repetition rate of 120 Hz by controlling the circular polarization of the source laser. This pulse randomization minimized unwanted correlations between the pulse helicity and other periodic phenomena in the accelerator, as well as in the SLD and polarimeter data. On each SLC cycle, two closely spaced (61 ns) electron bunches were produced, the second of which was used to produce the positrons.

The electron spin orientation was longitudinal at the source and remained longitudinal until the transport to the damping ring (DR). In the linac-to-ring (LTR) transport line, the electron spins precessed in the dipole magnets, where the spin precession angle is given in terms of the anomalous magnetic moment g:

$$\theta_{\text{precession}} = \left(\frac{g-2}{2}\right)\frac{E}{m}\,\theta_{\text{bend}}. \tag{4}$$

By design, the bend angle θ_{bend} resulted in transverse spin orientation at the entrance to the LTR spin rotator magnet. This superconducting solenoid magnet was used to rotate the polarization about the beam direction into the vertical orientation for storage in the DR. This was necessary because any horizontal spin components precessed rapidly and net horizontal polarization completely dissipated during the 8.3 ms (1/120 s) storage time owing to energy spread in the bunch. In addition, the polarized electron bunches could be stored in one of two possible configurations by reversing the LTR spin rotator solenoid magnet. These reversals, typically done every three months, were useful for identifying and minimizing the small $[\mathcal{O}(10^{-4})]$ polarization asymmetries produced at the source.

The product of the horizontal and vertical emittances of the electron (positron) bunches, a measure of the transverse phase-space of the beam, was reduced in the DR by a factor of roughly

100 (1000). One of two stored positron bunches was extracted from the positron DR and led the two electron bunches down the linac, the bunches spaced by 61 ns. The second electron "scavenger" bunch was diverted to the positron target after 30 GeV of acceleration. Positrons produced at the target were accelerated to 200 MeV for transport via the positron return line to the positron DR, where they were stored for 16.6 ms. The remaining e^- and e^+ bunches continued down the linac and reached ~ 46.5 GeV. They were then transported through the arcs (energy loss of about 1 GeV occured in the arcs owing to synchrotron radiation) and final focus to the interaction point (IP). Following the IP, the bunches entered the extraction lines where their energies were measured by precision spectrometers, after which they were transported to beam dumps.

After leaving the DR, the electrons were accelerated in the linac with their polarization oriented vertically, and brought into the SLC north arc. The electron spin orientation was manipulated in the north arc (see Figure 1) using controllable betatron oscillations (known as "spin bumps") to achieve longitudinal polarization at the IP. This was possible because the betatron phase advance closely matched the spin precession (1080° and 1085°, respectively) in each of the 23 bending-magnet assemblies ("acromats") used in the arc —and hence the north arc operated close to a spin-tune resonance. As a result, excepting 1992 running, the two additional SLC spin rotator solenoids were not necessary for spin orientation and were used only in a series of specialized polarization experiments. This unanticipated simplification had an additional benefit. In order to achieve higher luminosity, starting in 1993 the SLC was operated with "flat beams" ($\sigma_x > \sigma_y$), a setup that would have been precluded by the spin rotators because x-y coupling in the ring-to-linac spin rotator would have spatially rotated the electron bunches.

2.2 Energy Spectrometers

The SLC employed a pair of energy spectrometers (14) located in the electron and positron extraction lines (see Figure 1). Beam deflection, and therefore beam energy, was measured from the spatial separation of synchrotron radiation emitted by the beam in deflector magnets located before and after a precision dipole magnet. These two spectrometers together nominally measured the e^+e^- collision energy with a precision of 20 MeV. The importance of the energy measurement and some details concerning spectrometer precision are discussed in Section 5.2.

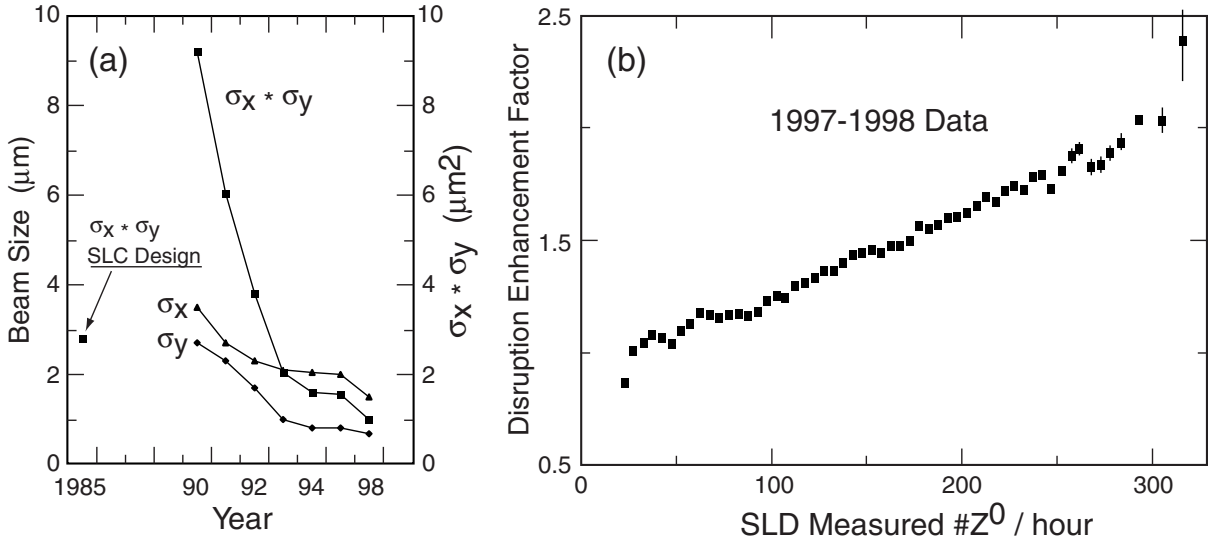

Figure 2: (*a*) Horizontal (σ_x) and vertical (σ_y) beam spot sizes, as well as the cross-sectional area ($\sigma_x \cdot \sigma_y$) of the beam as a function of time. The original design value for the area is also shown. (*b*) Luminosity enhancement due to beam-beam disruption.

2.3 Luminosity Improvements

The luminosity $\mathcal{L}$ of a linear collider is given by

$$\mathcal{L} = \frac{N^+ N^- f}{4\pi\sigma_x\sigma_y} H_d, \tag{5}$$

where $N^\pm$ are the number of positrons and electrons in each bunch at the IP, f is the collision repetition rate, and $\sigma_{x,y}$ are the average horizontal and vertical beam sizes. The additional parameter H_d is a disruption enhancement factor that is a function of $N^\pm$ and the transverse and longitudinal beam dimensions, and for moderate beam intensities H_d is equal to one.

The route to high luminosity at the SLC was somewhat different than originally conceived, with a greater emphasis on reduced beam size (design performance was exceeded by about a factor of three) because the maximum bunch size was limited to about 4×10^{10} due to wakefield effects and DR instabilities (7×10^{10} was indicated in the initial plans). In the final focus, the e^+e^- transverse bunch dimensions were demagnified to about 1.5 μm in x and 0.7 μm in y for collision at the IP. Figure 2*a* shows the historical trend in the size of the SLC beams. A consequence of the very small SLC beam sizes at the IP was that a significant luminosity enhancement due to beam-beam disruption ($H_d > 1$) was observed at the highest luminosities. From a comparison between the luminosity measured with the SLD luminosity monitor and that computed from Equation 5 with $H_d = 1$, enhancements of up to a factor of two were seen, as

shown in Figure 2*b*.

Though not directly relevant to our discussion of the SLD physics program, one important feature of SLC operation deserves mention. Producing and maintaining the small beam emittances required for these very small spot sizes, and sustaining their collisions, all on a pulse-to-pulse basis, was challenging. An important lesson was that a linear collider is an inherently unstable machine and extensive feedback systems are indispensable. In particular, the importance of fast feedback (at the 120 Hz machine repetition rate) became apparent. By the end of the SLD program in 1998, the SLC featured over 50 feedback systems controlling 250 machine parameters. These features included intensity feedback at the source, energy feedback, linac orbit feedback, and an elaborate collision optimization system that modulated five final focus corrections for each beam while monitoring a direct measure of luminosity (beamstrahlung).

2.4 Impact on the SLD Physics Program

Three features of the SLC contributed to the unique capabilities of the SLD physics program. Most important was the polarized electron beam. The SLC achieved a precise determination of the weak mixing angle with more than 30 times the sensitivity per Z^0 event of any competing method at LEP and with smaller systematic error. The beam also enabled a number of the world's best measurements in heavy-quark electroweak physics, partly through the greatly enhanced statistical power and simplicity afforded by polarization. Second, the small size of the luminous region at the collision point, smaller in the transverse (x,y) and longitudinal (z) dimensions than at LEP by factors of typically 100, 4, and 10, respectively, allowed for excellent localization of the primary vertex in reconstructed Z^0 decays. Finally, the low repetition rate of the SLC (120 Hz compared with 45 kHz at LEP), a liability insofar as luminosity is concerned, permitted the use of charge-coupled device (CCD) sensors with inherently long readout times in the SLD vertex detector, a device that subsequently set the world standard for precision in decay-length reconstruction. All these issues are addressed in more detail in our discussion of physics results.

3 THE SLD DETECTOR

3.1 Overall Description

The SLD was a general-purpose device (15) covering most of 4π sterradians (sr). It was optimized for physics at the Z^0 resonance, i.e., it was designed for the reconstruction and identification of

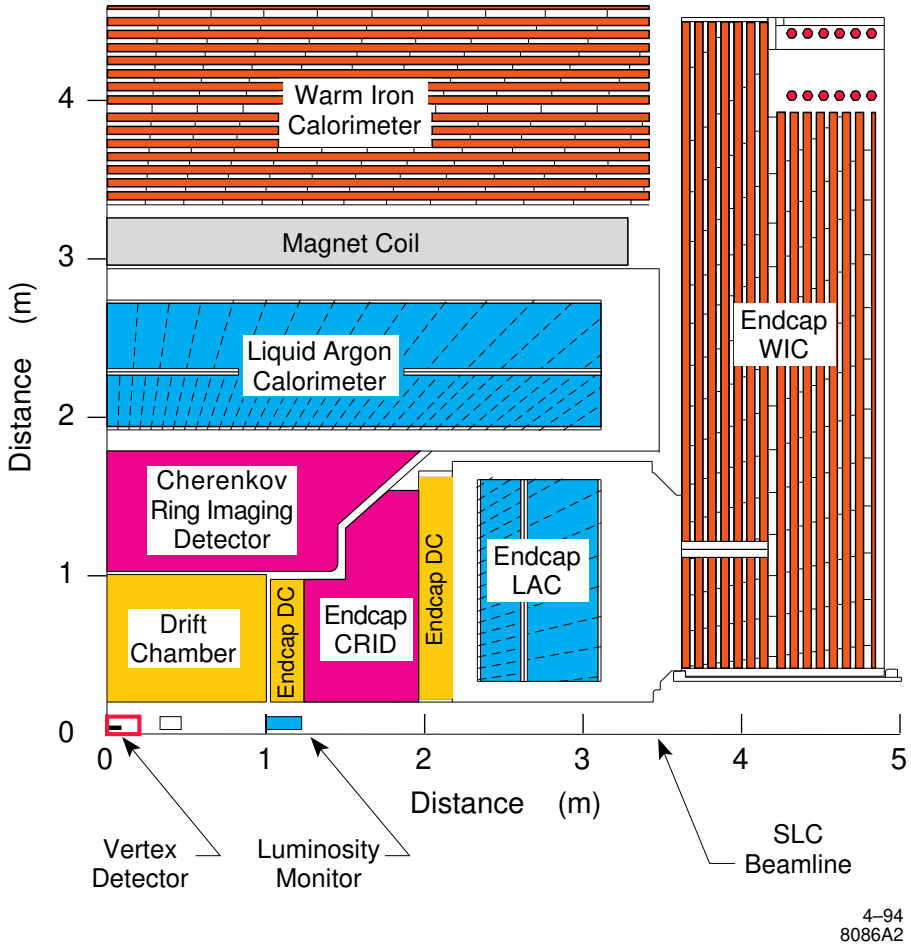

Figure 3: Side view of one quadrant of the SLD detector.

particles in a momentum range of several hundred MeV/c up to nearly 50 GeV/c. The detector consisted of multiple concentric layers (see Figure 3). In the following, we refer to a right-handed coordinate system with a z-axis along the e^+ beam direction and a y-axis along the vertical direction.

Precision charged-particle tracking was performed with the CCD pixel Vertex Detector (VXD) surrounded by the Central Drift Chamber (CDC). Outside the tracking systems, the Cherenkov Ring Imaging Detector (CRID) identified the charged hadrons π, K, and p, and the Liquid Argon Calorimeter (LAC) provided electromagnetic and hadronic calorimetry as well as electron identification (and muon identification to a lesser extent). These systems were contained inside a large solenoid producing a 0.6 T axial magnetic field. Finally, the Warm Iron Calorimeter (WIC) served as the magnet flux return yoke and identified muons. In the following, we describe the calorimetry systems and devote separate sections to the tracking, particle identification, and polarimetry systems.

The main calorimeter was the lead–liquid argon sampling calorimeter (16), which satisfied the design requirements for hermiticity (it covered 98% of 4π sr), good energy and position resolution, and good uniformity of response to electromagnetic and hadronic showers. To provide information on longitudinal shower development, the LAC was divided radially into two separate electromagnetic sections totaling 21 radiation lengths and two hadronic sections totaling 2.8 interaction lengths. Energy resolution was measured to be $\sigma/E = 0.15/\sqrt{E(\mathrm{GeV})}$ for electromagnetic showers and estimated to be $\sigma/E = 0.60/\sqrt{E(\mathrm{GeV})}$ for hadronic showers. The LAC was placed inside the magnet coil to minimize the amount of material in front of the calorimeter, thus achieving good resolution down to low energies. Finally, the LAC was used to trigger the data acquisition system and, in conjunction with the drift chamber, to identify electrons.

Outside the magnet coil stood the WIC (17), a coarsely sampled iron-gas calorimeter operated in limited streamer mode, which was designed to catch the remaining $\sim 15\%$ of hadronic energy leaking out from the LAC. Its main use, however, was as a muon tracking and identification device. The material in the WIC amounted to four interaction lengths, which, in addition to the 2.8 (0.7) interaction lengths from the LAC (magnet coil), gave a total of over seven interaction lengths for particles traversing the whole detector from the IP.

A third calorimeter system (18), made of tungsten and silicon pads, detected electromagnetic showers at small angle with respect to the beam line: $28 < \theta < 68$ mrad. The purpose of this system was to monitor the SLC luminosity.

3.2 The Tracking and Vertexing System

3.2.1 The Central Drift Chamber

The CDC (19) had a cylindrical geometry with a length of 1.8 m, extending radially from 0.2 m to 1.0 m. It consisted of ten superlayers, four coaxial to the beam, interleaved with pairs of superlayers having stereo angles of ± 41 mrad. Each superlayer consisted of cells 50 mm along the radius (r) and ~ 59 mm wide in azimuth (ϕ) at the midpoint. Each of the cells contained eight sense wire layers. An average spatial resolution of $82\,\mu$m was obtained with a gas of CO_2 : argon : isobutane in the ratio of 75% : 21% : 4%, respectively. The azimuthal and polar angle resolutions on the track direction at the inner radius of the CDC were 0.45 mrad and 3.7 mrad, respectively, for high-momentum tracks. The momentum resolution of combined CDC+VXD tracks in the central region ($|\cos\theta| < 0.7$) was $\frac{\sigma p_T}{p_T} = 0.010 \oplus 0.0024\, p_T$, where p_T is the momentum transverse to the beam axis, measured in GeV/c.

3.2.2 The CCD Vertex Detector

The detection of short-lived particles using vertex detectors has played a vital role in the advance of our understanding of flavor physics. In the LEP/SLC era in particular, the usage of vertex detectors extended beyond the traditional field of heavy-flavor decay physics and became an important tool for electroweak and QCD physics, as well as for new particle searches. The low beam-crossing rate of the SLC compared with the circular colliders offered an opportunity for using CCDs as the basic vertex detector elements. Some of the main advantages over silicon-strip vertex detectors employed at LEP are as follows:

- The SLD vertex detector was a factor of two closer to the beam line, which was crucial for reducing track errors due to extrapolation and multiple scattering.
- The genuine three-dimensional nature of CCD pixel hits led to fewer tracking hit misassignments. In contrast, double-sided silicon-strip detectors yield uncorrelated ϕ and z hits, which result in a quadratic increase in hit ambiguity.
- The spatial resolution provided by the SLD CCD pixel segmentation was better by a factor of two.
- The active silicon layer of the CCDs was typically 15 times thinner than that in silicon-strip detectors. This feature largely prevented the drastic z-resolution degradation at shallow polar angles that is inevitable for silicon strips. It also allowed for thinner detectors to reduce multiple scattering.

The first version of the SLD CCD vertex detector (VXD2) (20) was installed in late 1992. Its reliable operation and impressive performance inspired the design of an upgraded vertex detector (VXD3) (21), with a more optimized geometry, improved coverage, and reduced material. This detector was operational starting in 1996 and hence for the majority of the SLD data sample. VXD3 consisted of 48 "ladders," each containing two 8×1.6 cm custom-made CCDs. The ladders were arranged in three cylindrical layers (see Figure 4) at radii of 2.7, 3.8, and 4.8 cm respectively, covering $|\cos\theta| < 0.85$ with three layers and $|\cos\theta| < 0.90$ with two layers. The entire detector was supported by a beryllium structure and operated at 190 K using nitrogen gas cooling. The CCDs were thinned to 200 μm and supported by a beryllium motherboard so that the material per layer for normal incidence was 0.40% of a radiation length. The beryllium beam pipe and inner gas shell added 0.52% radiation length of material inside the VXD.

Each VXD3 CCD contained 800×4000 pixels that were 20 μm×20 μm in size, and the active silicon depth was also 20 μm. VXD3 was continuously read out at a rate of 5 MHz and the entire

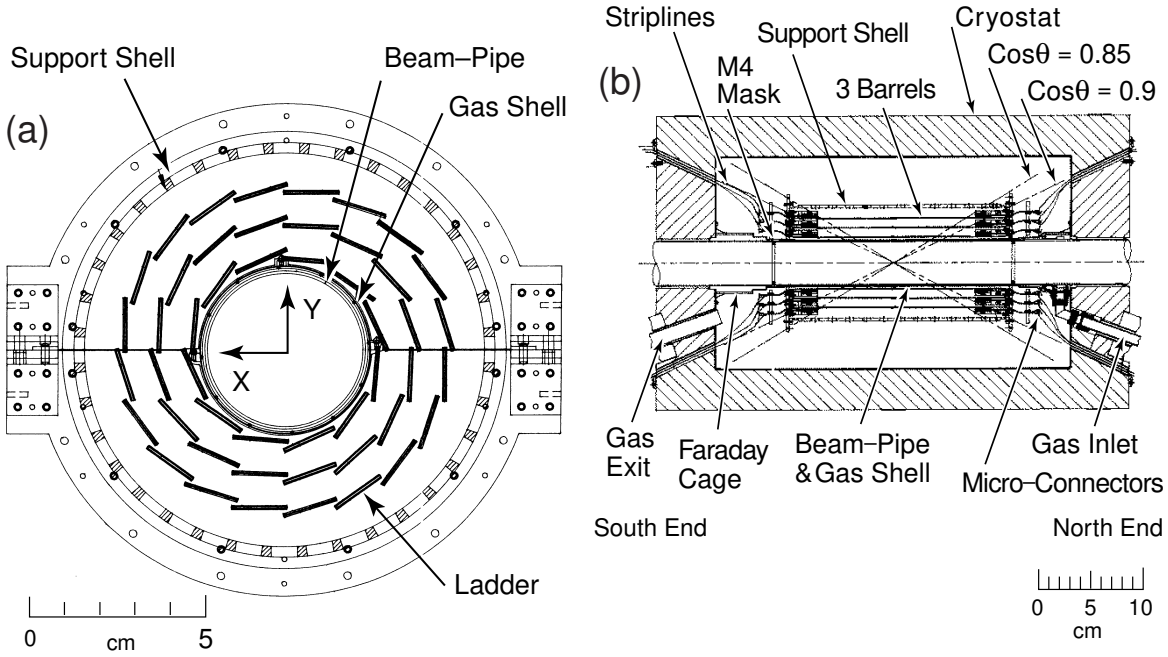

Figure 4: Layout of VXD3 and mechanical support structure showing (a) cross-section view; (b) longitudinal section view.

detector took 200 ms (25 SLC beam crossings) to read out. The electronic noise per pixel was 55 electrons, compared with the most probable energy loss of 1200 electrons for minimum ionizing particles, typically spread over 4–5 pixels. The cluster centroid positions were calculated using the measured ionization charge accumulated in each pixel. The average single-hit efficiency was over 99.5% for the data taken since 1997; the remaining inefficiency mainly came from a small number of faulty electronic channels during limited time periods. The average efficiency for the 1996 data sample was ∼2% worse because of early electronics problems and radiation damage effects, which were cured in 1997–1998 by operating at a lower temperature.

The VXD3 geometry was designed with careful consideration for track-based alignment, with CCD overlaps in z on the same ladder and in ϕ between adjacent ladders in the same layer. The CCD shape distortions were first corrected based on optical survey data. The CCD positions, fully described by three translations and three rotations, were subsequently determined using a track-based internal alignment. This alignment also included long-range constraints from $Z^0 \to e^+e^-$ and $Z^0 \to \mu^+\mu^-$ events. The average single-hit spatial resolution was 3.5 μm in the r-ϕ plane for all polar angles and 3.7 μm (5.7 μm) in the r-z plane for tracks with $|\cos\theta| < 0.6$ ($0.6< |\cos\theta| <0.85$). The resolution degradation in z at high $|\cos\theta|$ was partly due to some residual errors in the CCD shape distortion corrections.

The central beam pipe and VXD assembly was mechanically supported from the CDC. Its mechanical coupling to the rest of the beam line was reduced by a factor of ten with a set of bellows separating out the central section. This loose coupling provided a very stable relative position of the VXD with respect to the CDC, at the level of a few microns, during long periods of operation. Global alignment between VXD and CDC was necessary only after major detector accesses.

3.2.3 Tracking Performance

The tracking algorithm first reconstructed three-dimensional track segments in the VXD with three or more hits and $p_T > 80\,\mathrm{MeV}/c$. These VXD track segments were then extrapolated to the CDC to search for CDC hits to form tracks. On the second pass, the tracks found with the remaining CDC hits not used by the first-pass tracks were extrapolated into the VXD to search for hits; at least two VXD hits were required. All pattern-recognized tracks were subject to a Kalman fit (22) to determine the track parameters, taking into account multiple scattering effects. The SLC beam caused a VXD background hit density of 2–7 hits/ cm^2 depending on the CCD layer and ϕ position. This occupancy turned out to be quite manageable thanks to the extremely fine granularity of the CCD pixels. For "prompt" tracks in hadronic events, the CDC+VXD full tracking efficiency was 96%. Prompt tracks are defined as tracks that originate from the IP or from heavy hadron decays with $p_T > 400$ MeV/c and $|\cos\theta| < 0.85$, and neither decayed nor interacted before exiting the CDC.

Among the prompt tracks with full CDC+VXD information, 97.8% had three or more VXD hits, and 99.8% had all VXD hits correctly assigned. The VXD track segments without a CDC link were used to improve vertex charge determination. Despite the rather short radial span (~ 2 cm), the charge was correctly determined for 90% of the VXD track segments up to $1.5\,\mathrm{GeV}/c$ ($3.5\,\mathrm{GeV}/c$) without (with) a vertex constraint.

The track impact parameter resolution can be roughly parameterized as $\sigma_{r\phi} = 7.7 \oplus \frac{33}{p\sin^{3/2}\theta}$ μm and $\sigma_{rz} = 9.6 \oplus \frac{33}{p\sin^{3/2}\theta}$ μm, where p is the track momentum, measured in GeV/c. The constant terms were determined from a study of two-track miss-distance distributions near the IP in $Z^0 \to \mu^+\mu^-$ events, see Figure 5. This resolution performance is a factor of two better than the best LEP detectors in both the constant and multiple scattering terms.

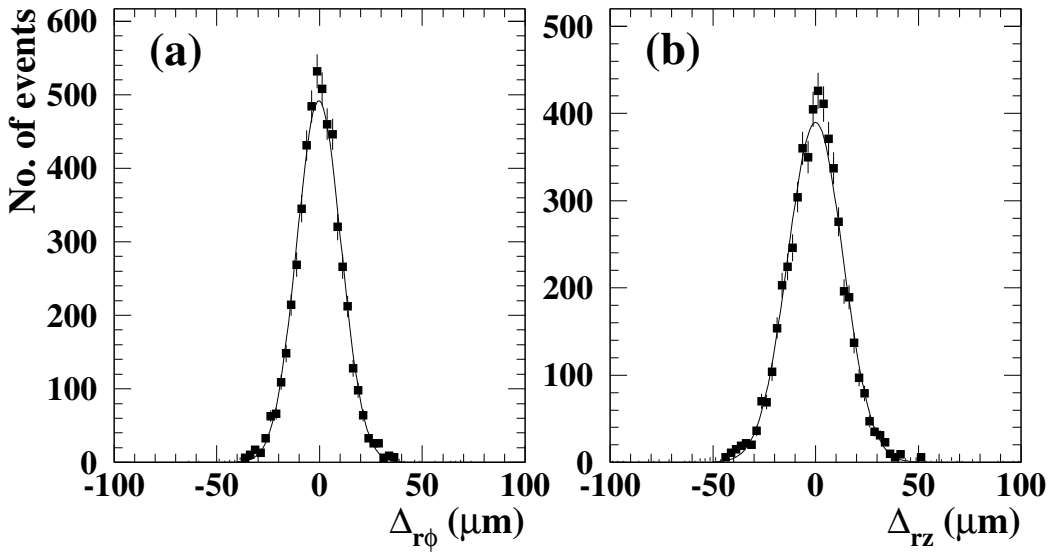

Figure 5: Two-track miss-distance distributions for $Z^0 \to \mu^+\mu^-$ events: (*a*) r-ϕ miss-distance; (*b*) r-z miss-distance.

3.2.4 The SLC Interaction Point

To achieve the best identification of secondary vertices from heavy-flavor decays, the primary vertex resolution is crucial. To enable the micron-sized SLC beams to collide, it was essential to maintain a stable IP. For this reason, the average beam position in the x-y plane is a very good estimate of the event primary vertex. In the e^+e^- storage ring experiments, the beam spot in y is also fairly narrow (a few to $10\,\mu$m), but the beam size in x is typically $100\,\mu$m or more, so that event-by-event reconstruction of the primary vertex x position was required. This typically resulted in a primary vertex x resolution > 20 μm for LEP experiments. The average SLC beam position in the x-y plane was determined from ∼30 consecutive hadronic events by fitting all tracks coming from a common origin. The resolution of the beam position determination was found to be $\sigma_{xy} = 3.5$ μm using the impact parameter distribution of tracks in $Z^0 \to \mu^+\mu^-$ events. This resolution was the result of the combined effect of beam jitter and tracking resolution.

The event primary vertex in z was measured event by event owing to the large luminous region along the beam axis (∼$700\,\mu$m). The z position of the primary vertex was determined from the median of the z-coordinate distribution for all tracks consistent with the IP in the x-y plane. This simple approach was found to be particularly stable against track impact parameter resolution tails. The event primary vertex z resolution for (uds, c, b) events was estimated to be (10,11,17) μm.

3.3 The Cherenkov Ring Imaging Detector

The CRID covered the region $|\cos\theta| < 0.68$. To perform $\pi/K/p$ separation over the full momentum range of interest ($\sim$0.2 to 45 GeV/c), two different radiators were used (23). The liquid C_6F_{14} radiator identified particles in the lower portion of the momentum range, whereas the gas $C_5F_{12} + N_2$ radiator covered the higher end of the range. Thresholds for emission of Cherenkov radiation in the liquid (gas) were 0.17 (2.4) GeV/c for $\pi^{\pm}$, 0.62 (8.4) GeV/c for $K^{\pm}$, and 1.17 (16.0) GeV/c for protons. Cherenkov photons emitted in a cone around the charged-particle trajectory were focused onto an array of 40 time projection chambers (TPCs) filled with ethane and $\sim 0.1\%$ tetrakis dimethylamino ethylene (TMAE) which served as the photosensitive agent. The three-dimensional location of each photoelectron conversion was recorded in the TPCs and the production angle relative to a given charged track was reconstructed. For typical $\beta \simeq 1$ particles passing through the liquid (gas) radiator, an average of 12.8 (9.2) photons were detected per full ring and the Cherenkov angle resolution was measured to be 16 (4.5) mrad.

3.4 Polarimetry

In Compton scattering of longitudinally polarized electrons from circularly polarized photons, the differential cross section in terms of the normalized scattered photon energy fraction x is given by

$$\frac{d\sigma}{dx} = \frac{d\sigma_0}{dx}[1 - \mathcal{P}_\gamma \mathcal{P}_e A(x)], \tag{6}$$

where $\frac{d\sigma_0}{dx}$ is the unpolarized differential cross section, $\mathcal{P}_\gamma$ and $\mathcal{P}_e$ are the photon and electron polarizations, and $A(x)$ is the Compton asymmetry function. The asymmetry arises from the difference between cross sections for parallel and anti-parallel spins ($\sigma_{j=3/2} > \sigma_{j=1/2}$), and is defined in the usual way as the cross-section difference divided by the sum of the two cross sections. In a polarimeter, the Compton-scattered photons or electrons are detected, and the requisite instrumental effects are incorporated into a detector response function. The normalized convolution of $A(x)$ with $\frac{d\sigma_0}{dx}$ and the response function (all functions of x) is the "analyzing power." When $\mathcal{P}_\gamma$ and the analyzing power are known, the experimental determination of the $j = 3/2$ to $j = 1/2$ scattering asymmetry determines $\mathcal{P}_e$ and hence the utility of this elementary QED process to electron polarimetry.

The SLD precision Compton polarimeter detected beam electrons that had been scattered by photons from a circularly polarized laser. The choice of a Compton-scattering polarimeter was dictated by the requirements that the device be operated continually while beams were in collision and that uncertainties in the physics of the scattering process not be a limiting factor

in the systematic error—both are troublesome issues for Møller scattering instruments because of their magnetic foil targets. The pulse-to-pulse controllability of the laser polarization, as well as the high polarization (99.9%), are additional advantages over other options.

Figure 6 illustrates the essential features of the polarimeter: Frequency-doubled (532 nm) Nd:YAG laser pulses of 8 ns duration and peak power of typically 25 MW were produced at 17 Hz, circularly polarized by a linear polarizer and a Pockels cell pair. The laser beam was transported to the SLC beam line by four sets of phase-compensating mirror pairs and into the vacuum chamber through a reduced-strain quartz window. About 30 m downstream from the IP, the laser beam was brought into collision with the outgoing electron beam (10 mrad crossing angle) at the Compton interaction point (CIP) and then left the beam pipe through a second window to an analysis station. The pair of Pockels cells on the optical bench allowed for full control of elliptical polarization and was used to automatically scan the laser beam polarization at regular intervals in order to monitor and maximize laser polarization at the CIP. Downstream from the CIP, a pair of bend magnets swept out the off-energy Compton-scattered electrons (typically of order 1000 per laser pulse) that passed through a thin window out of the beam-line vacuum and into a nine-channel (1 cm per channel) transversely segmented gas Cherenkov detector. By detecting scattered electrons with a threshold Cherenkov device, the large beamstrahlung backgrounds in the SLC environment were dramatically reduced.

The minimum-energy 17.4 GeV electrons, corresponding to full backscattering, generally fell into the seventh detector channel. At this point in the electron spectrum, known as the Compton edge, the energy-dependent Compton asymmetry function reached its maximum value of 0.748. Small deviations from the theoretical asymmetry function (of order 1% in channel 7) were modeled using an electromagnetic shower simulation (24) in a detailed model of the detector geometry and the magnetic spectrometer (25). The detector was mounted on a movable platform and the Compton edge was scanned across several channels at regular intervals in order to monitor its location and to experimentally determine the detector channel response functions. This procedure was essential for the precise determination of the analyzing power of the important outer channels. Figure 7 presents data showing the corrected Compton asymmetry, as well as the magnitude of the correction, as a function of position and scattered electron energy. There is good agreement between the corrected asymmetry and the data in each channel.

Starting in 1996, two additional polarimeters (26), which detected the Compton-scattered photons and which were operated in the absence of positron beam due to their sensitivity to beamstrahlung backgrounds, were used to verify the precision polarimeter calibration. These

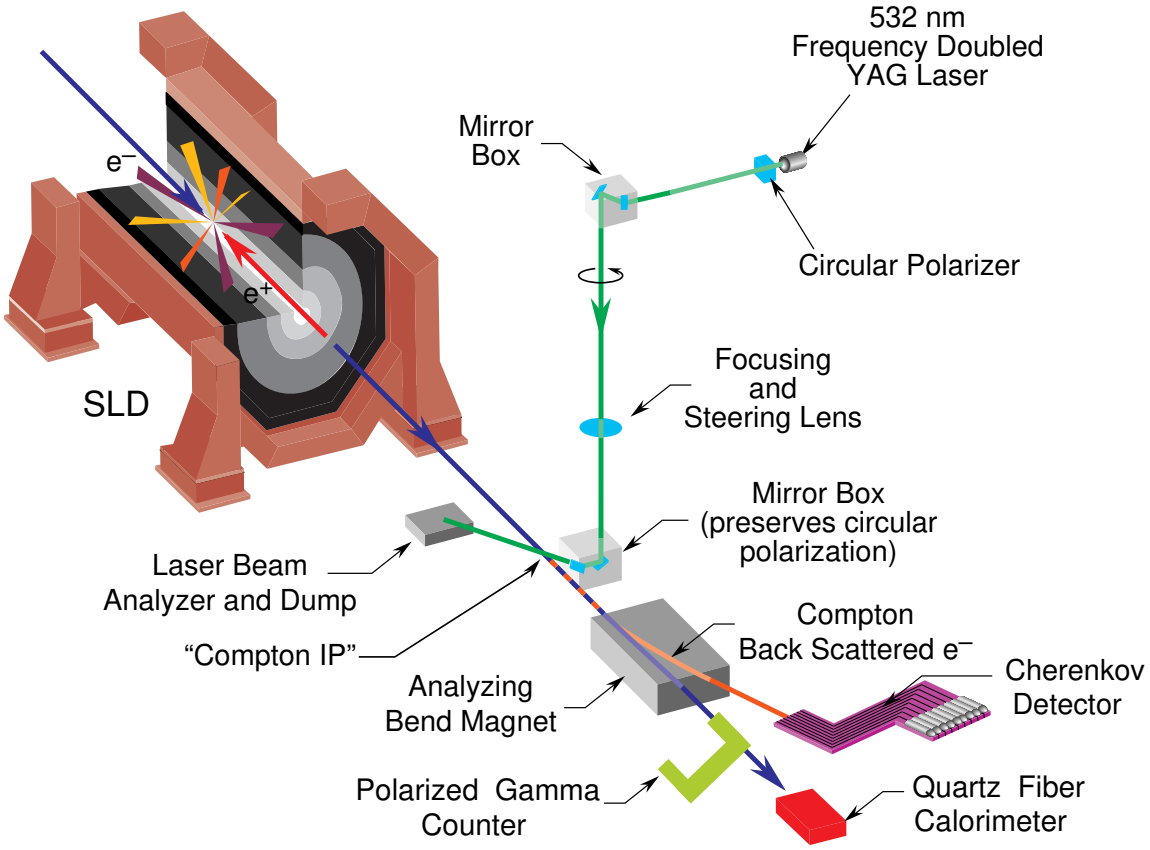

Figure 6: A conceptual diagram of the SLD Compton polarimeter.

two devices were of different design (one employed a gas Cherenkov detector and the other a quartz-fiber calorimeter) with different systematic errors, and they had in common with the primary electron polarimeter only the instrumental errors due to the polarized laser. The cross-check provided by these photon detectors was used to establish a calibration uncertainty of 0.4%. Table 2 summarizes the systematic uncertainties in the polarization measurement. During the period 1992–1998, the total fractional systematic error decreased from 2.7% to its final value of 0.50%, with the most significant reductions coming from greatly improved understanding of the laser polarization and the Cherenkov detector nonlinearity. The dominant error is now due to the analyzing power calibration discussed above.

The polarimeter result was corrected for higher order QED and accelerator-related effects (a total of $-0.22\pm0.15\%$ for 1997–1998 data). The higher-order QED offset was very small and well-determined (-0.1%) (27). The primary accelerator-related effect arose from energy-polarization correlations that caused the average beam polarization measured by the Compton polarimeter to differ slightly from the luminosity-weighted average beam polarization at the IP. In 1994–1998,

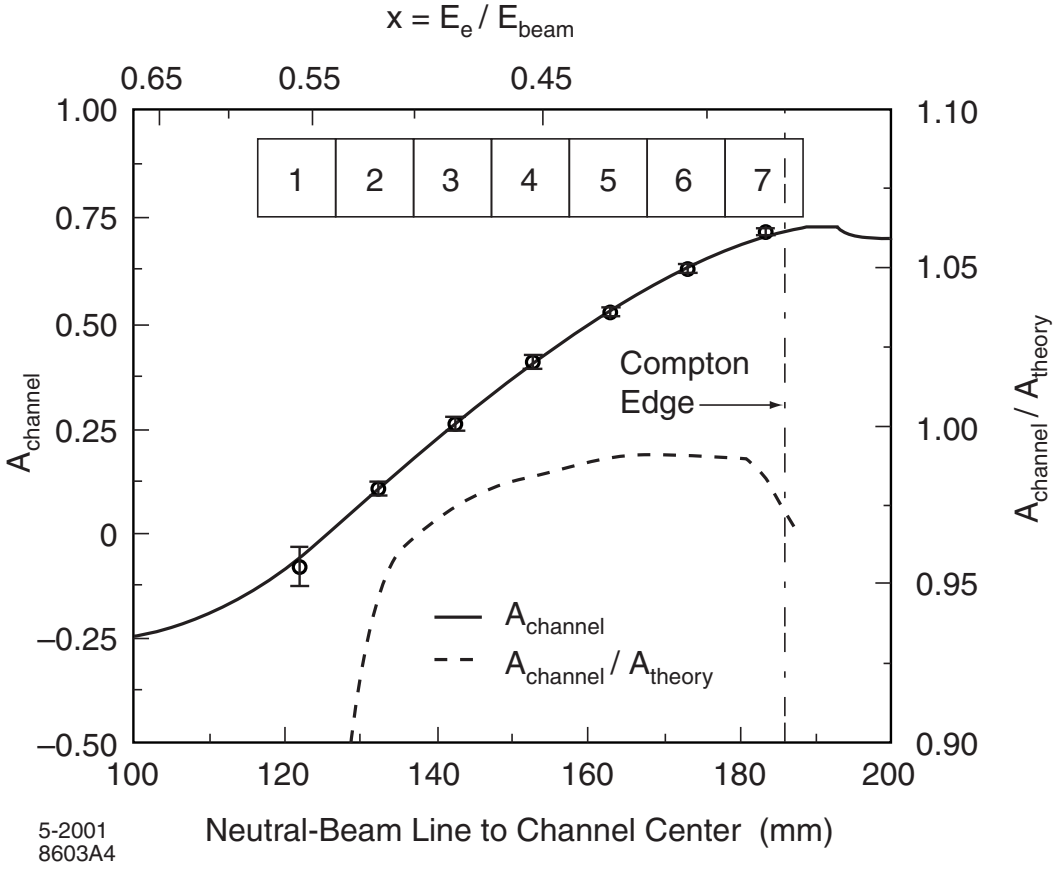

Figure 7: Compton scattering asymmetry as a function of channel position. The horizontal axis gives the distance in mm from the center of the detector channels (1 cm wide each) to the path of the hypothetical undeflected electron beam (neutral-beam line). The inset shows the seven inner detector channels, sized to match the horizontal scale. The per channel data are plotted as open circles, and the corrected asymmetry function is the solid curve. The size of the correction from the theoretical QED calculation is indicated by the dashed curve.

a number of measures in the operation of the SLC and in monitoring procedures (smaller and better-determined beam energy spread and polarization energy dependence) reduced the size of this chromaticity correction and its associated error from its value of $1.1 \pm 1.7\%$ when it was first observed in 1993 to below 0.2%. An effect of comparable magnitude arose from the small precession of the electron spin in the final focusing elements between the SLC IP and the CIP. The contribution of depolarization during collision was determined to be negligible, as expected, by comparing polarimeter data taken with and without beams in collision. All effects combined yielded a correction with the uncertainty given in Table 2.

Table 2: Compton polarimeter systematic errors on the beam polarization and, in italics, the total accelerator-related systematic error

Uncertainty (%)	$\delta\mathcal{P}_e/\mathcal{P}_e$
Laser polarization	0.10
Detector linearity	0.20
Analyzing power calibration	0.40
Electronic noise	0.20
Total polarimeter uncertainty	0.50
Chromaticity and interaction point corrections	0.15

Table 3 gives the fully corrected, luminosity-weighted, average polarizations corresponding to each of the SLD runs. Improvements in GaAs photocathode performance are evident in the 1993 run (first use of a strained-lattice material) and the 1994–1995 run (in which the active layer was three times thinner). Changes in the achieved polarization in later years mainly reflect variation in photocathode manufacture.

A number of experiments and redundant systems were used to verify the high-precision polarimeter. Most important were the following:

- **Moderate precision Møller and Mott polarimeters confirmed the high-precision Compton polarimeter result to $\sim 3\%$ (1993–1995), and gamma polarimeters were operated in parallel with the electron detector polarimeter (1996–1998).** Møller polarimeters located at the end of the SLAC linac and in the SLC electron extraction line were used to cross-check the Compton polarimeter. The perils of using a less reliable method to test a precision device were apparent when large corrections for atomic electron momentum effects in the Møller target were discovered (28) and accounted for, after which good agreement was obtained. In addition, a less direct comparison was provided by Mott polarimeter bench tests of the GaAs photocathodes (29). As described above, during the

Table 3: Luminosity-weighted average polarization values for all SLD data

1992	1993	1994–1995	1996	1997–1998
0.224	0.630	0.7723	0.7616	0.7292
$\pm$ 0.006	$\pm$ 0.011	$\pm$ 0.0052	$\pm$ 0.0040	$\pm$ 0.0038

last years of the program, two photon detectors were used to cross-check the primary electron polarimeter and to experimentally establish calibration uncertainties.

- **SLC arc spin transport was extensively studied (1993–1998) and was frequently monitored and adjusted.** A series of experiments studied the beam polarization reported by the Compton polarimeter as a function of beam energy, beam energy spread, and beam trajectory in the SLC arcs (30). Two spin rotators (in the linac and in the ring-to-linac return line) were scanned in order to determine the IP polarization maximum. An important result of these experiments was the discovery that the SLC arcs operate near a spin tune resonance, leading to the advent of spin manipulation via "spin bumps" in the SLC arcs mentioned above. This procedure eliminated the need for these spin rotators and allowed one to minimize the spin chromaticity ($d\mathcal{P}_e/dE$), which reduced the resulting polarization correction from $> 1\%$ in 1993 to $< 0.2\%$ by 1995.

4 THE PHYSICS ANALYSIS TOOLS

4.1 Monte Carlo Simulation

The Monte Carlo simulation for $Z^0 \rightarrow$ hadrons events employed the `Jetset` 7.4 generator (31). For the B meson decay simulation, the CLEO QQ generator was adopted, with adjustments to improve the agreement with inclusive particle production measurements from ARGUS and CLEO. A detailed simulation of the detector was performed with `Geant` 3.21 (32). Simulated Z^0 decays were overlaid with signals from events taken on random beam crossings in close time-proximity to each recorded Z^0 and then processed using the standard data reconstruction. The Monte Carlo $Z^0 \rightarrow$ hadrons events were produced with statistics exceeding data by factors of 4, 15, and 22 for uds, $c\bar{c}$, and $b\bar{b}$ events, respectively.

For many of the measurements described in this article, the systematic errors associated with tracking efficiency and resolution uncertainties are important and require a consistent evaluation. The uncertainty in the tracking efficiency was evaluated from a comparison between data and Monte Carlo for the fraction of good CDC tracks extrapolating close to the IP that did not have associated VXD hits. These studies indicated that the Monte Carlo simulation overestimated tracking efficiency by $\sim$1.5% on average. A procedure for the random removal of tracks in bins of p_T, ϕ, and θ was used to correct the Monte Carlo for this difference. Most analyses quoted the effect of the entire correction as a systematic error. The effect of residual detector misalignment on the tracking was estimated from the observed shifts in the track impact

parameter distributions as a function of ϕ and θ in both r-ϕ and r-z planes. The typical impact parameter biases observed in the data were $\sim 2.5\,\mu$m ($\sim 5\,\mu$m) in the r-ϕ (r-z) plane. A correction procedure was applied so that the Monte Carlo tracks match the mean bias values of the data in various (ϕ, θ) regions. This was a more realistic evaluation of alignment bias effects, where tracks passing the same detector region were biased in a correlated manner. The full effect of this correction was taken as the systematic error.

4.2 Vertexing Algorithm

Conventional identification of heavy-flavor decays with vertex detectors typically relies on either counting tracks with large impact parameter significance or vertexing kinematically selected decay tracks. SLD took advantage of its CCD vertex detector and the small and stable SLC IP to pioneer inclusive topological vertexing methods that provided additional information on decay kinematics, charge, and flavor.

The topological vertexing algorithm `ZVTOP` (33) aimed to identify all separated vertices and all secondary decay tracks in the event. Well-measured tracks with VXD hits were used to search for secondary vertices by looking for areas of high track overlap density in three-dimensional coordinate space, taking into account the individual track resolution functions. Because of the excellent decay length resolution available at SLD, it was possible in a significant fraction of decays to distinguish secondary (b-hadron decay vertex) tracks from tertiary (cascade charm decay vertex) tracks, instead of lumping all secondary tracks into a single vertex, as was typically done by other experiments. The vertexing algorithm was therefore designed to allow the search for multiple vertices associated with one b-hadron decay.

The vertexing was done in each hemisphere or jet separately. The b hadrons produced in Z^0 decays have an average momentum of $\sim$30 GeV/c, corresponding to $\gamma\beta \sim 6$. This large boost distributes the tertiary vertices along the b-hadron flight direction. The original algorithm, as described by Jackson (33), simply used a $50\,\mu$m-radius cylindrical volume around the jet or hemisphere axis as a preferred secondary vertex volume to suppress fake vertices. An improved version of `ZVTOP`, used by some of the analyses in this article, deployed a "ghost" track to best represent the b-hadron flight direction. This was achieved by finding the direction that minimized the vertex χ^2 sum for the vertices between the ghost track and all other tracks in the jet. It should be noted that once the ghost track was removed, one could be left with single-track "vertices," which is in fact a fairly common decay topology (e.g., one-prong $D^{\pm}$ decays). This algorithm found at least one secondary vertex in 73% (29%) of the hemispheres in $b\bar{b}$ ($c\bar{c}$) events.

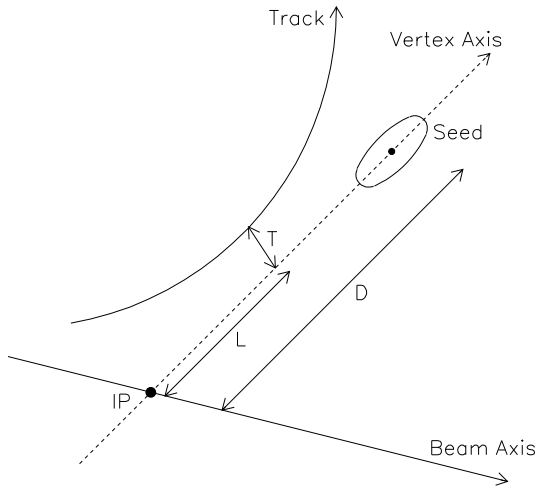

Figure 8: Variables used in ZVTOP track-vertex assignment.

Among the b hemispheres that had at least one secondary vertex, two or more secondary vertices were found in 30% of them.

To obtain the best description of a b hadron, it is crucial to identify all its decay products. Since the basic decay vertex topology was established with well-measured tracks only, an attempt was made to incorporate lower-quality tracks or even unlinked VXD track segments. To do so, a vertex axis was formed by joining the IP to a "seed" vertex combining both secondary and tertiary tracks, and the distance D between the IP and this vertex was computed. For each track, the three-dimensional distance of closest approach T to the vertex axis and the longitudinal distance L between the IP and the point of closest approach on the vertex axis were calculated (see Figure 8). Typical requirements for attaching a track to the seed vertex were $T < 1$ mm, $L > 250$ μm, and $L/D > 0.25$. This track attachment procedure was further improved by means of a neural-network algorithm combining the information on T, L, L/D, and track angle with respect to the vertex axis. There were on average 3.9 quality secondary tracks in the seed vertex, and 0.9 additional tracks were attached per b hemisphere. The VXD track segments were used only for vertex charge determination, with an average of 0.2 such segments attached per b-hadron decay. The sum of the identified secondary tracks and VXD track segments corresponds to an average of 82% of all prompt b-hadron decay tracks, with a track assignment purity of 96.8%.

4.3 b and c Tagging

Prior to the advent of vertex detectors, events with b or c quarks were typically identified by the presence of high-p_T leptons or fully reconstructed D^* decays. However, these tagging methods

suffered from relatively low branching ratios as well as limited purity. The development of vertex detectors opened a new avenue in heavy-flavor tagging by exploiting the surprisingly long b-hadron lifetime. Limited success in b-tagging had already been achieved with vertex drift chambers at PEP/PETRA (34), but b-tagging developed into a powerful tool in the LEP/SLC era only with the advent of silicon vertex detectors. SLD contributed pioneering vertexing techniques to fully explore the high resolution offered by the CCD pixel vertex detector and elevated inclusive b- and c-tagging to a new level.

There are various ways of using the basic tagging tools (tracks with large impact parameters and secondary vertices), which are all quite efficient for b-tagging. However, it is difficult to achieve b-tag purities $> 95\%$ without drastic loss of efficiency because the main remaining background consists of irreducible $c\bar{c}$ events with genuine long decay length. An important improvement in b-tagging was the utilization of the secondary vertex mass as a powerful discriminator to separate b and c quarks.

The SLD implementation of the vertex mass tag included additional kinematical information to improve the efficiency while still maintaining high purity. The tracks identified as secondary by the procedure described in the previous section were used to calculate the raw vertex invariant mass ($M_{\rm raw}$) for each hemisphere. For vertices with $M_{\rm raw}$ close to the charm cutoff of 2 GeV, the vertex momentum is typically collinear with the vertex axis for vertices in $c\bar{c}$ events whereas vertices in $b\bar{b}$ events at this low mass typically have large missing transverse momentum (p_t) with respect to the vertex axis because of missing neutral particles. This information was utilized by forming a "p_t-corrected mass":

$$M_{\rm corr} = \sqrt{M_{\rm raw}^2 + p_t^2} + |p_t|. \tag{7}$$

This minimum-p_t correction can be simply derived by boosting the system of identified secondary tracks along the vertex axis until their longitudinal momentum sum is zero, and assuming that a massless neutral system is recoiling with the missing p_t in that frame. To prevent $udsc$ events from gaining an artificially large p_t due to detector resolution effects, the p_t was actually the minimum p_t allowed by the uncertainties in the primary and secondary vertex positions. $M_{\rm corr}$ was further restricted to be $\leq 2 \times M_{\rm raw}$ to reduce the contamination from fake vertices in light-quark events. The effectiveness of $M_{\rm corr}$ as a b-tagging variable can be clearly seen in Figure 9*a*. Many analyses using only a basic secondary track classification and requiring a mass tag of $M_{\rm corr} > 2$ GeV benefited from a hemisphere b-tagging efficiency of 53% and a b purity of 98%. In this simple scheme, a cut on the raw mass of $M_{\rm raw} > 2$ GeV would give a similar purity, but the efficiency would be only 35%. The partial correction for missing neutral particles

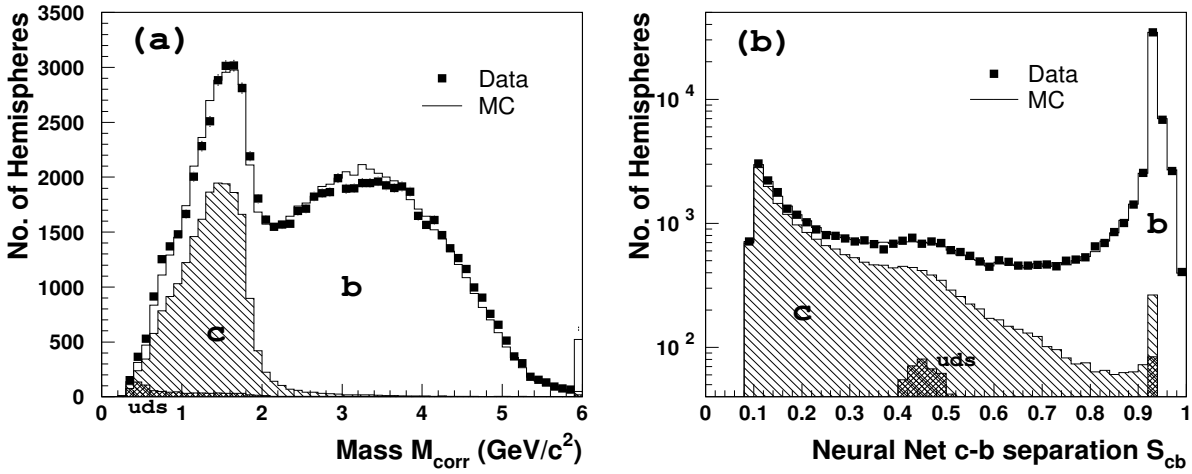

Figure 9: Distributions of (a) the p_t-corrected mass $M_{\rm corr}$ and (b) the neural-net $c-b$ separation variable S_{cb} comparing data and Monte Carlo.

depends critically on the ability to precisely measure the primary and secondary vertex positions to ensure that the vertex flight direction was well determined. The fact that so far only SLD has effectively applied this underscores the crucial role of the small and stable SLC IP and the high-precision vertexing achieved with the CCD vertex detector.

Although the requirement $M_{\rm corr} > 2\,{\rm GeV}$ cleanly selected the high-mass b hemispheres, further kinematical information can be used to achieve good separation between b and c in the mass region below 2 GeV. A neural-network algorithm was constructed to process information on the secondary vertex momentum, track multiplicity, and decay length, in addition to the p_t-corrected mass, leading to a single $c-b$ separation variable S_{cb} as shown in Figure 9b. The b tags were given by large values of S_{cb}, whereas a clean c tag also emerged at small S_{cb}. A typical b tag requiring $S_{cb} > 0.75$ gave a hemisphere b-tagging efficiency of ϵ_b=62% and purity of Π_b=98.3%.

We not only enhanced the b-tag performance but also simultaneously obtained a c tag with a typical cut of $S_{cb} < 0.30$, giving ϵ_c=18% and Π_c=84%. Given the shorter lifetime and much less distinctive kinematical properties of $c\bar{c}$ events, this is also a very impressive performance, which is approaching the earlier era of b-tagging performance. It should be noted that the uds events amounted to only a very small fraction of the events containing a secondary vertex, and they were concentrated near $S_{cb} = 0.5$. Furthermore, a large fraction of the uds background was actually due to $g \to b\bar{b}$ and $g \to c\bar{c}$ production in uds events. The success of this inclusive charm tag is unique to SLD.

4.4 Hadron Identification

SLD was one of two Z^0 resonance experiments with a Cherenkov ring imaging system for hadron identification. The primary goal of the CRID was to identify charged pions, kaons, and protons, but the system proved valuable in lepton identification also (see next section). Hadron identification at SLD relied exclusively on the CRID, i.e., no dE/dx information from the CDC was used. Tracks were extrapolated outward from the end of the drift chamber through the liquid and gas radiators. The TPC hit positions were then transformed into Cherenkov angles with respect to the track trajectory for each of the radiators. Finally, a global likelihood approach was used to identify the charged particles. A likelihood $\mathcal{L}_i$ was computed for each particle hypothesis ($i = e$, μ, π, K, or p). The likelihood made use of the expected number of photons and Cherenkov angle, which both depend on the charged-particle momentum and the mass hypothesis chosen, the number and angles of reconstructed photons, and a background term. The latter incorporated information about background from random hits as well as the contribution from genuine Cherenkov photons originating from other charged particles in the event. The identification proceeded by cutting on differences between the logarithms of these likelihoods (the log-likelihoods from the two radiators were simply added to form an overall likelihood).

Kaon identification is very important in heavy-flavor physics, and it is preferable to keep as high an efficiency as possible by focusing mostly on pion rejection. Proton rejection was difficult in the momentum range $3 \lesssim p \lesssim 9$ GeV/c because both kaons and protons were below Cherenkov threshold in the gas radiator and were thus primarily identified by the absence of Cherenkov radiation. Pion rejection was achieved by requiring $\log \mathcal{L}_K - \log \mathcal{L}_\pi > 3$ (> 5) for $p < 2.5$ (> 2.5) GeV/c, corresponding to the momentum region below (above) threshold for charged pion radiation in the gas radiator. Loose proton rejection was obtained with $\log \mathcal{L}_K - \log \mathcal{L}_\mathrm{p} > -1$. Other cuts were also applied to guarantee that the detector was fully operational and that the quality of the track extrapolation was high. For kaons with $p > 0.8$ GeV/c and $|\cos\theta| < 0.68$, the selection had an efficiency between 40 and 55%, depending on the momentum of the track. Using clean pion samples from $K^0_S \to \pi^+\pi^-$ decays, the $\pi \to K$ misidentification rate was measured to be nearly constant at 2.5% for $0.8 < p < 2.5$ GeV/c, rising to about 10% between 2.5 and 4 GeV/c and remaining $\sim$10% for $p > 4$ GeV/c.

4.5 Lepton Identification

Like hadron identification, lepton identification required that charged tracks be extrapolated outward from the drift chamber to the LAC and WIC subsystems. The extrapolation transported

the track parameters as well as the error matrix, taking multiple scattering into account.

Electron identification was performed in the range $|\cos\theta| < 0.72$ for tracks with $p > 1$ GeV/c and relied primarily on information from the LAC. A special feature of the identification was the use of the CRID to remove charged hadron contamination. A neural network, tuned to the Monte Carlo simulation and cross-checked with data, optimized the electron selection based on the LAC and CRID variables. The selection efficiency was estimated using the Monte Carlo simulation to be 64%, whereas the purity was 64% for $p > 2$ GeV/c. A pion misidentification rate of approximately 1.0% was measured with a clean sample of pion tracks from $K^0_S \to \pi^+\pi^-$ decays, in good agreement with the simulation. Electrons from photon conversion were identified and rejected with a 73% efficiency.

Muon identification was performed in the range $|\cos\theta| < 0.70$. Extrapolated charged tracks with $p > 2$ GeV/c were matched with hit patterns in the WIC. Cuts on the quality of the hit pattern and CDC/WIC match, as well as the penetration depth, provided a sample of muons with 81% efficiency and 68% purity, as determined in the simulation. This muon selection also took advantage of the CRID to reject approximately half of the charged kaon and proton contamination in most of the momentum range, and roughly a third of all charged pions with $p < 6$ GeV/c (with an efficiency loss of only 5%). Information from the pattern of energy deposition in the LAC was also used in the identification and was especially useful at larger $|\cos\theta|$. Pion misidentification rates of about 0.3% were estimated from $K^0_S \to \pi^+\pi^-$ and $\tau^\pm$ decays in the data, in reasonable agreement with the simulation.

5 ELECTROWEAK PHYSICS: Z^0 BOSON COUPLINGS

5.1 Introduction

In Section 1, we mentioned that in the standard model the $Zf\overline{f}$ couplings depend on the weak-isospin of the fermions and on a single parameter, $\sin^2\theta_W$, but we did not discuss the origin of this parameter. Recall that in the standard model, the weak isotriplet $\vec{A}_\mu$ and the isosinglet B_μ gauge fields, with gauge couplings g and g', are mixed by electroweak symmetry breaking due to the finite vacuum expectation value of the Higgs scalar field. The charged fields A^1_μ and A^2_μ and neutral fields B_μ and A^3_μ combine linearly into the physical charged W^+ and W^- and the neutral photon and Z^0 gauge bosons. This change of basis is parameterized by a weak mixing angle θ_W, given by $g' = g\tan(\theta_W)$, and the masses of the physical gauge bosons (and the fermions) emerge as by-products of electroweak symmetry breaking (the "Higgs mechanism").

Electroweak tests of the standard model reached an important turning point once the Z^0 boson mass was determined at LEP to a precision of two parts in 10^5. The measurement of M_Z provides a third precision constant, which together with the Fermi constant G_F (constrained by muon decay) and the fine structure constant α (evaluated at $Q^2 = M_Z^2$) is sufficient to determine the three universal parameters of the electroweak standard model: the $SU(2)_L \times U(1)$ couplings g and g', and the vacuum expectation value of the Higgs field. The couplings of fermions to the Z^0 boson are, by virtue of weak mixing, a function of θ_W—hence, their determination provides a fundamental test of electroweak symmetry breaking and, if sufficiently precise, of higher-order corrections. The electroweak measurements made by the SLD collaboration can generally be described as measurements of the fermion-to-Z^0 couplings.

The differential cross section for $e^+e^- \to Z^0 \to f\bar{f}$ is expressed as

$$\frac{d\sigma}{d\cos\theta} = (1 - \mathcal{P}_e A_e)(1 + \cos^2\theta) + 2\cos\theta(A_e - \mathcal{P}_e)A_f, \tag{8}$$

where $\cos\theta$ is the cosine of the angle between the final-state fermion f and the incident electron directions, $\mathcal{P}_e$ is the electron beam longitudinal polarization, and A_e and A_f are the asymmetry parameters for the initial- and final-state fermions, respectively. The asymmetry parameter for a given fermion represents the extent of parity violation at the $Z^0 \to f\overline{f}$ vertex and is defined as

$$A_f = \frac{2 g_V g_A}{g_V^2 + g_A^2} = \frac{g_L^2 - g_R^2}{g_L^2 + g_R^2}. \tag{9}$$

The parameter A_f can be isolated by the measurement of various cross-section asymmetries, which is experimentally attractive because systematic effects are minimized. In addition, $g_V^2 + g_A^2$ (or equivalently, $g_L^2 + g_R^2$) is determined from the Z^0-decay partial widths, which are normalized by the hadronic decay partial width to control systematic effects.

The simplest of the asymmetries is the left-right cross-section asymmetry

$$A_{LR}^0 = \frac{\sigma_L - \sigma_R}{\sigma_L + \sigma_R} = A_e, \tag{10}$$

for which all angular dependence and all dependence on the final state cancel[1]. As a result, $A_{\rm LR}$ is a particularly robust quantity, with smaller systematic effects than any other asymmetry. This asymmetry provides a direct measurement of the coupling between the Z^0 and the e^+e^- initial state, and provides, as we shall see, the best sensitivity to $\sin^2\theta_W$.

[1]The dependence of $A_{\rm LR}$ on the final state couplings and polar (and azimuthal) angle completely vanishes, provided that the efficiency for detecting a fermion at some polar angle (with respect to the electron direction) is equal to the efficiency for detecting an anti-fermion at the same polar angle. This condition is satisfied by the SLD detector.

Table 4: The approximate magnitude of the various fermion-to-Z^0 coupling parameters, for $\sin^2\theta_W^{\rm eff} = 0.23$

	g_L^f	g_R^f	$R_f = \frac{\Gamma(Z^0\to f\overline{f})}{\Gamma(Z^0\to hadrons)}$	A_f	$\frac{\delta A_f}{\delta \sin^2\theta_w}$
e, μ, τ	-0.27	-0.23	0.05	0.15	-7.9
u, c	0.35	0.15	0.17	0.67	-3.5
d, s, b	-0.42	-0.08	0.22	0.94	-0.6

Asymmetries that retain angular information are sensitive to the final-state couplings. For $Z^0 \to f\overline{f}$ decays, the forward-backward asymmetry, measured at LEP for lepton and heavy quark final states, can be expressed in terms of $z = \cos\theta$ as

$$A_{\rm FB}^f(z) = \frac{\sigma^f(z) - \sigma^f(-z)}{\sigma^f(z) + \sigma^f(-z)} = A_e A_f \frac{2z}{1+z^2}. \tag{11}$$

The asymmetry $A_{\rm FB}^f$ for fermions is a composite observable sensitive to both the initial-state A_e and the final-state A_f. For example, from the magnitudes of the parity violation parameters A_f as listed in Table 4, it can be seen in the case of the b quark that the large value of A_b makes $A_{\rm FB}^b$ particularly sensitive to A_e (and hence to $\sin^2\theta_W$). In general, the final-state $Zf\overline{f}$ asymmetry parameter A_f can be deduced by taking the lepton coupling A_e's from other measurements such as the τ polarization, the lepton pair forward-backward asymmetries, and $A_{\rm LR}$. Note that $A_{\rm FB}^f$ is subject to systematic errors in the determination of detector acceptance and efficiency.

At the SLC, the polarized forward-backward asymmetry can be measured. Due to the factor $(A_e - \mathcal{P}_e)$ in Equation 8, manipulation of the helicity of the e^- beam ($\mathcal{P}_e < 0$ for left-handed electrons) distinguishes two different forward-backward asymmetries. In particular, for a highly polarized beam, the forward-backward asymmetry is not only of the opposite sign for left-handed beam, the magnitude is also expected to be larger compared with the asymmetry for right-handed beam. Separate measurements of the left and right cross sections can be combined into the left-right forward-backward asymmetry

$$\tilde{A}_{\rm FB}^f(z) = \frac{[\sigma_L^f(z) - \sigma_L^f(-z)] - [\sigma_R^f(z) - \sigma_R^f(-z)]}{[\sigma_L^f(z) + \sigma_L^f(-z)] + [\sigma_R^f(z) + \sigma_R^f(-z)]} = |\mathcal{P}_e| A_f \frac{2z}{1+z^2}. \tag{12}$$

The use of $\tilde{A}_{\rm FB}^f$ eliminates the dependence on A_e and measures A_f directly. Compared with $A_{\rm FB}^f$, $\tilde{A}_{\rm FB}^f$ benefits from a large gain in statistical power for the determination of A_f. Given an SLC electron beam polarization of $\sim$75%, this improvement factor is $(\mathcal{P}_e/A_e)^2 \sim 25$. The effects of nonuniformity of the detector acceptance and efficiency cancel to first order for this double

asymmetry. The SLD collaboration has measured $\tilde{A}_{\rm FB}^f$ for bottom, charm, and strange quarks as well as the charged leptons, providing direct measurements of the associated fermion asymmetry parameters. With the exceptions of A_e and A_τ, these direct measurements are unique to SLD.

Measurements of partial Z^0-decay widths provide information complementing that obtained from the asymmetries. Because

$$R_f = \frac{\Gamma(Z^0 \to f\bar{f})}{\Gamma(Z^0 \to \text{hadrons})} \propto g_L^2 + g_R^2 \ , \tag{13}$$

R_f measures the $Z^0 \to f\overline{f}$ coupling strength, whereas A_f measures the extent of parity violation at the $Z^0 \to f\overline{f}$ vertex. From another perspective, consider for example the sensitivity of R_b and A_b to the left- and right-handed $Zb\bar{b}$ couplings:

$$\begin{aligned} \delta R_b/R_b &\sim -3.57\,\delta g_L^b - 0.65\,\delta g_R^b \quad \text{and} \\ \delta A_b/A_b &\sim -0.31\,\delta g_L^b + 1.72\,\delta g_R^b. \end{aligned} \tag{14}$$

We see that R_b is more sensitive to the possible deviations in the left-handed $Zb\bar{b}$ coupling, and A_b is more sensitive to deviations in the right-handed coupling. The SLD collaboration has measured both R_b and R_c.

We have discussed how the well-determined constants M_Z, G_F, and $\alpha(M_Z^2)$ constrain the standard model. However, these data are a sufficient set only at tree level, and to test the standard model, including loop effects, at least one additional precise measurement is required. In the standard model, aside from the effects of real and virtual photons, radiative corrections to the fermion-to-gauge boson couplings are dominated by corrections to the boson propagators. These effects are known as oblique corrections because the virtual loop is not directly coupled to the initial- or final-state fermions (see Figure 10). Loop corrections to the boson propagators are dominated by those due to the heaviest fermion, the top quark, and are proportional to $(m_t^2 - m_b^2)/M_Z^2$ (note that this factor depends on weak-isospin symmetry breaking in the top-bottom doublet). This arises because of the proportionally large Yukawa couplings of the heaviest fermions to the Higgs boson. The sensitivity of the radiative corrections to m_t means that precise electroweak measurements can be used to constrain m_t. Now that m_t has been measured directly, precision measurements have become sensitive to much smaller effects, such as those due to the Higgs boson, which are only logarithmic in the Higgs mass, and sensitive to effects due to new physics processes.

In the standard model, direct vertex corrections (see Figure 11) are small, but they are expected to be largest for the heaviest fermions. In particular, the $Zb\bar{b}$ vertex corrections, which act only on the left-handed coupling, are particularly large owing to the large top quark mass

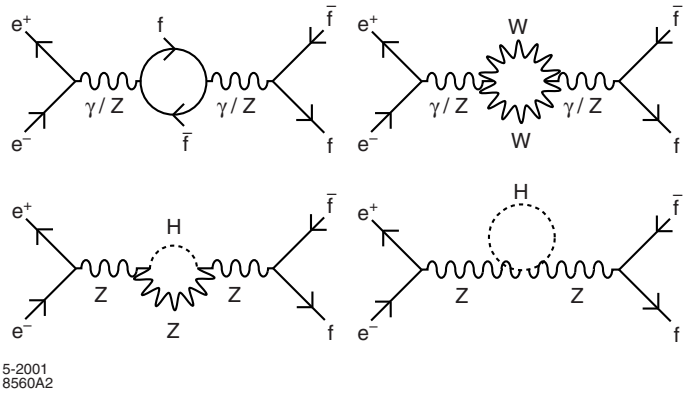

Figure 10: Feynman diagrams showing radiative corrections affecting the Z^0 propagator, including contributions from fermions, gauge bosons and the Higgs boson.

and the fact that the relevant quark-mixing matrix element ($|V_{tb}| \sim 1$) is large. In general, heavy quark partial widths and asymmetry parameters are most sensitive to vertex corrections but with different sensitivity to left- and right-handed coupling constants. In contrast, oblique corrections are best isolated by measurements of the lepton asymmetries, and this distinction has an important consequence. In contrast to the $\sin^2\theta_W$ sensitive lepton asymmetries, the vertex-sensitive observables are largely independent of the Higgs boson and top quark masses, so their standard-model predictions are relatively unambiguous. Hence, the SLD precision electroweak results constitute a complementary set of neutral-current coupling measurements.

5.2 Lepton Couplings

5.2.1 The $A_{\rm LR}$ Measurement

The measurement of the left-right cross-section asymmetry $A_{\rm LR}$ (35, 36) at the SLC provides a determination of the asymmetry parameter A_e and is presently the most precise single measure-

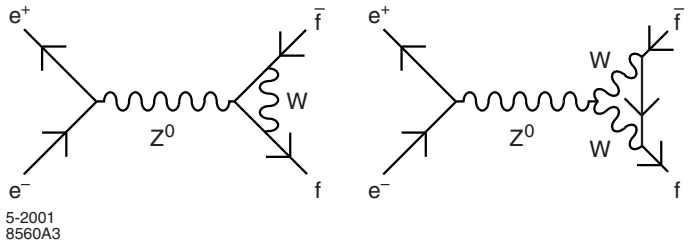

Figure 11: Feynman diagrams showing radiative corrections affecting the Z^0 coupling to the final state fermions.

ment, with the smallest systematic error, of this quantity. In addition, A_e is particularly sensitive to the effective weak mixing angle with $\delta A_e \approx 7.85(\delta \sin^2\theta_W^{\rm eff})$ (for the $A_{\rm FB}^{\ell}$ measurements, the analogous factor is 1.77). Hence, the most precise available determination of the effective weak mixing angle derives from the $A_{\rm LR}$ measurement.

In principle, the analysis is straightforward. One counts the numbers of Z^0 bosons produced by left- and right-handed longitudinally polarized electrons ($N_{\rm L}$ and $N_{\rm R}$), forms an asymmetry, and then divides by the luminosity-weighted e^- beam polarization (the e^+ beam is not polarized):

$$A_{\rm LR} = \frac{N_{\rm L} - N_{\rm R}}{N_{\rm L} + N_{\rm R}} \frac{1}{\langle \mathcal{P}_e \rangle}. \tag{15}$$

The method requires no detailed final-state event identification (e^+e^- final-state events are removed because of their nonresonant t-channel contributions, as are all other backgrounds not due to Z^0 decay) and is insensitive to all acceptance and efficiency effects. In order to convert the $A_{\rm LR}$ into a determination of the effective weak mixing angle, the result is converted into a "Z^0-pole" value by the application of a small (typically about 2.0%) correction for initial-state radiation and $\gamma - Z^0$ interference (37):

$$A_{\rm LR}(E_{\rm cm}) \rightarrow A_{\rm LR}^0 \equiv A_e. \tag{16}$$

This calculation requires accurate and precise knowledge of the luminosity-weighted average center-of-mass collision energy $E_{\rm cm}$.

For the most recent data (1997–1998), the small total systematic error of a relative 0.65% is dominated by the 0.50% relative systematic error in the determination of the e^- polarization, with the second largest error (0.39%) arising from uncertainties in the determination of the luminosity-weighted average center-of-mass energy. Some much smaller contributions to the systematic error are discussed below. The relative statistical error on $A_{\rm LR}$ from all data is about 1.3%.

Below, we describe some details of the $A_{\rm LR}$ measurement and provide some historical context for the $A_{\rm LR}$ program at SLC/SLD (1992–1998).

Systematic Effects and Their Control The $A_{\rm LR}$ measurement is remarkably resistant to detector-dependent systematic effects and Monte Carlo modeling uncertainties that are significant issues for most other electroweak precision measurements. By far the dominant systematic effects arise from polarimetry and from the determination of the collision energy, rather than from any details of the analysis or the operation of SLD. The simple expression given in Equation 15 applies to the ideal case in the absence of additional systematic effects, and as such it is a good approximation to better than 0.2%. Nevertheless, systematic left-right asymmetries in

luminosity, polarization, beam energy, and acceptance, as well as background and positron polarization effects, can be incorporated into an extended expression for the cross-section asymmetry. One finds that the measured asymmetry A_m is related to $A_{\rm LR}$ by the following expression, which incorporates a number of small correction terms in lowest-order approximation:

$$A_{\rm LR} = \frac{A_m}{\langle \mathcal{P}_e \rangle} + \frac{1}{\langle \mathcal{P}_e \rangle}\Bigg[f_{\rm bkg}(A_m - A_{\rm bkg}) - A_{\mathcal{L}} + A_m^2 A_{\mathcal{P}} - E_{\rm cm}\frac{\sigma'(E_{\rm cm})}{\sigma(E_{\rm cm})} A_E - A_\varepsilon + \langle \mathcal{P}_e \rangle \mathcal{P}_p \Bigg], \quad (17)$$

where $\langle \mathcal{P}_e \rangle$ is the mean luminosity-weighted polarization; $f_{\rm bkg}$ is the background fraction; $\sigma(E)$ is the unpolarized Z^0 boson cross section at energy E; $\sigma'(E)$ is the derivative of the cross section with respect to E; $A_{\rm bkg}$, $A_{\mathcal{L}}$, $A_{\mathcal{P}}$, A_E, and A_ε are the left-right asymmetries[2] of the residual background, the integrated luminosity, the beam polarization, the center-of-mass energy, and the product of detector acceptance and efficiency, respectively; and $\mathcal{P}_p$ is any longitudinal positron polarization, which is assumed to have constant helicity. Because the colliding electron and positron bunches were produced on different machine cycles and because the electron helicity of each cycle was chosen randomly, any positron helicity arising from the polarization of the production electrons was uncorrelated with the electron helicity at the IP. The net effect of positron polarization from this process vanished rigorously. However, positron polarization of constant helicity would affect the measurement.

The close ties between the $A_{\rm LR}$ measurement and the SLC accelerator complex are highlighted by numerous accelerator-based experiments dedicated to the SLD physics program. Particularly important among these experiments was a Z^0-peak scan to calibrate the sum of the beam energies. The SLC energy spectrometers were briefly described in Section 2.2. These devices were first operated in their final configuration in 1989 by the Mark II experiment, and the calibration of the two precision spectrometer magnets was performed in 1988 (14). Their expected precision was about ± 20 MeV on the measured center-of-mass collision energy $E_{\rm cm}$. The importance of these devices to the $A_{\rm LR}$ measurement is quantified by the approximate rule of thumb that an 80 MeV uncertainty in $E_{\rm cm}$ corresponds to a 1% error on the Z^0-pole asymmetry $A^0_{\rm LR}$. For this reason, a Z^0-peak scan was performed in 1998 to calibrate the spectrometers to the LEP measurement of the Z^0 mass. The scan used two optimized off-peak points at $+0.88$ and -0.93 GeV and a luminosity approximately equivalent to 9000 produced Z^0 bosons to reach a statistical precision on the peak position of 20 MeV. The results of a complete analysis of systematic effects

[2]The left-right asymmetry for a quantity Q is defined as $A_Q \equiv (Q_L - Q_R)/(Q_L + Q_R)$ where the subscripts L and R refer to the left- and right-handed beams, respectively.

determined an offset of -46 MeV and a total $E_{\rm cm}$ uncertainty of 29 MeV [the 0.39% uncertainty on $A_{\rm LR}^0$ mentioned above and given in Table 5 (38)].

Other examples of accelerator-based experiments include the following:

- **The e^- bunch helicity transmission was verified by setting up a large current-helicity correlation in the SLC, allowing for the use of the LAC to verify data synchronization (1992–1993).** Although the electron bunch polarization state was transmitted via reliable and redundant paths to the SLD detector/polarimeter complex, the SLD electroweak group proposed a series of independent tests of the synchronization of this information and the SLD event data. In one such test, the laser optics at the SLC polarized source were temporarily modified by the addition of a polarizer and quarter-wave plate so that photocathode illumination was nulled for one of the two circular polarization states. The positron beam was turned off, and the electron beam was delivered to the IP. Beam-related background in the LAC was detected, but only for the non-extinct pulses. By this means, the expected correlation between helicity and the presence of beam, and hence the LAC data stream, was verified (39).
- **Positron polarization was experimentally constrained.** In 1998, a dedicated experiment was performed in order to directly test the expectation that accidental polarization of the positron beam was negligible. The positron beam was delivered to the SLAC End Station A (ESA), where a Møller polarimeter was used. Experimental control was assured by first delivering the polarized electron beam, and then an unpolarized electron beam (sourced from SLAC's thermionic electron gun), to the ESA, confirming polarimeter operation. In addition, the spin rotator magnet located in the linac was reversed halfway through the positron beam running, thereby reversing the sense of polarization at the Møller target and reducing systematic error. The final result verified that e^+ polarization was consistent with zero ($-0.02 \pm 0.07\%$) (40).

A simple calorimetric event selection in the LAC, supplemented by track multiplicity and topology requirements in the CDC, was used to select hadronic Z^0 decays. For each event candidate, energy clusters were reconstructed in the LAC. Selected events were required to contain at least 22 GeV of energy observed in the clusters and to have a normalized energy imbalance[3] of less than 0.6. The left-right asymmetry associated with final-state e^+e^- events is expected to be diluted by the t-channel photon exchange subprocess. Therefore, we excluded

[3]The energy imbalance is defined as a normalized vector sum of the energy clusters as follows, $E_{\rm imb} = |\sum \vec{E}_{\rm cluster}|/\sum |E_{\rm cluster}|$.

e^+e^- final states by requiring that each event candidate contain at least four selected CDC tracks, with at least two tracks in each hemisphere (defined with respect to the beam axis), or at least four tracks in either hemisphere. This track topology requirement excluded Bhabha events that contained a reconstructed gamma conversion. Small backgrounds in the $A_{\rm LR}$ data sample were due to residual e^+e^- final-state events, and to two-photon interactions, beam-related noise, and cosmic rays. For the most recent data (1996–1998), the total background contamination was estimated to be $< 0.05\%$ for a selection efficiency of $(91 \pm 1)\%$.

The asymmetries in luminosity, polarization, and beam energy were all continually monitored using small-angle Bhabha counters, the Compton polarimeter, and energy spectrometer data available at the SLC repetition rate of 120 Hz. These asymmetries were limited to approximately 10^{-4}, 10^{-3}, and 10^{-6}, respectively. The long-term average values of all asymmetries of this type were reduced by the roughly trimonthly reversal of the transverse polarization sense in the electron damping ring (DR) referred to in Section 2. The dominant cause of the observed asymmetries was the small current asymmetry produced at the SLC polarized source. This effect arose because of the source photocathode sensitivity to linear polarized light, together with residual linear polarization in the source laser light that was correlated with the light helicity. The source current asymmetry was minimized by a polarization control and intensity feedback system (starting in 1993) and was generally maintained below 10^{-4}.

The value of $A_{\rm LR}$ is unaffected by decay-mode-dependent variations in detector acceptance and efficiency, provided that the efficiency for detecting a fermion at some polar angle (with respect to the electron direction) is equal to the efficiency for detecting an anti-fermion at the same polar angle. This fact, and the high degree of polar symmetry in the SLD detector, render A_ε negligible. Finally, $\mathcal{P}_p$ was experimentally demonstrated to be consistent with zero to a precision of 7×10^{-4}, as described above. Calculations based on polarization buildup in the positron DR suggested a much smaller number, $\mathcal{P}_p < \mathcal{O}(10^{-5})$; hence, no correction for $\mathcal{P}_p$ was applied to the data.

Table 5 summarizes the systematic effects discussed in this section. The total uncertainties due to backgrounds and accelerator-induced asymmetries were much smaller than the leading systematic effects due to polarimetry and energy uncertainties, as can be seen by comparing the last three rows of Table 5.

Table 6 shows the run-by-run $A_{\rm LR}$ results. The previously discussed $E_{\rm cm}$-dependent radiative correction and its uncertainty are evident in the difference between $A_{\rm LR}$ and $A^0_{\rm LR}$. These five results show a χ^2 of 7.4 for four degrees of freedom, corresponding to a probability of 11.6%.

Table 5: Z^0 event counts and corrections for all SLD run periods. Also shown are the total polarimetry errors (including chromaticity and IP effects) and the relative error due to the electroweak interference correction needed for the conversion of $A_{\rm LR}$ to $A^0_{\rm LR}$. Note that because of low statistics, a number of effects were ignored for the 1992 data.

	1992	1993	1994–95	1996	1997–98
N_L	5,226	27,225	52,179	29,016	183,335
N_R	4,998	22,167	41,465	22,857	148,259
A_m	0.0223	0.1024	0.1144	0.1187	0.1058
	$\pm$0.0099	$\pm$0.0045	$\pm$0.0032	$\pm$0.0044	$\pm$0.0017
$f_{\rm bkg}$ (%)	1.4	0.25	0.11	0.029	0.042
	$\pm$1.4	$\pm$0.10	$\pm$0.08	$\pm$0.021	$\pm$0.032
$A_{\rm bkg}$		0.031	0.055	0.033	0.023
		$\pm$0.010	$\pm$0.021	$\pm$0.026	$\pm$0.022
$A_{\mathcal{L}}$ (10^{-4})	1.8	0.38	-1.9	$+0.03$	-1.3
	$\pm$ 4.2	$\pm$ 0.50	$\pm$ 0.3	$\pm$ 0.50	$\pm$ 0.7
$A_{\mathcal{P}}(10^{-4})$	-29	-33	$+24$	$+29$	$+28$
		$\pm$ 1	$\pm$ 10	$\pm$ 43	$\pm$ 69
A_E (10^{-4})		0.0044	0.0092	-0.0001	$+0.0028$
		$\pm$0.0001	$\pm$0.0002	$\pm$0.0035	$\pm$0.0014
$E_{\rm cm}\frac{\sigma'(E_{\rm cm})}{\sigma(E_{\rm cm})}$		-1.9	0.0	2.0	4.3
			$\pm$ 2.5	$\pm$ 3.0	$\pm$ 2.9
A_ε	0	0	0	0	0
$\mathcal{P}_p$ (10^{-4})	< 0.16	< 0.16	< 0.16	< 0.16	-2
					$\pm$ 7
Total correction,		$+$ 0.10	$+$ 0.2	$+0.02$	$+0.16$
$\Delta A_{\rm LR}/A_{\rm LR}$, (%)		$\pm$ 0.08	$\pm$ 0.06	$\pm$ 0.05	$\pm$ 0.07
$\delta\mathcal{P}_e/\mathcal{P}_e$ (%)	2.7	1.7	0.67	0.52	0.52
Electroweak interference		0.3	0.4	0.4	0.39
correction [relative (%)]					

The $\sin^2\theta^{\rm eff}_W$ results are derived from the equivalence $A^0_{\rm LR} \equiv A_e$, which implies

$$A^0_{\rm LR} = \frac{2(1-4\sin^2\theta^{\rm eff}_W)}{1+(1-4\sin^2\theta^{\rm eff}_W)^2}. \tag{18}$$

Table 6: Summary of $A_{\rm LR}$ and $\sin^2\theta_W^{\rm eff}$ measurements for all SLD runs (statistical and systematic errors are listed separately)

Data Set	$A_{\rm LR}$	$A_{\rm LR}^0$	$\sin^2\theta_W^{\rm eff}$
1992	0.100	0.097	0.2378
	$\pm 0.044 \pm 0.004$	$\pm 0.044 \pm 0.004$	$\pm 0.0056 \pm 0.0005$
1993	0.1628	0.1656	0.2292
	$\pm 0.0071 \pm 0.0028$	$\pm 0.0071 \pm 0.0028$	$\pm 0.0009 \pm 0.0004$
1994–1995	0.1485	0.1512	0.23100
	$\pm 0.0042 \pm 0.0010$	$\pm 0.0042 \pm 0.0011$	$\pm 0.00054 \pm 0.00014$
1996	0.1559	0.1593	0.22996
	$\pm 0.0057 \pm 0.0008$	$\pm 0.0057 \pm 0.0010$	$\pm 0.00073 \pm 0.00013$
1997–1998	0.1454	0.1491	0.23126
	$\pm 0.0024 \pm 0.0008$	$\pm 0.0024 \pm 0.0010$	$\pm 0.00030 \pm 0.00012$
All		0.15138 ± 0.00216	0.23097 ± 0.00027

The average for the complete SLD data sample is

$$\begin{aligned} A_{\rm LR}^0 &= 0.15138 \pm 0.00216, \\ \sin^2\theta_W^{\rm eff} &= 0.23097 \pm 0.00027. \end{aligned} \tag{19}$$

Small correlated systematic effects are accounted for in the calculation of this average.

5.2.2 Leptonic Asymmetries

The individual lepton asymmetry parameters were determined from lepton final-states (41, 42). The $A_{\rm LR}$ measurement determined the initial-state parameter A_e, but electron polarization also allows direct measurement of the final-state asymmetry parameter A_ℓ for lepton ℓ using the left-right forward-backward asymmetry ($\tilde{A}_{\rm FB}^\ell = \frac{3}{4}\langle\mathcal{P}_e\rangle A_\ell$). If lepton universality is assumed, the results for all three lepton flavors can be combined to yield a determination of $\sin^2\theta_W^{\rm eff}$, which in turn can be combined with the more precise result from $A_{\rm LR}$. The event sample used for $A_{\rm LR}$ was purely hadronic (there was a very small $0.3\pm0.1\%$ admixture of $\tau^+\tau^-$ events), and hence, the left-right asymmetry of the lepton events constituted an independent measurement. Although the lepton final-state analysis described below is more sophisticated than a simple $A_{\rm LR}$-style counting measurement, essentially all the information on $\sin^2\theta_W^{\rm eff}$ is obtained from the left-right asymmetry

Table 7: Summary of event selections, efficiency, and purity for $e^+e^- \to \ell^+\ell^-$ for the 1997–1998 SLD data

Event sample	Background fraction	Efficiency in $\lvert\cos\theta\rvert < 0.9$	# of selected events
$e^+e^- \to e^+e^-$	0.7% $\tau^+\tau^-$	75%	15,675
$Z^0 \to \mu^+\mu^-$	0.2% $\tau^+\tau^-$	77%	11,431
$Z^0 \to \tau^+\tau^-$	$e^+e^- : \mu^+\mu^- : 2\text{-}\gamma : \text{hadrons}$ $0.9\% : 2.9\% : 0.9\% : 0.6\%$	70%	10,841

of these events. For example in the 1996-1998 data set, the inclusion of the distributions in polar angle that are essential for the extraction of the final-state asymmetries improved the resulting precision on $\sin^2\theta_W^{\text{eff}}$, but only to ± 0.00076, compared with about ± 0.00078 obtained from a simple left-right event count.

The Analysis Method Table 7 summarizes the selection efficiencies, backgrounds, and numbers of selected candidates for e^+e^-, $\mu^+\mu^-$, and $\tau^+\tau^-$ final states. Event-by-event maximum likelihood fits, for each lepton flavor, were used to incorporate the contributions of all the terms in the polarized differential cross section and to include the effect of initial-state radiation. Photon exchange terms and, if the final-state leptons were electrons, t-channel contributions, were taken into account. All three lepton asymmetry parameters, A_e and A_μ (A_τ), were obtained from $\mu^+\mu^-$ ($\tau^+\tau^-$) final states. These A_e results were combined with A_e obtained from the e^+e^- final state.

Figure 12 shows the $\cos\theta$ distributions for e^+e^-, $\mu^+\mu^-$, and $\tau^+\tau^-$ candidates for the 1997–1998 data. The pre-1997 results are similar but have smaller acceptance ($\lvert\cos\theta\rvert \leq 0.8$) (note that the SLD event totals including this older data are 22,254, 16,844, and 16,084 for the e^+e^-, $\mu^+\mu^-$ and $\tau^+\tau^-$ final states respectively).

The high-$\lvert\cos\theta\rvert$ region is increasingly sensitive to the asymmetry parameters, most apparent in the $\mu^+\mu^-$ and $\tau^+\tau^-$ distributions in Figure 12. In 1996, the upgraded vertex detector and a new trigger system for forward $\mu^+\mu^-$ events were installed. The improved acceptance of VXD3 allowed for efficient track finding up to $\lvert\cos\theta\rvert = 0.9$ (42). The new trigger for $\mu^+\mu^-$ events covered the angular range up to $\lvert\cos\theta\rvert < 0.95$ by requiring two back-to-back tracks that pass through the IP and reach the endcap WIC used for muon identification.

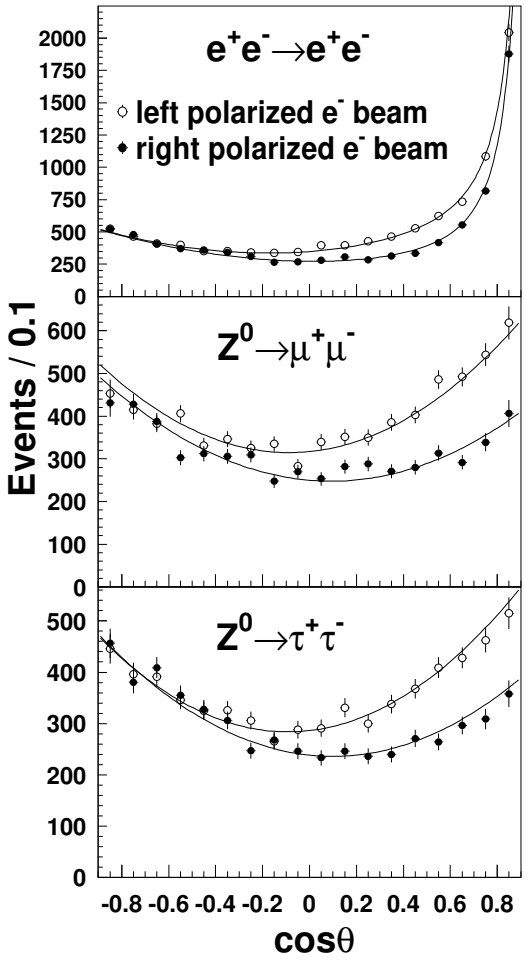

Figure 12: Distributions of the lepton $\cos\theta$ for e^+e^-, $\mu^+\mu^-$, and $\tau^+\tau^-$ candidates from the 1997–1998 data set.

Systematic Errors This measurement is statistically limited. The 1997–1998 dataset, which dominates the sample, typically has statistical errors between 4 and 10 times larger than the total systematic error for the various asymmetry parameters. The systematic errors arise from polarimetry, backgrounds, radiative corrections, $\tau^\pm$ polarization effects ("V−A"), incorrect charge assignment for tracks at large $\cos\theta$, and nonuniformities in the detector efficiency and forward-backward asymmetries. These errors are given in Table 8.

One error deserves some discussion because of its specific relevance to polarized forward-backward asymmetry measurements. The dominant systematic error in the $\tau^\pm$ analysis resulted from final-state $\tau^\pm$ polarization effects, that introduced a selection bias. The term V−A ("vector minus axial vector") used in Table 8 arises from the $(1-\gamma^5)\gamma^\mu$ Lorentz structure of the charged-current Lagrangian that governs $\tau^\pm$ decay. For example, if both τ^+ and τ^- decay to $\pi\nu$, helicity

Table 8: Summary of statistical and systematic uncertainties in units of 10^{-4} for the 1997–1998 data. The superscript on each asymmetry refers to the lepton sample from which it was derived (electrons, muons, or taus).

Source	A_e^e	A_e^μ	A_e^τ	A_μ^μ	A_τ^τ
Statistics	110	130	130	180	180
Polarization	8	8	8	8	8
Backgrounds	5	–	13	–	14
Radiative correction	23	2	2	3	2
V-A	–	–	–	–	18
Charge confusion	–	–	–	7	11
Detector asymmetry	–	–	–	–	4
Nonuniform efficiency	2	–	–	–	–

conservation requires that both pions generally have lower momentum for a left-handed τ^- and right-handed τ^+ and higher momentum otherwise. This effect, which biased the reconstructed event mass, was significant because of the e^- beam polarization, which induced a large and asymmetric $\tau^\pm$ polarization as a function of polar angle. The value of A_e extracted from $\tau^+\tau^-$ final states was not affected, since the overall relative efficiencies for left-handed beam and right-handed beam events were not changed significantly (only the polar angle dependence of the efficiencies was changed).

Results Results for all SLD data sets were combined, taking into account small effects due to correlations in systematic uncertainties (polarization and average SLC center-of-mass energy). From purely leptonic final states, one obtains $A_e = 0.1544 \pm 0.0060$. This A_e result was combined with the left-right asymmetry measurement in the tabulation of leptonic asymmetry results:

$$\begin{aligned} A_e &= 0.1516 \pm 0.0021, \text{ (with } A_{\rm LR}^0\text{)} \\ A_\mu &= 0.142 \pm 0.015, \qquad \text{and} \\ A_\tau &= 0.136 \pm 0.015. \end{aligned} \tag{20}$$

These results are consistent with lepton universality and hence can be combined to obtain A_ℓ, which in the context of the standard model is simply related to the weak mixing angle. The result is discussed in the following section.

5.2.3 Combined Results for $\sin^2\theta_W^{\rm eff}$

Assuming lepton universality, the $A_{\rm LR}$ result and the results on the leptonic left-right forward-backward asymmetries are combined, where small correlated systematics are accounted for, yielding

$$A_\ell = 0.15130 \pm 0.00207. \tag{21}$$

This measurement is equivalent to the determination

$$\sin^2\theta_W^{\rm eff} = 0.23098 \pm 0.00026, \tag{22}$$

where the total error and corresponding systematic error of ± 0.00010 are more precise than those obtained by any other technique.

5.3 Quark Couplings

It is particularly interesting to measure the couplings of individual quark flavors separately, and thereby probe the radiative corrections to the $Zq\bar{q}$ vertex. The b and c quarks are the heaviest charge 1/3 and charge 2/3 quarks, respectively, that are accessible at the Z^0 energy. Potential new-physics signatures may preferentially appear in the heavy-quark couplings, e.g., those that involve Yukawa-type couplings favoring fermions with large masses. More generally, any unexpected difference in quark coupling of one flavor compared with other flavors could be a vital clue toward a solution to the puzzle of fermion family degeneracy. The relatively similar production rates of all quark flavors in Z^0 decays, combined with our ability to tag bottom and charm hadron decays, offers the possibility to test the Z^0 coupling to the individual quark flavors with high precision. In addition to the measurements with heavy quarks, comparing the measurements for the s quark to those of the b quark provides a unique test of the universality of couplings for charge 1/3 quarks.

For most of the measurements in this section, the hadronic Z^0 events were selected by requiring at least seven charged tracks and a visible charged energy of at least 18 GeV. The events were typically required to be well-contained in the high-quality tracking fiducial volume of $|\cos\theta_{\rm thrust}| < 0.7$. The flavor-tagging efficiencies referred to are generally for these selected fiducial events.

5.3.1 R_b and R_c Measurements

The formulation of R_b and R_c as ratios of hadronic cross sections ensures that the propagator (oblique) electroweak radiative corrections and QCD radiative corrections that are common to

all flavors largely cancel, isolating the heavy quark to Z^0 coupling vertex radiative corrections. In the standard model, the large top quark mass introduces a -1.5% correction on R_b (43), compared with the tree-level prediction. Extensions to the standard model can also produce potential deviations in R_b at $\sim$1% (44). The effort toward $< 1\%$ precision R_b measurements has therefore been one of the primary activities of the Z^0-pole experiments. The $Zc\bar{c}$ vertex corrections in the standard model are much smaller, so that any deviations of the measured R_c from the standard-model prediction would signal exotic new physics processes.

At the peak of the R_b and R_c "crisis" in early 1996, the world average for R_b was over 3σ higher than the standard model, whereas that for R_c was over 2σ lower than the standard model (45). SLD's crucial contribution was to introduce an improved analysis method that was eventually adopted by other experiments, resulting in a significant increase in precision.

R_b Measurement Recent R_b measurements have generally adopted a double-tag technique to reduce modeling uncertainty. Events were divided into two hemispheres by the plane perpendicular to the thrust axis, and a b-tagging algorithm was applied to each hemisphere in turn. The measured hemisphere tag rate F_s and event double-tag rate F_d allow the extraction of both R_b and the hemisphere b-tagging efficiency ϵ_b from the data by solving two simultaneous equations:

$$\begin{aligned} F_s &= \epsilon_b R_b + \epsilon_c R_c + \epsilon_{uds}(1 - R_b - R_c), \\ F_d &= C_b \epsilon_b^2 R_b + C_c \epsilon_c^2 R_c + \epsilon_{uds}^2 (1 - R_b - R_c). \end{aligned} \tag{23}$$

The small background tagging efficiencies for uds and charm hemispheres, ϵ_{uds} and ϵ_c, as well as the b-tagging hemisphere correlations $C_b = \frac{\epsilon_b^{\rm double}}{\epsilon_b^2}$ and $C_c = \frac{\epsilon_c^{\rm double}}{\epsilon_c^2}$, were estimated from the Monte Carlo simulation. Furthermore, a standard-model value of R_c was assumed. The R_b statistical error is approximately $\propto 1/\epsilon_b$, whereas the uds and charm systematic errors scale as $\epsilon_{uds}/\epsilon_b$ and ϵ_c/ϵ_b, indicating the need to maintain both high efficiency and high purity for the b tag.

For the preliminary analysis of the 1996–1998 data, a cut on the neural-net $c - b$ separation variable of $S_{cb} > 0.75$ (see Section 4.3) was used as the b tag. Figure 13a shows the hemisphere tagging efficiencies and b purity for the 1997–1998 data as a function of the S_{cb} cut. It can be seen that the measured b-tagging efficiency is in good agreement with the Monte Carlo simulation. At the nominal cut of S_{cb}=0.75, the tagging efficiencies for various flavors were ϵ_{uds}=0.07%, ϵ_c=1.1%, and $\epsilon_b^{\rm data}$=61.8%, which corresponded to a b purity of Π_b=98.3%. The small hemisphere correlation ($1 - C_b = 0.00007 \pm 0.00050$) was due to a combination of several effects related to the IP, b-tagging efficiency dependence on b-hadron momentum, and $\cos\theta$, which were all verified to be small. Table 10 presents the preliminary R_b measurement result and systematic errors,

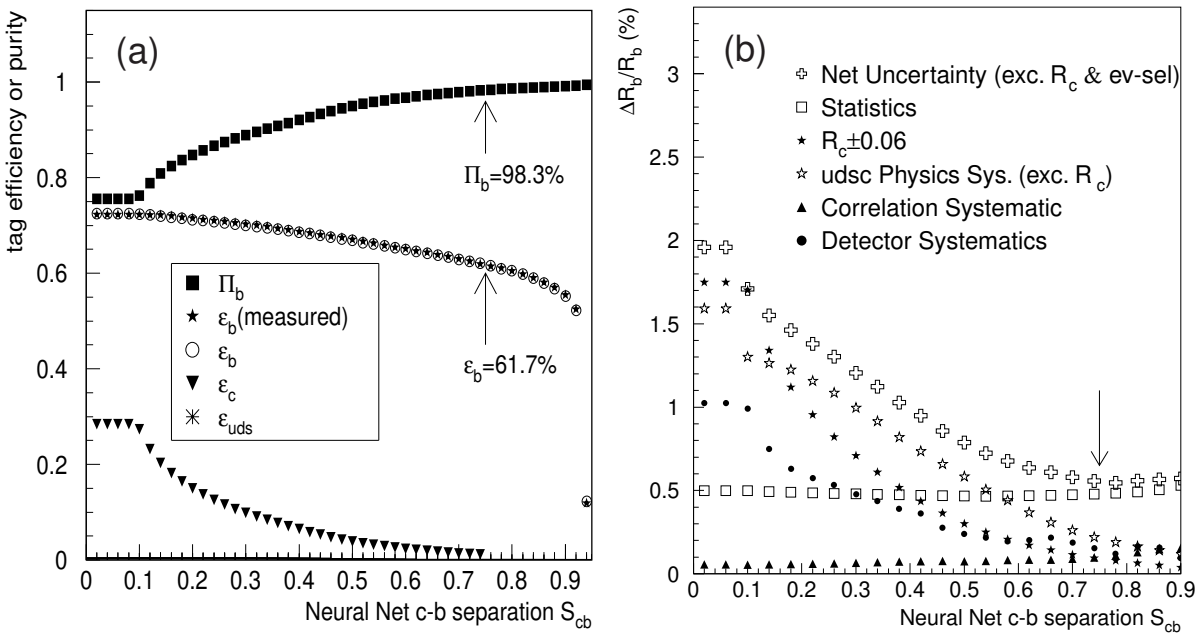

Figure 13: (*a*) *b*-tagging efficiency and purity versus S_{cb} cut. (*b*) R_b statistical and systematic errors versus S_{cb} cut.

combined with the published 1993–1995 result. The choice of the $S_{cb} > 0.75$ cut was the result of an optimization that minimized the total error, as seen in figure 13*b*.

R_c Measurement All R_b measurements now rely on the long *b*-hadron lifetime to exploit the double-tag technique, but the shorter charm lifetime and limited vertex detector resolution prevent the effective use of that technique for R_c measurements in most experiments. This led to more complicated paths for the R_c measurements at LEP, mostly involving techniques that relied on fully or partially reconstructed charm hadrons (48). These methods were not only limited statistically, owing to low efficiency, but also limited systematically at the ± 0.010 level, owing to the lack of clean self-calibration of tagging efficiencies from data. In 1997, SLD introduced an efficient double-tag analysis, which led to, by far, the most precise R_c measurement.

The current preliminary SLD measurement of R_c is based on the 1996–1998 data only. Since the *b* tag separated out the majority of *b* hemispheres with high purity, the R_b analysis used a simple double-tag technique. The R_c measurement, on the other hand, benefited significantly from the additional statistics of $c\bar{c}$ hemispheres in a wider range of S_{cb} values. Although the charm purity was moderate compared with the *b*-tagging purity, the remaining impurities were mainly *b* hemispheres whose fractions could be precisely measured from data. The R_c measurement therefore adopted a multi-tag scheme, which was also used in some LEP R_b measurements.

Table 9: Hemisphere tagging efficiencies and purities for tags used in the R_c analysis, based on the $c-b$ separation variable S_{cb} (boxed efficiency values were measured values from data)

Tag Name	"c-pure"	"c-like"	"b-like"	"b-pure"
Tag Cuts	$S_{cb} < 0.3$	$0.3 < S_{cb} < 0.5$	$0.5 < S_{cb} < 0.75$	$S_{cb} > 0.75$
ϵ_b (%)	2.53	2.96	5.10	62.02
ϵ_c (%)	17.94	5.04	2.29	1.12
ϵ_{uds} (%)	0.05	0.10	0.12	0.07
b purity (%)	15.0	40.9	70.4	98.3
c purity (%)	84.2	55.3	25.1	1.4
uds purity (%)	0.9	3.8	4.5	0.3

Hemispheres were classified into five categories, corresponding to four exclusive categories of b and c tags defined by various S_{cb} ranges and a fifth category with no tag. Table 9 lists the efficiencies and purities of the four different b and c tags for the 1997–1998 data analysis. The measured event rates, $N_{ij}/N_{\rm tot}$ for two hemispheres (categories i versus j), were used in a χ^2 fit for all tag combinations:

$$\chi^2 = \sum_{ij} \frac{N_{ij}/N_{\rm tot} - R_b\epsilon_i^b\epsilon_j^b C_{ij}^b - R_c\epsilon_i^c\epsilon_j^c C_{ij}^c - (1-R_b-R_c)\epsilon_i^{uds}\epsilon_j^{uds}C_{ij}^{uds}}{\sigma(N_{ij}/N_{\rm tot})}. \qquad (24)$$

Besides R_b and R_c, all b-tagging and c-tagging efficiencies (except the c-tagging efficiency for the b-pure tag) were also measured from data. The small uds efficiencies and the hemisphere correlations (C_{ij}) were estimated from the Monte Carlo simulation. The hemisphere correlation factors were found to be very close to 1 for all tags. The essence of this multi-tag scheme is that by looking at the tags opposite the high-purity b-pure and c-pure tags, the flavor composition in the less pure tags was measured from data. However, this efficiency cross calibration is reliable only when the uds fractions are kept as low as as they were in this analysis.

Table 10 summarizes the preliminary R_c result and its systematic errors. The value of the simultaneously fitted R_b was also very consistent with the simple double-tag R_b result. The various measured b- and c-tagging efficiencies were found to be close to the Monte Carlo simulation.

R_b and R_c Summary The SLD measurements of R_b and R_c are summarized in Table 10, where the results were corrected for γ-exchange by $+0.0003$ for R_b and -0.0003 for R_c.

These results are in good agreement with the LEP measurements (48) and the standard model (see Figure 14). Despite the disadvantage of event statistics, the SLD R_b measurement

Table 10: Preliminary results and systematic summary for the R_b and R_c measurements

Observable	R_b	R_c
Data sample	1993–1998	1996–1998
References	$(46, 47)$	$(46, 49)$
Measurement value	0.21641	0.17382
Statistical error	0.00092	0.00308
Monte Carlo statistics	0.00024	0.00095
Event selection bias	0.00026	0.00027
uds and charm physics	0.00042	0.00142
b-hemisphere correlation	0.00023	0.00025
$g \to c\bar{c}, g \to b\bar{b}$	−0.00023	−0.00082
Detector effects	0.00043	0.00079
R_c (± 0.006)	−0.00020	—
R_b (± 0.0015)	—	−0.00020
Total systematic error	0.00080	0.00209

is competitive in precision, and the SLD R_c measurement dominates the world average with a systematic error three times smaller than that of other measurements. The R_b crisis is now believed to have been caused by underestimated detector resolution effects that resulted in an excess of light-flavor tags in one of the early LEP measurements. The R_c deviation from the standard model was related to incorrect assumptions on charm production and decay branching ratios, which were later measured directly from the data. Recent measurements are less prone to these problems as improved analysis methods have largely reduced the sensitivity to physics and detector modeling uncertainties.

5.3.2 A_b and A_c Measurements

The direct measurements of A_b and A_c at SLD are mostly sensitive to deviations in the right-handed $Zb\bar{b}$ and $Zc\bar{c}$ couplings, which have unambiguous standard-model predictions with small radiative corrections. Most proposed extensions to the standard model predict changes in the left-handed $Zb\bar{b}$ coupling, with little or no effect on the right-handed coupling. Any deviations from the standard-model prediction for A_b and A_c will therefore be sensitive to exotic new physics processes.

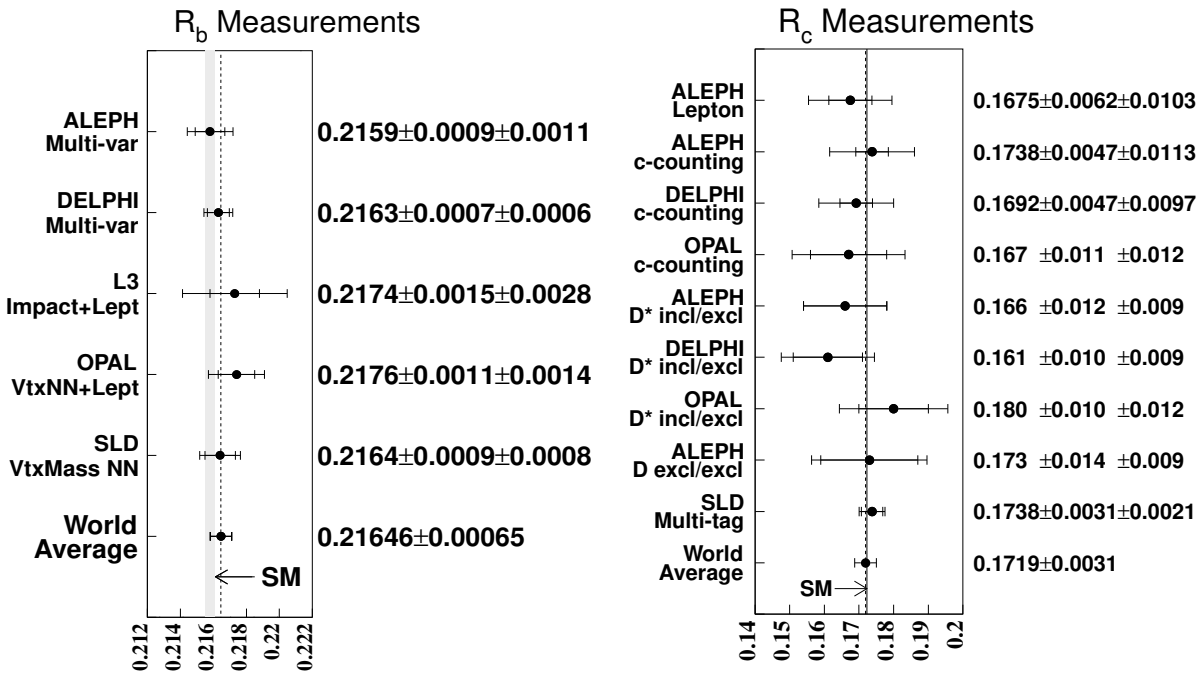

Figure 14: Summary of R_b and R_c measurements from LEP and SLD. The shaded band for the R_b standard model (SM) prediction reflects the uncertainty in the top quark mass.

The heavy-quark asymmetry analyses typically involved quark flavor tags to enrich the fraction of the desired heavy-quark species. The primary $Q\overline{Q}$ production axis was typically approximated by the event thrust axis. Various techniques were then used to determine the direction of the quark as opposed to the antiquark. We refer to this process as the quark charge assignment. All analyses adopted maximum likelihood fits to the polarized differential cross section (see Equation 8) as a function of $\cos\theta$, and events were weighted appropriately based on the correct quark charge assignment probability, event quark-flavor fractions, and electron beam helicity. The information drawn from this procedure is equivalent to that obtained from the left-right forward-backward asymmetry $\tilde{A}^Q_{\rm FB}$ at first order. The measurements were corrected for QCD and QED radiative effects. The dependence of radiative corrections on center-of-mass energy was negligible.

In the following, we first describe the analysis procedure, emphasizing features that are special to SLD. The results are presented in Table 11.

A_b and A_c with Leptons The use of leptons to identify heavy-hadron decays has been a traditional technique for the b- and c-asymmetry measurements. The lepton tags not only enrich the b- and c-quark events but also provide the crucial separation between quark and antiquark.

In this SLD measurement, the estimation of correct charge assignment probability for this $Q/\overline{Q}$ separation was based on the probabilities from the Monte Carlo for the candidate lepton to be from various sources, e.g., $b \to \ell$, $b \to c \to \ell$, $c \to \ell$ or lepton misidentification, etc. This analysis benefited from the well-understood kinematics of semileptonic decays of heavy hadrons and the generally well-measured decay branching ratios for the various lepton sources. Besides the conventional lepton total momentum and transverse momentum with respect to the jet axis, the vertex mass b tag and other vertexing observables were also used to improve the lepton source classification. A special variable assisting this separation was the lepton longitudinal position along the vertex axis, L/D (see Section 4.2), which had significant resolving power between direct secondary $b \to \ell$ and cascade tertiary $b \to c \to \ell$ leptons. The major sources of physics systematic uncertainty were the various semileptonic branching ratios and B mixing rates, which were taken from the LEP combined lepton fit results (48).

A_b with Jet Charge The use of momentum-weighted track charge (more commonly refered to as "jet charge") to sign the b-quark direction is now a standard technique for b-asymmetry measurements. The method is based on the correlation between the primary quark charge and the net charge of high-momentum tracks in the jet. In this analysis, $b\bar{b}$ events were selected by requiring at least one hemisphere with a vertex mass tag of $M_{\rm corr} > 2\,{\rm GeV}$. The momentum-weighted track charge was calculated from

$$Q = \sum_{\rm tracks} q_i \cdot {\rm sign}(\vec{p}_i \cdot \hat{T}) |(\vec{p}_i \cdot \hat{T})|^\kappa, \tag{25}$$

where q_i and $\vec{p}_i$ are the charge and momentum vector of track i, $\hat{T}$ is the thrust axis direction and κ was chosen to be 0.5 to optimize the charge determination.

The correct charge assignment probability was calibrated from data. The approximately Gaussian shape of the jet charge distribution allowed a simple parameterization of the correct charge assignment probability as $p_b(|Q|) = 1/(1 + e^{-\alpha_b}|Q|)$. The widths of the hemisphere charge sum and difference distributions were used to calculate the single parameter α_b. The correct charge assignment probability was evaluated for each event and used in the likelihood fit. On average, this probability was ∼69%. The small *udsc* background was subtracted based on the Monte Carlo simulation, but the b purity was measured from data using the double-tag technique, as in the case of the R_b measurement. There was a small hemisphere charge correlation, analogous to the hemisphere tag correlation in R_b analysis, which was estimated from the Monte Carlo.

A_c with $D^{(*)}$ and inclusive $D^{*+} \to D^0\pi^+$ A traditional way of tagging charm is simply to reconstruct $D^{(*)}$ decays. Two measurements of A_c were performed. The first analysis used fully or partially reconstructed D^{*+}, D^+, and D^0 mesons;[4] the second used inclusively reconstructed $D^{*+} \to D^0\pi^+$ decays. These methods not only selected the $c\bar{c}$ events, the $D^{(*)}$ ($\overline{D}^{(*)}$) mesons naturally tagged c ($\bar{c}$) quarks with high purity. The behavior of the random combinatorial background (RCBG) events can be conveniently studied with the events in the mass sidebands. A simple b tag with mass requirement of $M_{\rm corr} > 2\,{\rm GeV}$ was used to veto real $D^{(*)}$ background from $b\bar{b}$ events.

The effective rejection of RCBG using precision vertexing allowed the inclusion of many decay modes in this measurement. The exclusive $D^{*+} \to D^0\pi^+$ analysis utilized four D^0 decay modes: $K^-\pi^+$, $K^-\pi^+\pi^0$, $K^-\pi^+\pi^-\pi^+$, and $K^-\ell^+\nu$. The direct D meson reconstructions used two decay modes: $D^+ \to K^-\pi^+\pi^+$ and $D^0 \to K^-\pi^+$. CRID kaon identification was used for the $D^0 \to K^-\pi^+$ mode. The sample of all $D^{(*)}$ candidates had the following composition: $c \to D/b \to D/{\rm RCBG}$=71%/7%/22%.

The inclusive $D^{*+} \to D^0\pi_s^+$ analysis exploited the fact that a high-momentum leading D^* in a $c\bar{c}$ jet would follow the jet axis very closely. Because of the low Q^2 of the $D^{*+} \to D^0\pi_s^+$ decay, the π_s would also travel very close to the jet axis. The π_s candidates having momentum transverse to the jet axis $p_T^2 < 0.01\ ({\rm GeV}/c)^2$ were selected with a signal-to-background ratio of 1:2 and an efficiency three times higher than the exclusively reconstructed sample. For the combined result in Table 11, the overlapping candidates between the two analyses were removed from the inclusive analysis for the combined A_c result.

A_b and A_c with Vertex Charge and Kaon Tag The most precise A_b and A_c measurements at SLD were based on two novel quark charge assignment techniques: vertex charge and identified kaon charge.

The analysis selected b and c hemispheres mainly using the neural-net $c-b$ separation variable S_{cb} (see Section 4.3). The hemisphere b tag required $S_{cb} > 0.9$ and $M_{\rm corr} < 7\,{\rm GeV}$, and the c tag required $S_{cb} < 0.4$ and a momentum sum of all secondary tracks > 5 GeV/c.

A clean reconstruction of the secondary vertex charge tagged the heavy-quark charge. This is especially beneficial in the case of b hadrons because both lepton and jet-charge techniques suffer from dilution from neutral B-meson mixing. This method required clean and efficient separation of primary and secondary tracks, fortunately achievable with the precision IP and tracking at SLD. The secondary track selection procedure can be found in Section 4.2. Figure 15 shows the

[4]Charge conjugate modes are implied throughout this paper.

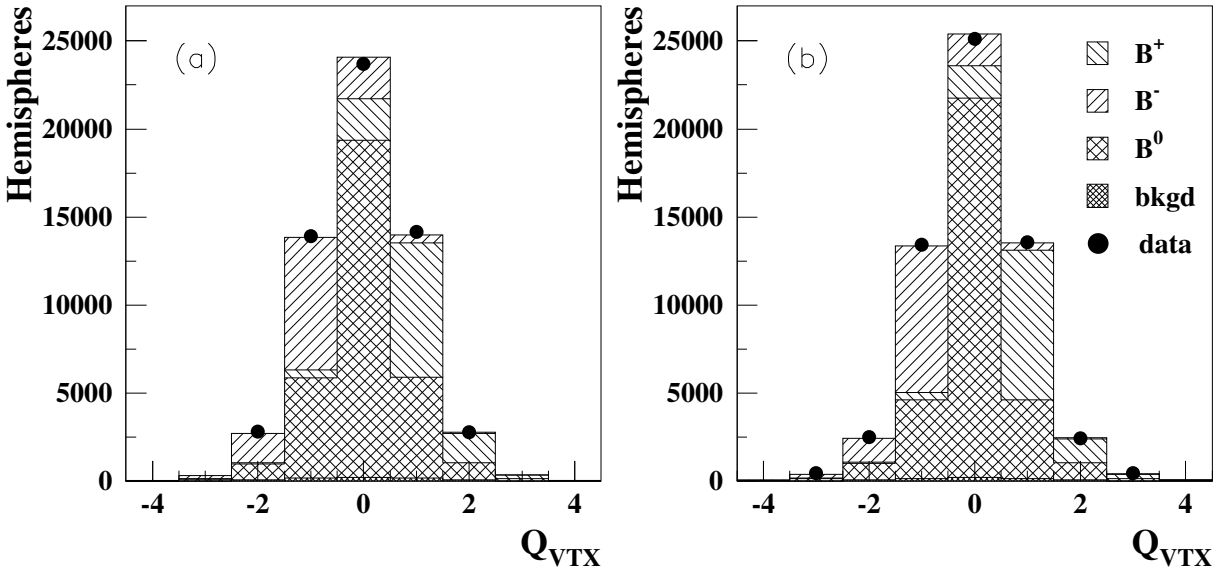

Figure 15: Vertex charge distributions for the b-tagged hemispheres, (a) with fully fitted tracks and (b) including VXD track segments. The "B^0" category shown in the plot includes all neutral b hadrons.

vertex charge distributions for the b-tagged hemispheres, demonstrating good agreement between data and Monte Carlo and a clear $+/-$ charge separation. Note that the inclusion of the VXD track segments in the charge reconstruction noticeably improved the correct charge assignment fraction. For the b- (c-) tagged hemispheres, the fraction of hemispheres with the secondary decay identified as charged was 56% (45%), and the correct b- (c-) quark charge identification probability was 81% (91%).

Another quark charge assignment technique was to use the dominant $b \to c \to s \to K^-$ and $c \to s \to K^-$ decay chains, in which the $K^\pm$ were identified by the CRID. However, in the case of b hemispheres, the additional contribution from the $K^\pm$ tag was found to be small. This was mostly due to the fact that the hemispheres with no vertex-charge tag contained an enhanced fraction of neutral B mesons, which had inherently poorer $K^\pm$ tag performance due to B mixing. On the other hand, a $K^\pm$ tag fraction of 30% and a correct c-quark charge identification probability of 86% for the c-tagged hemispheres, provided a very effective additional charge assignment contribution. Therefore, the A_b analysis used the vertex-charge tag only, while the A_c analysis used both vertex-charge and kaon-charge tags.

The vertex-charge and kaon-charge tags were used to make a joint quark charge assignment in the A_c analysis. In cases of conflict between a vertex-charge and kaon-charge assignment in the same hemisphere, no charge assignment was made. Thanks to the high efficiency and

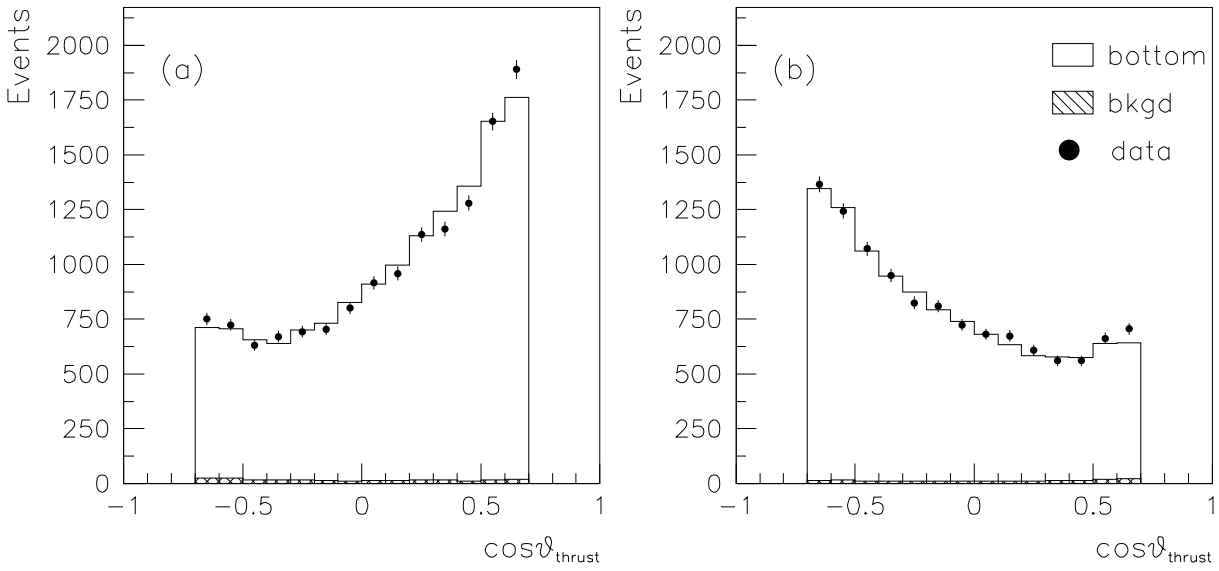

Figure 16: Event thrust $\cos\theta$ distributions for (a) left- and (b) right-handed beams in the vertex-charge A_b analysis, for data (points) and Monte Carlo simulation (histograms).

the good performance of the quark charge assignment, we were able to determine the event flavor composition and quark charge assignment probability simultaneously from data using a hemisphere double-tag technique. This procedure used the small *uds* efficiencies and hemisphere correlations from the Monte Carlo simulation and assumed the world average values of R_b and R_c.

For the A_b and A_c fits, events with either hemisphere having a b tag were classified as $b\bar{b}$ events, whereas events with either hemisphere having a c tag and no hemisphere having a b tag were classified as $c\bar{c}$ events. Events with two hemispheres having the same charge were discarded, and events with two hemispheres having the opposite charge were weighted by the joint correct charge assignment probability. The $b\bar{b}$ sample had a b purity of $97.5 \pm 0.5\%$ and a correct b-quark charge fraction of $81.5 \pm 0.5\%$. The b-quark $\cos\theta$ distributions of b-tagged events with vertex charge are shown in Figure 16. The most significant systematic uncertainty was due to charge assignment calibration statistics.

A_b and A_c Summary Table 11 summarizes results for the various A_b and A_c measurements. The raw measured asymmetry parameters were corrected for QCD and QED radiative effects. The QED corrections for A_b and A_c were rather small: -0.2% and $+0.2\%$, respectively. These were already taken into account for results in Table 11. The size of these corrections can be compared to the analogous QED corrections of 2.5% and 9% applied to unpolarized asymmetries measured at LEP.

Table 11: Summary of A_b and A_c results, detailing statistical and systematic uncertainties. All measurements are preliminary except for the A_c measurement with $D^{(*)}$.

Observable	A_b			A_c		
Measurement type	Lepton	Jet-Q	Vtx-Q	Lepton	$D^{(*)}$	Vtx+K
Data sample	1993–98	1993–98	1996–98	1993–98	1993–98	1996–98
References	(50, 51)	(46, 52)	(46, 54)	(50, 51)	(53)	(46, 54)
Measurement value	0.924	0.907	0.921	0.589	0.688	0.673
Statistical error	0.030	0.020	0.018	0.055	0.035	0.029
Monte Carlo statistics	0.005	–	0.003	0.017	–	0.004
Calibration statistics	–	0.014	0.013	–	–	0.021
Calibration systematic	–	0.016	0.007	–	–	0.009
Detector effects	0.010	0.008	0.003	0.020	–	0.003
b-tag purity	0.009	0.005	0.007	0.036	–	0.003
Br(semi-ℓ) & B mixing	0.012	0.000	0.000	0.022	0.010	0.000
b, c decay/prod. model	0.011	0.000	0.003	0.018	0.018	0.004
$g \to c\bar{c}, g \to b\bar{b}$	0.002	0.001	<0.001	0.001	<0.001	0.002
Beam polarization	0.005	0.005	0.005	0.004	0.003	0.004
QCD correction	0.005	0.003	0.003	0.005	0.003	0.001
A_c (± 0.035)	0.003	0.001	0.001	–	–	–
A_b (± 0.035)	–	–	–	0.008	−0.003	−0.001
Total systematic error	0.023	0.024	0.018	0.053	0.021	0.024

Whereas the QED corrections were generally calculated reliably with small uncertainties, the QCD corrections had significant theoretical uncertainties and were sensitive to analysis details. The total integrated QCD correction was at the $\sim$ 3.5% level for an ideal measurement of either A_{FB}^{Q} or A_Q. However, the analysis event selection and final-state particle reconstructions typically tended to suppress the events with hard gluon radiation and therefore only needed reduced QCD corrections. This can be understood because b tags were typically more efficient for high-momentum b hadrons, and high-x D^* reconstruction and high-momentum lepton selections also favored high-momentum c and b quarks in two-jet events. The QCD corrections were scaled down by analysis-dependent factors ranging between 25% and 75%. The SLD A_b and A_c analyses used a first-order QCD correction calculated by Stav & Olsen (56), which included

heavy-quark mass effects with explicit $\cos\theta$ dependence. The second-order QCD corrections and their uncertainties were based on the prescription found in Reference (57).

The individual A_b and A_c measurements were combined, taking into account systematic correlations. The various A_b measurements had significant event sample overlaps. A statistical correlation matrix was built, taking into account the different weight of each event used in the analysis. The effective correlations obtained from this procedure were as follows:

Lepton	versus	Jet-Q:	22%,
Lepton	versus	Vtx-Q:	15%,
Jet-Q	versus	Vtx-Q:	32%.

The combined result also included an older measurement of A_b using the K tag alone from the 1994–1995 data (55). Given the much smaller samples for the various A_c analyses, their statistical correlations were deemed to be small. The combined preliminary SLD A_b and A_c results are

$$\begin{aligned} A_b &= 0.916 \pm 0.021, \\ A_c &= 0.670 \pm 0.027. \end{aligned} \tag{26}$$

Figure 17 lists the individual A_b and A_c measurements, as well as the SLD average, along with the indirect measurements derived from the LEP A_{FB} measurements, assuming a measured A_e from the SLD and LEP combined A_{lepton} result of $A_e = 0.1501 \pm 0.0016$.

5.3.3 A_s Measurement

An important test of the standard model is to verify the universality of coupling strengths of the Z^0 boson to fermions with the same charge and weak isospin. As described in the previous section, a number of precise measurements of heavy-quark asymmetries have been performed, but few measurements of light-quark asymmetries have been carried out, owing to the lack of clear experimental signatures to separate $Z^0 \to u\overline{u}, d\overline{d}, s\overline{s}$ decays from one another. Nevertheless, it is possible, albeit with low efficiency, to select a fairly pure sample of $Z^0 \to s\overline{s}$ decays by requiring each event hemisphere to contain high-momentum kaons, as outlined below.

In the A_s analysis (58), $Z^0 \to b\bar{b}$ and $Z^0 \to c\bar{c}$ decays were suppressed by requiring the events to contain no more than one well-measured track with normalized impact parameter in the transverse plane $d/\sigma_d > 2.5$. Charged kaons were identified with the CRID and required to have $p > 9\,\text{GeV}/c$ to provide a sample 91.5% pure in $K^{\pm}$. Neutral kaons were identified via their decay into $\pi^+\pi^-$ final states with a purity of 90.7%. An event was tagged as $Z^0 \to s\overline{s}$ if one

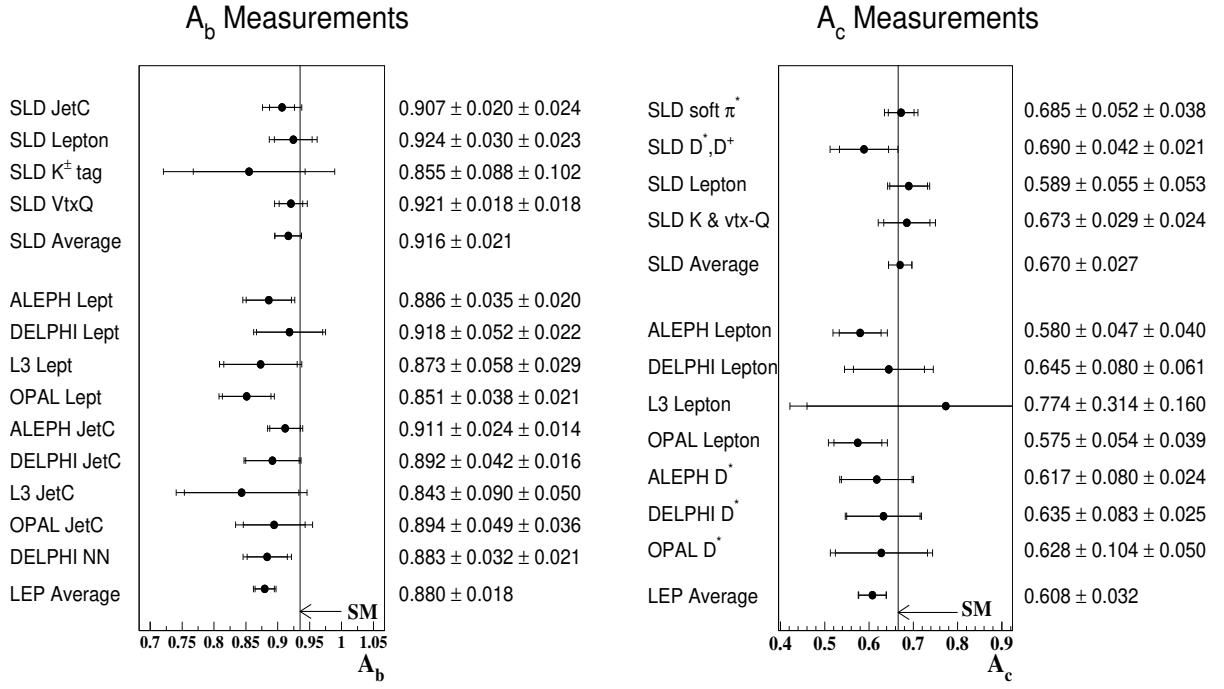

Figure 17: Comparison between the A_b and A_c measurements by SLD and the A_b and A_c values derived from the indirect $A_{\rm FB}^b$ and $A_{\rm FB}^c$ measurements at LEP.

hemisphere contained a $K^\pm$ candidate and the other contained either an oppositely charged $K^\pm$ or a K_S^0 candidate. The respective $s\bar{s}$ purities for K^+K^- and $K^\pm K_S^0$ events were estimated to be 73% and 60% from the Monte Carlo simulation, with an overall $s\bar{s}$ event selection efficiency of 2.6%. Identification of the s-quark hemisphere relied on the $K^\pm$ charge and was correctly assigned with a probability of 97.5% for K^+K^- events and 85.0% for $K^\pm K_S^0$ events.

A maximum likelihood method was used to extract A_s from the s-quark $\cos\theta$ distributions for left- and right-handed electrons in both samples (see Figure 18). From the figure, it is apparent that $b\bar{b}$ and $c\bar{c}$ backgrounds have asymmetries with the same sign as the signal asymmetry, but that $u\bar{u}$ and $d\bar{d}$ events contribute with the opposite sign. Therefore, uncertainties in the modeling of light quarks have the greatest impact on the value of A_s. Using the 1993–1998 data, the analysis determined $A_s = 0.895 \pm 0.066$ (stat.) ± 0.062 (syst.), where the systematic error is dominated by uncertainties in the $u\bar{u}$ and $d\bar{d}$ contributions to the $\cos\theta$ distributions. To reduce modeling uncertainties, these contributions were constrained using the data, as was the s-quark correct charge assignment probability.

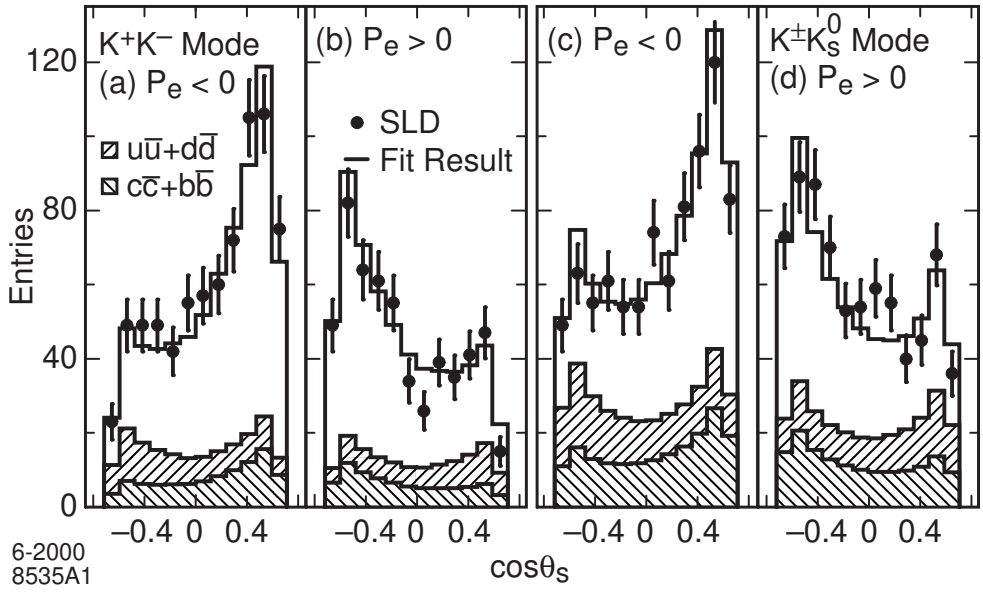

Figure 18: Distributions of the s-quark $\cos\theta$ for data (points) in (a) K^+ K^- events with $\mathcal{P}_e < 0$, (b) K^+ K^- events with $\mathcal{P}_e > 0$, (c) $K^\pm$ K^0_S events with $\mathcal{P}_e < 0$, (d) $K^\pm$ K^0_S events with $\mathcal{P}_e > 0$. The histograms represent the result of the fit.

6 B^0_s–$\overline{B}^0_s$ MIXING

6.1 Introduction

The special features of the SLC and SLD environment were particularly well-suited for studies of B decays. Measurements of the average b-hadron lifetime (59) and of the B^+ and B^0_d lifetimes (60) provided the initial impetus for the development of the inclusive topological vertexing described above. Recent updates of the B^+ and B^0_d lifetime measurements (61) are among the most precise available to date and have helped establish a small but significant difference between the lifetimes of the B^+ and B^0_d mesons, in agreement with predictions based on the heavy-quark expansion technique (62, 63).

Investigations of the properties of B meson decays at SLD have included the search for charmless hadronic decays into two-body and quasi–two-body final states (64), the search for flavor-changing neutral-current $b \to s$ gluon decays (65), and the measurement of the charm hadron yield (66).

A topic of particular interest is the study of the time dependence of B^0_d–$\overline{B}^0_d$ and B^0_s–$\overline{B}^0_s$ mixing. Experimental studies of mixing exploit all the special features of the SLC/SLD environment, i.e., beam polarization, small beam spot, high-resolution vertexing, and good particle identification.

Below, we focus on B_s^0–$\overline{B}_s^0$ mixing studies in some detail. A recent study of B_d^0–$\overline{B}_d^0$ mixing with a kaon tag is described elsewhere (67).

6.2 Theory

The neutral B meson system consists of B_q^0 and $\overline{B}_q^0$ flavor eigenstates, which are superpositions of heavy and light mass eigenstates ($q = d$ and s for B_d^0 and B_s^0 mesons, respectively). The mass eigenstates evolve differently as a function of time, resulting in time-dependent B_q^0–$\overline{B}_q^0$ oscillations with a frequency equal to the mass difference Δm_q between the heavy and light eigenstates. As a consequence, an initially pure $|B_q^0\rangle$ state may be found to decay as $|B_q^0\rangle$ or $|\overline{B}_q^0\rangle$ at a later time t with a probability equal to

$$P(B_q^0 \to B_q^0) = \frac{\Gamma}{2} e^{-\Gamma t}(1 + \cos \Delta m_q \, t) \quad \text{or} \tag{27}$$

$$P(B_q^0 \to \overline{B}_q^0) = \frac{\Gamma}{2} e^{-\Gamma t}(1 - \cos \Delta m_q \, t). \tag{28}$$

(Here we neglected the lifetime difference between mass eigenstates.)

The oscillation frequency can be computed to be (68)

$$\Delta m_q = \frac{G_F^2}{6\pi^2} m_{B_q} m_t^2 F(m_t^2/M_W^2) f_{B_q}^2 B_{B_q} \eta_{\mathrm{QCD}} \left| V_{tb}^* V_{tq} \right|^2 , \tag{29}$$

where G_F is the Fermi constant, m_{B_q} is the B_q^0 hadron mass, m_t is the top quark mass, M_W is the W boson mass, F is a function defined in Reference (69), and η_{QCD} is a perturbative QCD parameter. The parameter B_{B_q} and the decay constant f_{B_q} parameterize hadronic matrix elements. For further details, see the review by Gay (70). Much of the interest in B mixing stems from the fact that a measurement of the B_d^0 (B_s^0) oscillation frequency allows the magnitude of the poorly known CKM matrix element V_{td} (V_{ts}) to be determined (see Equation 29). However, the extraction of $|V_{td}|$ from the fairly precisely measured value $\Delta m_d = 0.472 \pm 0.017$ ps^{-1} (71) is affected by a theoretical uncertainty of about 20% in the product $f_{B_q}\sqrt{B_{B_q}}$ (72). Uncertainties are reduced for the ratio

$$\frac{\Delta m_s}{\Delta m_d} = \frac{m_{B_s} f_{B_s}^2 B_{B_s}}{m_{B_d} f_{B_d}^2 B_{B_d}} \left| \frac{V_{ts}}{V_{td}} \right|^2 = \frac{m_{B_s}}{m_{B_d}} (1.16 \pm 0.05)^2 \left| \frac{V_{ts}}{V_{td}} \right|^2 , \tag{30}$$

which indicates that the ratio $|V_{ts}/V_{td}|$ can be determined with an uncertainty as small as 5% (72).

The CKM matrix describes weak quark mixing in the standard model and contains an irreducible phase that provides the mechanism for CP violation in weak decays. This matrix can be written in terms of four fundamental parameters: $\lambda = \sin\theta_{\mathrm{Cabibbo}}$, A, ρ, and η [as defined in the

Wolfenstein parameterization (73)]. The value of η is directly related to the amount of CP violation. The parameters λ and A are well-measured, $\lambda = 0.2237 \pm 0.0033$ and $A = 0.819 \pm 0.040$ (74), but ρ and η are among the least-known parameters of the standard model. In terms of these parameters, we have $\Delta m_d \propto |V_{td}|^2 \simeq A^2\lambda^6[(1-\bar{\rho})^2 + \bar{\eta}^2]$ and $\Delta m_s \propto |V_{ts}|^2 \simeq A^2\lambda^4$, where $\bar{\rho} = \rho(1-\frac{\lambda^2}{2})$ and $\bar{\eta} = \eta(1-\frac{\lambda^2}{2})$. As a result, the combination of B_d^0 and B_s^0 mixing provides one of the strongest constraints on ρ and η, and therefore on CP violation, in the standard model.

6.3 Experimental Ingredients

Experimental studies of B_s^0–$\overline{B}_s^0$ mixing require two main ingredients: (a) the measurement of the B_s^0 decay proper time, and (b) the determination of the B_s^0 or $\overline{B}_s^0$ flavor at both production and decay to classify the decay as either "mixed" (if the tags disagree) or "unmixed" (otherwise). The significance for a B_s^0 oscillation signal can be approximated by (75)

$$S = \sqrt{\frac{N}{2}}\, f_s\, [1 - 2\,w]\; e^{-\frac{1}{2}(\Delta m_s \sigma_t)^2}, \tag{31}$$

where N is the total number of decays selected, f_s is the fraction of B_s^0 mesons in the selected sample, w is the probability of incorrectly tagging a decay as mixed or unmixed (i.e., the mistag rate), and σ_t is the proper time resolution. The proper time resolution depends on both the decay length resolution σ_L and the momentum resolution σ_p according to $\sigma_t^2 = (\sigma_L/\gamma\beta c)^2 + (t\,\sigma_p/p)^2$. Based on the Wolfenstein parameterization, we see that $\Delta m_s/\Delta m_d \simeq 1/\lambda^2$, which is of the order of 20. Therefore, B_s^0 oscillations are expected to be much more rapid than B_d^0 oscillations. The ability to resolve such rapid oscillations thus requires excellent decay length resolution and benefits from having a low mistag rate and a high B_s^0 purity. The importance of decay length resolution is illustrated in Figure 19, which shows the fraction of b-hadron decays tagged "mixed" as a function of proper time for $\Delta m_s = 20\,\mathrm{ps}^{-1}$, B_s^0 purity of 18%, mistag rate $w = 0.25$, relative momentum resolution $\sigma_p/p = 10\%$, and either $\sigma_L = 200\ \mu$m or $\sigma_L = 60\ \mu$m, the former being typical for LEP experiments and the latter typical for SLD. It is clear from Figure 19 that the decay length resolution is the most critical ingredient for sensitivity to the large B_s^0 oscillation frequencies that are expected.

6.4 Analysis Methods

SLD performed three separate analyses using the 1996–1998 data: "D_s+tracks," "lepton+D," and "charge dipole." These analyses differ in the way the B_s^0 decay candidates were reconstructed and the flavor at decay was tagged (see below).

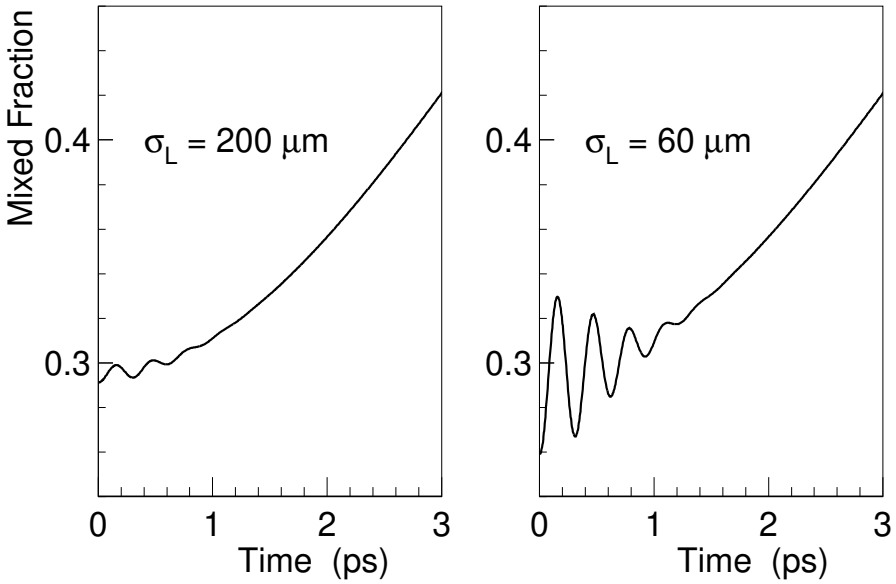

Figure 19: Fraction of b-hadron decays tagged "mixed" as a function of proper time for two different decay length resolutions, $\sigma_L = 200\ \mu$m and 60 μm. Other relevant parameters are $\Delta m_s = 20\,\mathrm{ps}^{-1}$, $f_s = 18\%$, $w = 0.25$, and $\sigma_p/p = 10\%$.

Common to all analyses was the determination of the production flavor (also known as the initial-state tag). This was achieved by combining several tagging techniques. The most powerful technique relied on the large polarized forward-backward asymmetry in $Z^0 \to b\bar{b}$ decays and was unique to SLD. In this case, a left- (right-) handed incident electron tagged the forward hemisphere quark as a b ($\bar{b}$) quark. The probability of correctly tagging a b quark at production is expressed as

$$P_A(\cos\theta) = \frac{1}{2} + A_b \, \frac{A_e - \mathcal{P}_e}{1 - A_e\mathcal{P}_e} \, \frac{\cos\theta}{1 + \cos^2\theta} \ . \tag{32}$$

The average mistag rate was 28% for an average electron beam polarization of 0.73. Other tags were also used. They relied on charge information from the hemisphere opposite that of the B_s^0 decay candidate (i.e., the hemisphere expected to contain the other b hadron in the event): (a) momentum-weighted jet charge, (b) secondary vertex charge, (c) charge of kaon from the dominant decay transition $b \to c \to s$, (d) charge of lepton from the direct transition $b \to \ell^-$, and (e) charge dipole. The first four of these tags were used to measure A_b and/or A_c, as described in Section 5.3, and the charge dipole tag is described below. These tags were estimated to have efficiencies (mistag rates) of 100% (66%), 43% (75%), 16% (74%), 9% (74%), and 17% (70%), respectively. The five tags were combined to yield an efficiency of 100% and a mistag rate of 28%. Overall, the average mistag rate was estimated to be 22%–25%, depending

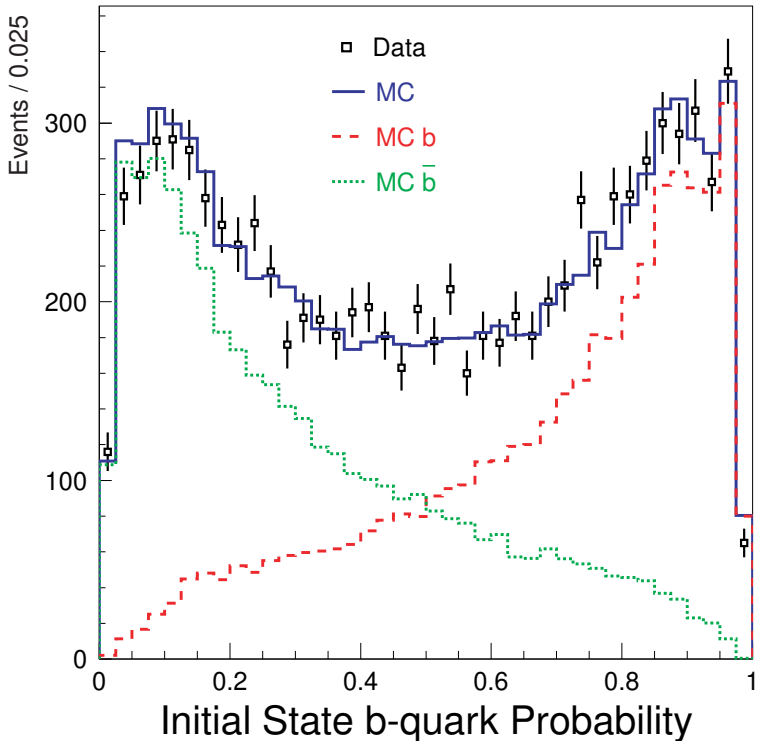

Figure 20: Distribution of the computed initial state b-quark probability for data (points) and Monte Carlo (histograms), for the events selected in the charge dipole analysis.

on the $\cos\theta$ acceptance of each particular analysis. Figure 20 shows the combined b-quark probability distributions for data and Monte Carlo in the charge dipole analysis and indicates a clear separation between b and $\bar{b}$ quarks.

Also common to all analyses was the method to estimate the b-hadron momentum. It utilized the following information: the momentum of all secondary tracks, the energy deposited in the electromagnetic section of the calorimeter, and kinematical constraints stemming from the known b-hadron mass and the e^+e^- collision center-of-mass energy.

6.4.1 D_s+Tracks Analysis

The D_s+tracks analysis (76) aimed to partially reconstruct the decay $B_s^0 \to D_s^- X$ with full reconstruction of the cascade decay $D_s^- \to \phi\pi^-$ or $K^{*0}K^-$. As a result, the analysis achieved a high B_s^0 purity and excellent decay length resolution but at the price of fairly low efficiency. D_s candidates were selected with a neural-network algorithm combining kinematical quantities and particle identification information to yield a sample of 280 $D_s^- \to \phi\pi^-$ and 81 $D_s^- \to K^{*0}K^-$ candidates. These D_s candidates were vertexed with one or more charged tracks to form the B_s^0

decay. A D_s^- (D_s^+) tagged the decay flavor as B_s^0 ($\overline{B}_s^0$). Table 12 summarizes the performance of this analysis. Increased sensitivity to B_s^0 decays was obtained by separately parameterizing decays with a reconstructed track charge sum equal to or different from zero. For example, B_s^0 purities above 50% were obtained for the neutral sample. Furthermore, $B_s^0 \to D_s^- \ell^+ \nu_l X$ candidates were identified and assigned both higher purity and lower decay flavor mistag rate than the average.

6.4.2 Lepton+D Analysis

The lepton+D analysis (77) attempted to reconstruct $B_s^0 \to D_s^- \ell^+ \nu_l$ decays, where the D_s^- decay was not reconstructed exclusively but rather with the inclusive topological vertexing technique described in earlier sections. The B_s^0 vertex was reconstructed by intersecting the lepton trajectory with the D trajectory, which is estimated from the inclusively reconstructed D vertex and its net momentum vector. Direct leptons from $b \to \ell$ transitions were selected with a neural-network algorithm that relied on the following variables: the transverse momentum of the lepton with respect to the B vertex direction (vector stretching from the IP to the B vertex), the B decay length, the transverse momentum of the lepton with respect to the D vertex direction (vector stretching from the B vertex to the D vertex), the mass of the charged tracks associated with the B decay, and the distance of closest approach of the lepton to the B vertex. This algorithm effectively suppressed leptons from $b \to c \to \ell$ transitions, which produce leptons with sign opposite that of direct leptons and thus dilute the decay flavor tag. To enhance the B_s^0 purity, the sum of lepton and D vertex track charges was required to be zero. The purity was further enhanced from 16% to 39% in the subsample containing an opposite-sign lepton-kaon pair. Table 12 gives performance parameters.

6.4.3 Charge Dipole Analysis

The charge dipole analysis (77) was based on a novel method to inclusively reconstruct decays of the type $B_s^0 \to D_s^- X$. For each candidate hemisphere, events were selected in which both a secondary (B) and a tertiary (D) vertex could be resolved. A "charge dipole" δQ was then defined as the distance between secondary and tertiary vertices signed by the charge difference between them such that $\delta Q < 0$ ($\delta Q > 0$) tagged B^0 ($\overline{B}^0$) decays (see Figure 21). This analysis, first developed by SLD, relied heavily on the ability to recognize secondary tracks (from the B-decay point) versus tertiary tracks (from the D-decay point). It also benefited from the fact that B_s^0 decays yield mostly charged secondary and tertiary vertices, whereas B_d^0 mesons tend

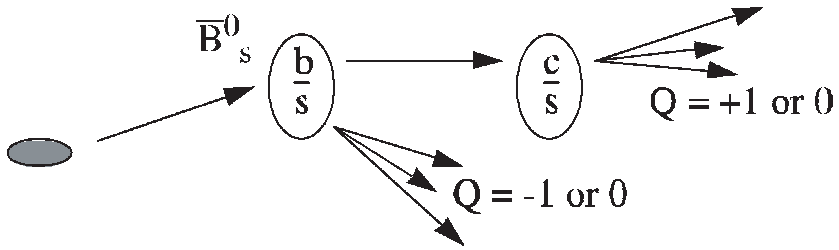

Figure 21: Sketch illustrating the decay cascade structure for $B_s^0 \to D_s^- X$ decays.

to produce neutral vertices since they decay mostly into neutral D mesons.

As in the lepton+D analysis, the total charge of all secondary and tertiary tracks was required to be zero, in order to enhance the B_s^0 purity from 10% to 15%. Figure 22 shows the δQ distribution, illustrating the clear separation between B and $\overline{B}$ decays. The average decay flavor mistag rate was estimated to be 24%, driven mostly by decays of the type $B_s^0 \to D\overline{D}X$

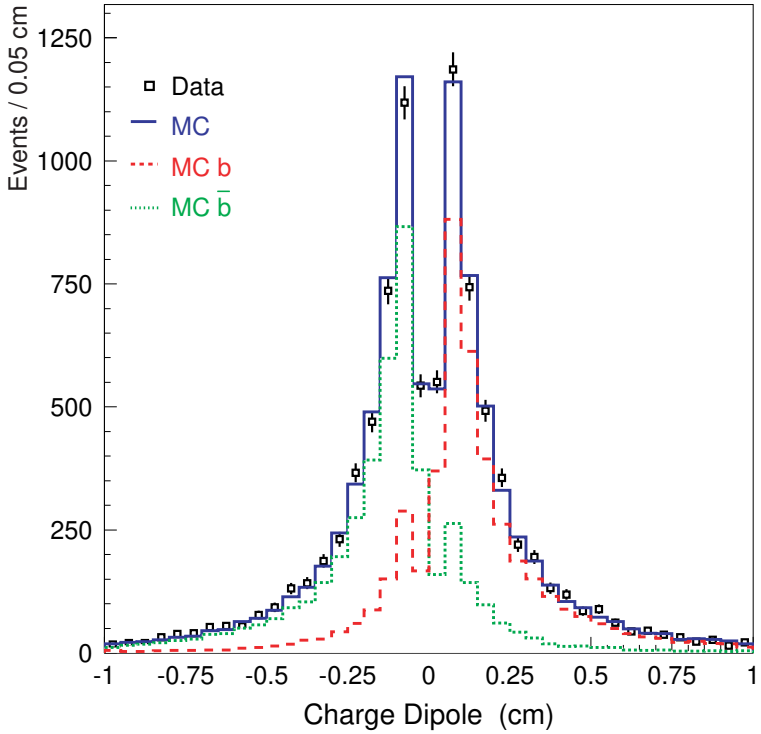

Figure 22: Distribution of the charge dipole for data (points) and Monte Carlo (solid histogram). Also shown are the contributions from b hadrons containing a b quark (dashed histogram) or a $\bar{b}$ quark (dotted histogram).

Table 12: Summary of relevant parameters for the B_s^0 mixing analyses

	D_s+Tracks	Lepton+D	Charge Dipole
No. decays	361	2087	8556
B_s^0 purity	38%	16%	15%
Production flavor mistag rate	25%	25%	22%
Decay flavor mistag rate	10%	4%	24%
σ_L (60% core Gaussian)	48 μm	55 μm	76 μm
σ_L (40% tail Gaussian)	152 μm	217 μm	311 μm
σ_p/p (60% core Gaussian)	0.08	0.06	0.07
σ_p/p (40% tail Gaussian)	0.19	0.18	0.21
Sensitivity	1.4 ps^{-1}	6.3 ps^{-1}	6.9 ps^{-1}
σ_A at Δm_s= 15 ps^{-1}	1.60	1.14	1.11

(representing approximately 20% of the selected sample) for which the method assigned the decay flavor randomly. In contrast, the mistag rate was estimated to be 12% for decays of the type $B_s^0 \to D_s^- X$, where X does not include any charm hadron.

In all the analyses, the sensitivity to B_s^0 oscillations was enhanced by evaluating the production and decay flavor mistag rates, and the decay length and momentum resolutions, an event-by-event basis.

6.5 Results

The study of the time dependence of B_s^0–$\overline{B}_s^0$ mixing utilized the amplitude method (75). Instead of fitting for Δm_s directly, the analysis was done at fixed values of Δm_s and a fit to the amplitude A of the oscillation was performed, i.e., in Equations 27 and 28, for the unmixed and mixed probabilities, the term $[1 \pm \cos(\Delta m_s t)]$ was replaced with $[1 \pm A\cos(\Delta m_s t)]$. This method is similar to Fourier transform analysis and has the advantage of facilitating the combination of results from different analyses and different experiments. One expects the amplitude to be consistent with $A = 0$ for values of the frequency sufficiently far from the true oscillation frequency, whereas the amplitude should peak at $A = 1$ at that frequency.

The D_s+tracks, lepton+D, and charge dipole analyses were combined, taking into account correlated systematic errors. Events shared by two or more analyses were only kept in the analysis with the highest sensitivity, thereby removing any statistical correlation between the

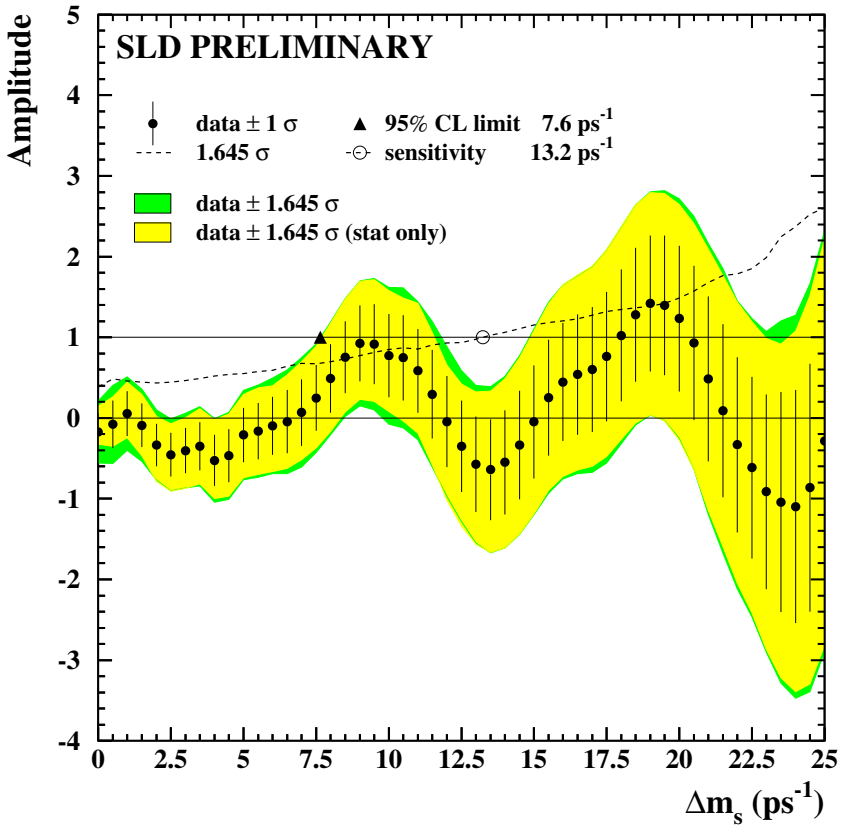

Figure 23: Measured amplitude as a function of Δm_s for the D_s+tracks, lepton+D, and charge dipole analyses combined.

analyses. The dominant contributions to the systematic error were found to be due to the uncertainties in the B_s^0 production rate, and the decay length and momentum resolutions, as well as the decay flavor tag in the case of the charge dipole analysis. Figure 23 shows the measured amplitude as a function of Δm_s for the combination. The measured values are consistent with $A = 0$ for the whole range of Δm_s up to 25 ps^{-1}, and no significant evidence is found for a preferred value of the oscillation frequency. The following ranges of B_s^0 oscillation frequencies are excluded at 95% CL: $\Delta m_s < 7.6\,\mathrm{ps}^{-1}$ and $11.8 < \Delta m_s < 14.8$ ps^{-1}, i.e., the condition $A + 1.645\,\sigma_A < 1$ is satisfied for those values. The combined sensitivity to set a 95% CL lower limit is found to be at a Δm_s value of 13.0 ps^{-1}, which corresponds to the frequency that satisfies $1.645\,\sigma_A = 1$. All results are preliminary.

The impact of the SLD analyses on the search for B_s^0 oscillations is apparent in Figure 24, which shows the uncertainty in the measured oscillation amplitude as a function of Δm_s for CDF, LEP, SLD, and the world average. The growth of σ_A with increasing Δm_s is due to the finite proper time resolution and clearly illustrates that the excellent proper time resolution for

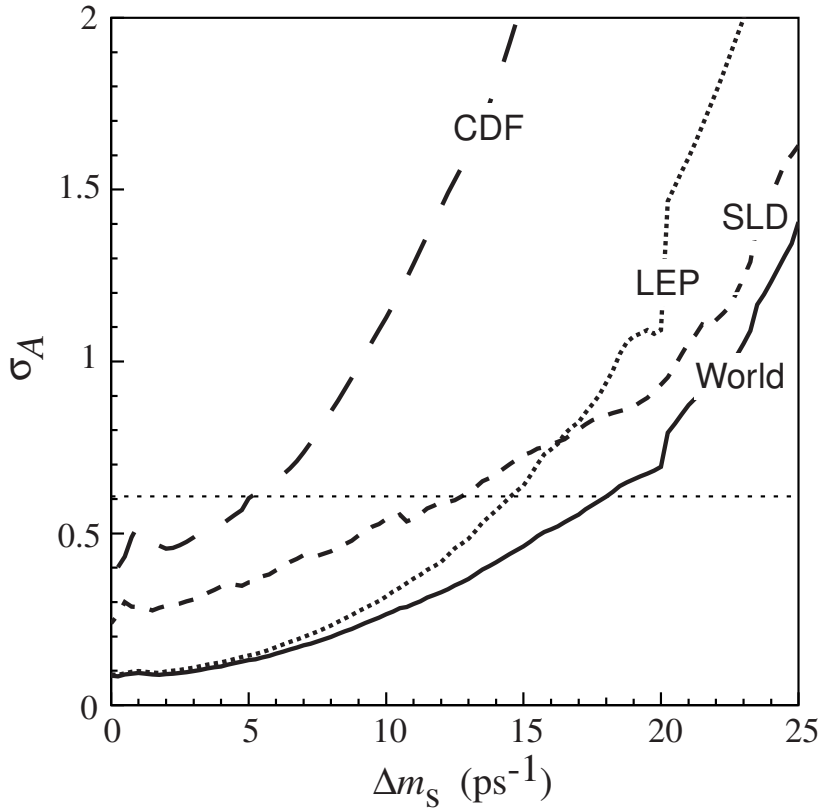

Figure 24: Amplitude uncertainty as a function of Δm_s for CDF, LEP, SLD, and the world average. The dashed horizontal line corresponds to the condition $1.645\,\sigma_A = 1$ used to define the 95% CL sensitivity.

SLD yields a smaller increase in uncertainty than in the case of LEP, for example. The SLD sensitivity of 13.0 ps^{-1} can be compared to the combined LEP sensitivity of 14.5 ps^{-1}, obtained with a data sample 30 times larger than that used by SLD.

7 INTERPRETATION OF RESULTS

7.1 B_s^0–$\overline{B}_s^0$ Mixing

As mentioned above, the study of B_s^0 oscillations is motivated by the fact that the oscillation frequencies Δm_d and Δm_s provide very powerful constraints on the weak quark mixing sector of the standard model in general, and on CP violation in particular. These constraints can be represented as circular bands centered around the point $(1, 0)$ in the $\bar{\rho}$-$\bar{\eta}$ plane (see Figure 25). Also shown are the constraints from measurements of the CP-violating parameter ϵ_K in the K^0–$\overline{K}^0$ system and the ratio of CKM elements $|V_{ub}/V_{cb}|$ measured in charmless B decays. The

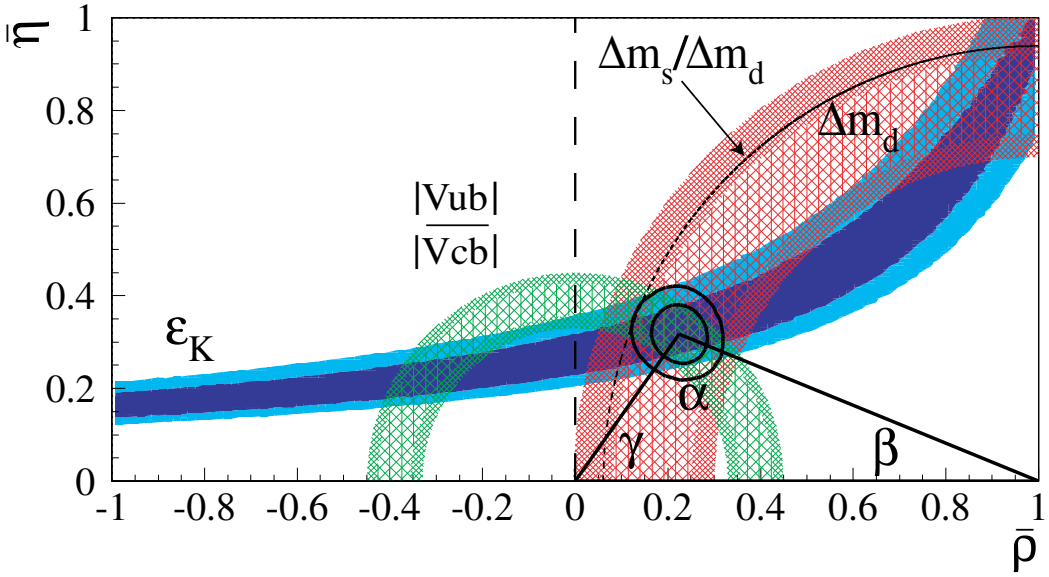

Figure 25: Constraints on the parameters $\bar{\rho}$ and $\bar{\eta}$ from the measurements of ϵ_K, $|V_{ub}/V_{cb}|$, Δm_d, and Δm_s. Figure extracted from Ciuchini et al (74).

combination of these constraints provides a measurement of the parameters ρ and η. These parameters correspond to the apex of the Unitarity Triangle (shown in Figure 25). The triangle represents one of the unitarity conditions that the CKM matrix must satisfy. A nonvanishing value of η implies the existence of CP violation, whereas the angles of the triangle are related to the single CP-violating phase of the CKM matrix.

A global fit within the context of the standard model yields $\bar{\rho} = 0.224 \pm 0.038$ and $\bar{\eta} = 0.317 \pm 0.040$ (74). The fit uses the entire B_s^0 oscillation amplitude spectrum rather than just the lower limit on Δm_s to incorporate information about the exclusion significance as a function of Δm_s. It should be noted that the treatment of errors in such a fit remains controversial because theoretical uncertainties dominate. Of special interest are the predictions for the CP-violating angles of the Unitarity Triangle α, β, and γ, which are currently the subject of intense experimental activity. The fit yields $\sin 2\beta = 0.698 \pm 0.066$, $\sin 2\alpha = -0.42 \pm 0.23$, and $\gamma = (54.8 \pm 6.2)^\circ$ (74). CP violation in B decays has now been unequivocally observed by the BaBar and Belle collaborations, with a world average value for $\sin 2\beta$ of 0.79 ± 0.10 (78), in good agreement with the above standard-model prediction. In the next few years, it is likely that we will learn the most from the combination of $\sin 2\beta$ and Δm_s measurements at the B factories and the Tevatron, since they provide orthogonal constraints on the Unitarity Triangle and are fairly clean theoretically and experimentally.

7.2 Electroweak – Quark Couplings

SLD measurements of R_b, R_c, A_b, A_c, and A_s are all in good agreement with the standard model. The SLD R_b measurement precision of ∼0.5% is in the interesting regime for testing the ∼1% level effect due to physics beyond the standard model through radiative corrections. The A_s measurement, showing good agreement with the A_b measurement, confirms quark coupling universality at the ±10% level. These measurements are also mostly in agreement with the measurements from LEP. In the case of A_b and A_c, the indirect measurements from LEP derived from $A_{\rm FB}^b$ and $A_{\rm FB}^c$ are both lower than the SLD average at the 1.3σ and 1.5σ levels, respectively. However, the derived LEP A_b, using the LEP and SLD combined A_ℓ for the initial state A_e, is by itself 3.1σ away from the standard model. This is essentially the same effect as the case of $A_{\rm FB}^b$ and $A_{\rm FB}^c$ measurements giving higher $\sin^2\theta_W^{\rm eff}$ values than other measurements when assuming universality in the fermions (see next subsection).

An interesting perspective on the interconnection between the measurements of A_ℓ, A_b, and $A_{\rm FB}^b$ is the $Zb\bar{b}$ vertex coupling analysis scheme from Takeuchi et al (79). Deviations $(\delta g_L^b, \delta g_R^b)$ from the standard model $Zb\bar{b}$ coupling can be transformed into a pair of variables (ξ_b, ζ_b) such that R_b deviations depend only on ξ_b and A_b deviations depend only on ζ_b. Particularly interesting is the relation between the parity violation type variable ζ_b and $\delta\sin^2\theta_W^{\rm eff}$, as shown in Figure 26. The consistency between the various measurements and the standard model is only at the 1.0% CL. The projection of the different bands on the horizontal line corresponding to $\zeta_b = 0$, i.e., assuming the standard-model $Zb\bar{b}$ coupling, illustrates the discrepancy in $\sin^2\theta_W^{\rm eff}$ between the values derived from A_ℓ and from $A_{\rm FB}^b$. The projection along the vertical line representing the measured $\sin^2\theta_W^{\rm eff}$ from A_ℓ illustrates the difference in A_b, comparing the direct measurement from SLD and the indirect measurement from $A_{\rm FB}^b$.

A general fit for the left- and right-handed $Zb\bar{b}$ and $Zc\bar{c}$ couplings was performed (80) in the context of the standard model (with $\sin^2\theta_W^{\rm eff}$ extracted from the world average A_ℓ) using the R_b, R_c, A_b, A_c, $A_{\rm FB}^b$, and $A_{\rm FB}^c$ measurements. Table 13 summarizes the results of the fit and the corresponding standard model predictions. These results are also illustrated in Figure 27. There is generally good agreement between the measurements and the standard model for the $Zc\bar{c}$ coupling at the current precision level. The apparent departure of the $Zb\bar{b}$ coupling from the standard model, driven primarily by the LEP $A_{\rm FB}^b$ measurements, is mainly affecting the right-handed coupling value. This is particularly difficult to accommodate because no known model can produce a deviation from the standard model at this level. The direct measurement of A_b from SLD provides an important constraint on a possible $Zb\bar{b}$ coupling anomaly, which has

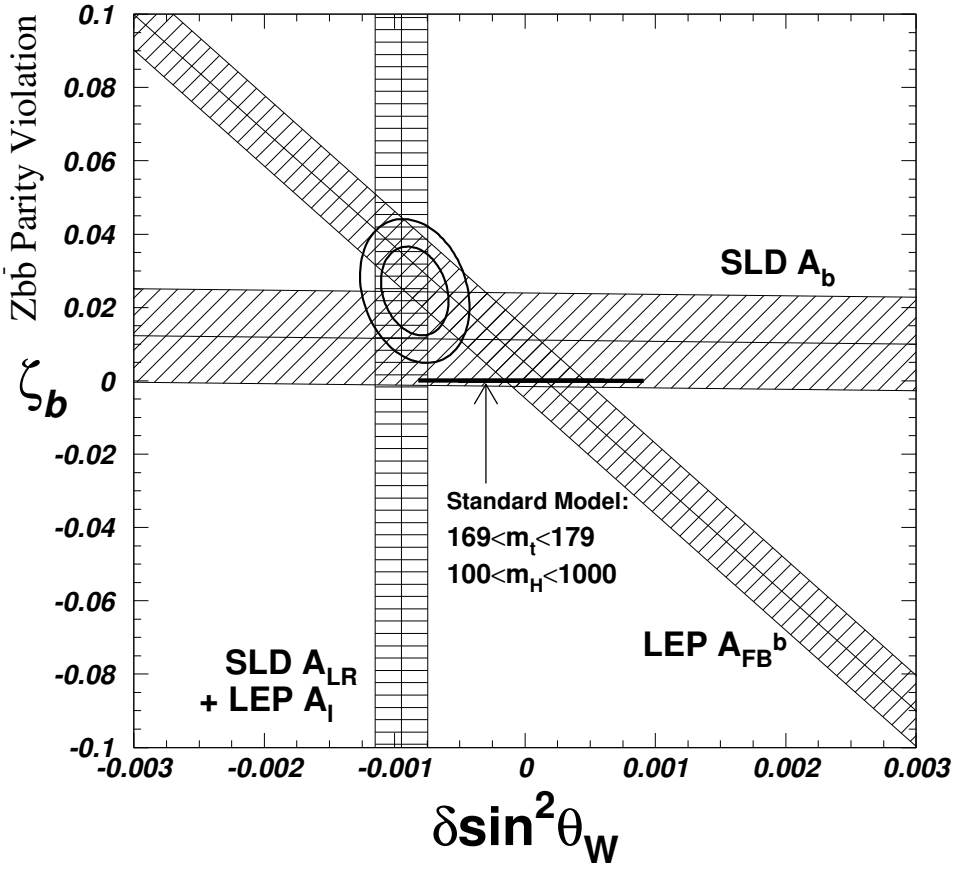

Figure 26: The $Zb\bar{b}$ coupling analysis result following Takeuchi et al. The standard-model point at (0,0) is defined by m_t=174 GeV, m_H=300 GeV, α_s=0.119, and α=1/128.905. The thin horizontal band around (0,0) corresponds to the standard model m_t and m_H variations indicated in the plot. The error ellipses represent 68% and 95% CL contours for the fit.

relevance to the validity of setting constraints on the Higgs mass from measurements of $A_{\rm FB}^b$, as is discussed next.

Table 13: Left- and right-handed $Zb\bar{b}$ and $Zc\bar{c}$ couplings determined from a fit to SLD and LEP measurements; the standard model (SM) prediction is also provided

Coupling constant	Fit result	SM prediction
g_L^b	-0.4183 ± 0.0015	-0.4211
g_R^b	-0.0962 ± 0.0064	-0.0774
g_L^c	0.3443 ± 0.0037	0.3467
g_R^c	0.1600 ± 0.0048	0.1548

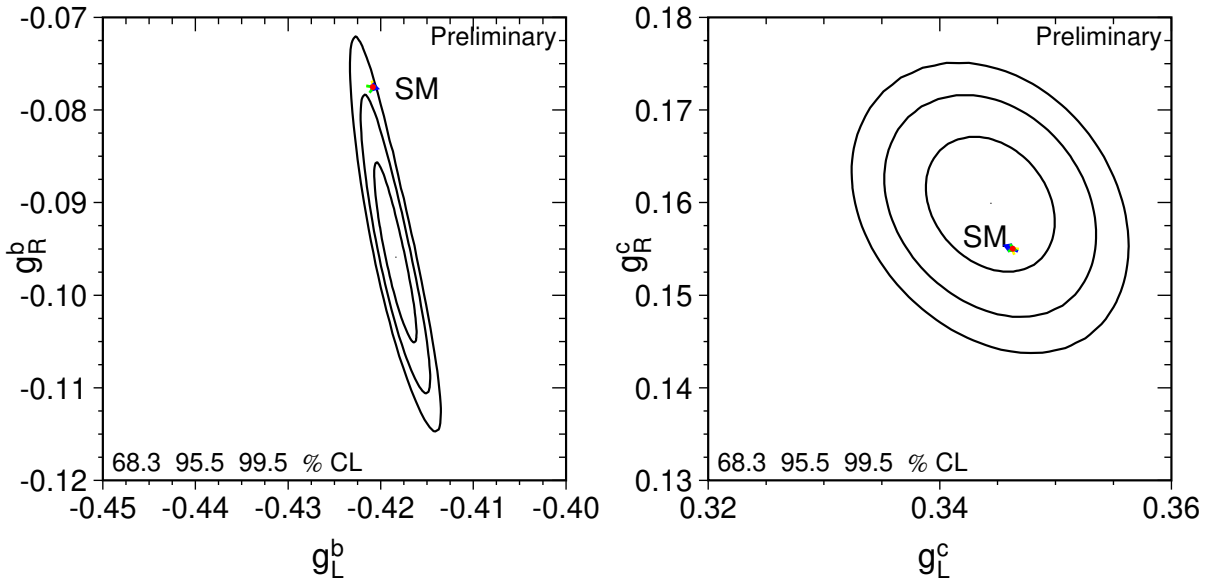

Figure 27: Left- and right-handed $Zb\bar{b}$ and $Zc\bar{c}$ couplings combining measurements from SLD and LEP. The standard model (SM) predictions are also shown with small arrows indicating the effect of the uncertainty in the top quark mass.

7.3 Electroweak – Lepton Couplings

The SLD measurement of $\sin^2\theta^{\rm eff}_W$, precise and statistics-dominated, represents a benchmark for determinations of the weak mixing angle. What do we learn from this result? We must first examine its consistency with the standard model. We have discussed the role of radiative effects and noted that the measured top mass agrees with theoretical constraints at the level of about 7 ± 10 GeV (a relative $4 \pm 6\%$). Now only one standard-model parameter remains undetermined (although direct experimental constraints exist)—the Higgs boson mass m_H. Because of radiative effects on the gauge boson propagators, corrections due to the Higgs boson are expected to contribute logarithmically in m_H, and hence sensitivity to this parameter is marginal.

7.3.1 Higgs Mass Constraints

Nevertheless, the SLD measurement error is small enough that a meaningful constraint is available from this measurement alone. The sensitivity of an observable Ω to m_H can be quantified by the normalized partial derivative $\frac{1}{\delta\Omega}\frac{\partial\Omega}{\partial log_{10}(m_H/\mathrm{GeV})}$, where $\delta\Omega$ is the total uncertainty in Ω. The value of this metric for the SLD $\sin^2\theta^{\rm eff}_W$ measurement, at 4.4, is larger than any other presently available electroweak result [closest are the forward-backward b quark asymmetry results from LEP (3.9) and the W boson mass result from LEP-II (3.7)]. Figure 28*a* illustrates the depen-

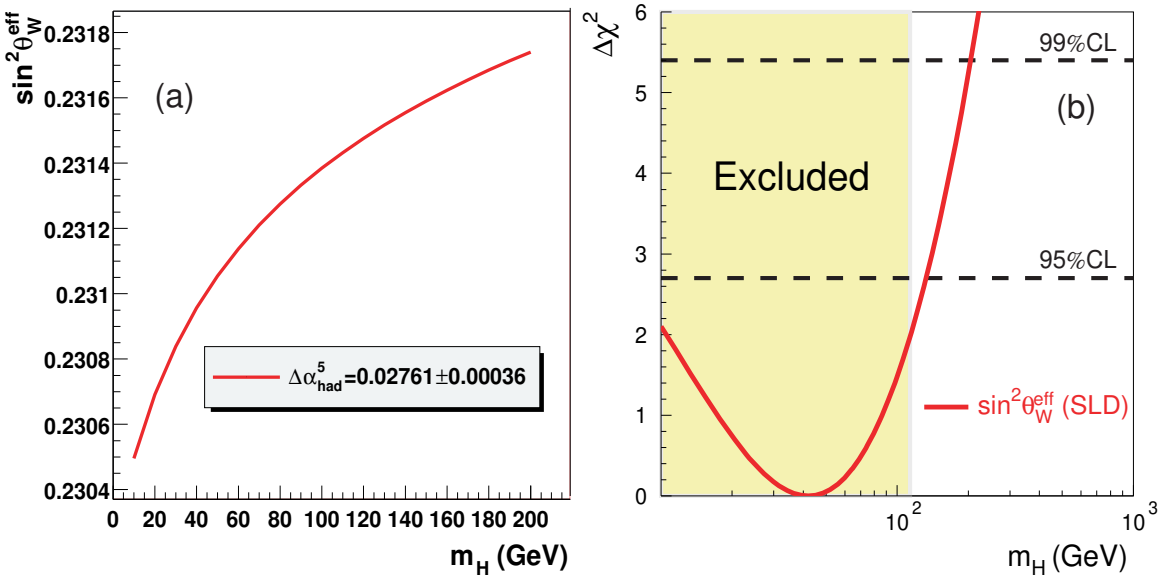

Figure 28: (*a*) Leading-order radiative effects on $\sin^2\theta_W^{\rm eff}$ as a function of the Higgs boson mass. (*b*) Change in χ^2 curve for a fit to the Higgs mass using the SLD $\sin^2\theta_W^{\rm eff}$ result.

dence of $\sin^2\theta_W^{\rm eff}$ on the Higgs mass. From this figure it is apparent that the SLD $\sin^2\theta_W^{\rm eff}$ result of 0.23097 prefers a low Higgs mass, and that mass constraints set in this region benefit from the steeper slope of the curve. The largest uncertainty in these standard-model calculations is due to the present top quark mass error of 5.1 GeV, equivalent to $\delta\sin^2\theta_W^{\rm eff} \approx \pm 0.00016$. In addition, an ambiguity in the determination of the standard-model Higgs boson mass arises from uncertainties in the evolution of the fine structure constant from low Q^2 to its value at the Z^0 scale, $\alpha(M_Z^2)$. This uncertainty stems from the need to use low-energy e^+e^- annihilation cross-section data in the calculation of hadronic loop effects. Recent data from the Beijing Electron Synchrotron (BES) e^+e^- experiment (81) have led to improved errors, which presently correspond to an uncertainty in $\sin^2\theta_W^{\rm eff}$ of about ± 0.0001 (82). However, a number of evaluations of $\alpha(M_Z^2)$ are in common use, leading to variations in $\sin^2\theta_W^{\rm eff}$ predictions over a range of ~ 0.00015, and an associated range in quoted Higgs boson mass limits. The choice of $\alpha(M_Z^2)$ used throughout this review is due to Burkhardt and Pietrzyk (82).

We perform a χ^2 fit to the standard model by including at least one electroweak observable, along with the fit parameters: m_H, M_Z measured at LEP, m_t measured at Fermilab, $\alpha(M_Z^2)$, and the strong coupling constant α_s (the Fermi constant G_F is held fixed). With the SLD $\sin^2\theta_W^{\rm eff}$ result as the sole electroweak observable included in the fit, Figure 28*b* gives the results in the form of a Higgs mass χ^2. The resulting one-sided confidence upper limits from the fit are

$m_H < 133$ GeV (95% CL) and < 205 GeV (99% CL). Also shown is the current direct search lower limit from LEP-II of 114.1 GeV. These direct and indirect Higgs bounds are in modest agreement: the value of the one-sided confidence limit at 114.1 GeV corresponds to a probability of 7%.

As we have seen, the SLD data are consistent with lepton universality. Measurements at LEP of $A_{\rm FB}^{\ell}$, and of $\tau^{\pm}$ polarization (which separately provides A_e and A_τ), confirm lepton universality as well. All available A_ℓ data, expressed in terms of $\sin^2\theta_W^{\rm eff}$, are consistent (see Figure 29). Also shown are the LEP $\sin^2\theta_W^{\rm eff}$ results deriving from quark asymmetries, which, taken together, provide an average (0.23230 ± 0.00029) that is 3.3σ different from the lepton asymmetries average (0.23113 ± 0.00021). Unresolved issues in the $Zb\bar{b}$ coupling data were discussed in the previous section. The χ^2 for the overall $\sin^2\theta_W^{\rm eff}$ combination has a probability of 2.5%. The quark asymmetry average is dominated by the $A_{\rm FB}^{b}$ measurement, the most precise $\sin^2\theta_W^{\rm eff}$ determination at LEP.

Fits are made to worldwide electroweak results (3), including all SLD and LEP measurements, LEP-II and Tevatron M_W results, deep inelastic neutrino scattering data, and measurements of atomic parity violation in cesium and thallium (83). Among these, the most sensitive to m_H are, in order of decreasing sensitivity, the asymmetries, M_W, and the Z^0 total width Γ_Z. With the exception of the $A_{\rm FB}^{b}$ data mentioned above, all of these measurements agree satisfactorily and favor a light Higgs boson. Figure 30 shows the individual contributions to the overall fit broken down into SLD, LEP leptonic, and LEP hadronic contributions to $\sin^2\theta_W^{\rm eff}$, the world M_W average, and all other electroweak results (dominated by Γ_Z). Including all data results in limits of $m_H < 195$ GeV (95% CL) and < 260 GeV (99% CL), in agreement with the direct lower Higgs mass limit at 114.1 GeV. The χ^2 per degree of freedom for this fit is 23.5/16, corresponding to a probability of 10%. Excluding the $A_{\rm FB}^{b}$ result from the fit increases the χ^2 probability to 47% and substantially tightens the Higgs mass limits to $m_H < 133$ GeV (95% CL) and < 185 GeV (99% CL). The confidence level of this restricted fit at the value of the direct lower Higgs mass limit is 9%. Within the context of the standard model, the electroweak data are suggesting that the Higgs boson is relatively light and is in the region expected by supersymmetric extensions of the standard model (84). Although these constraints are not model-independent, they do significantly restrict possible new physics, even if the Higgs mass limits are evaded (85).

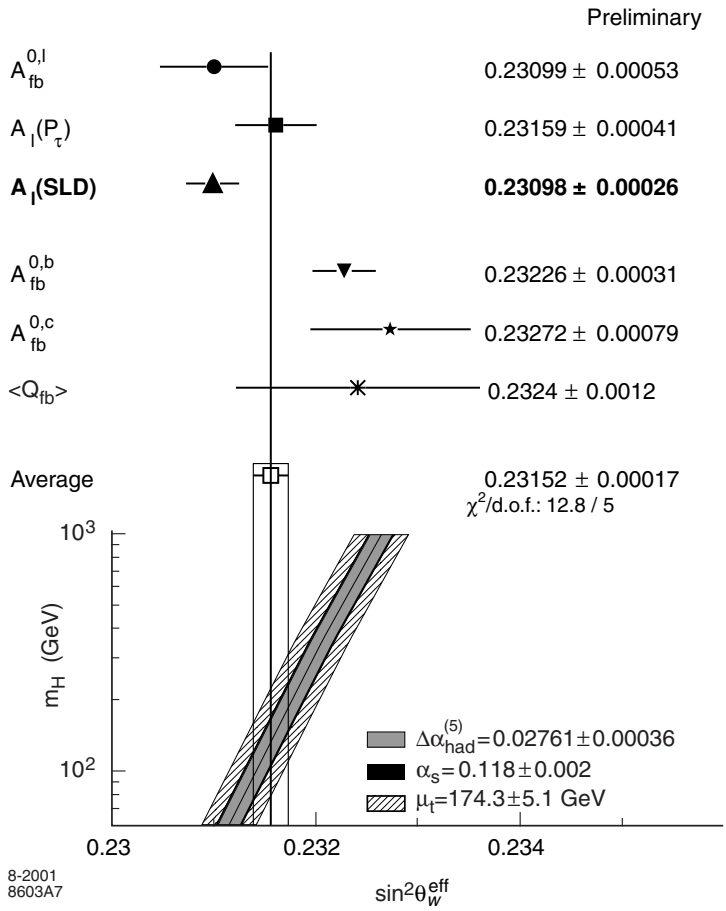

Figure 29: SLD and LEP $\sin^2\theta_W^{\rm eff}$ results. The first three results are based on lepton asymmetries including the SLD result, the last three results on b-quark, c-quark, and hadronic-event asymmetries are based on measurements at LEP.

7.3.2 Extensions of the Standard Model: The S, T, and U Parameters

It is desirable to consider the electroweak data in a more general context than the standard model. The framework of our analysis will follow Lynn et al. (86), who made the following assumptions:

- The gauge group of electroweak physics is $SU(2)_L \times U(1)$ (Z, Z' mixing, for example, is not incorporated).
- The symmetry-breaking sector has a global $SU(2)$ "custodial" symmetry that insures $\rho = M_W^2/M_Z^2\cos^2\theta_W = 1 + \mathcal{O}(\alpha)$.
- Vacuum polarization effects dominate compared to vertex and box corrections (the oblique hypothesis).

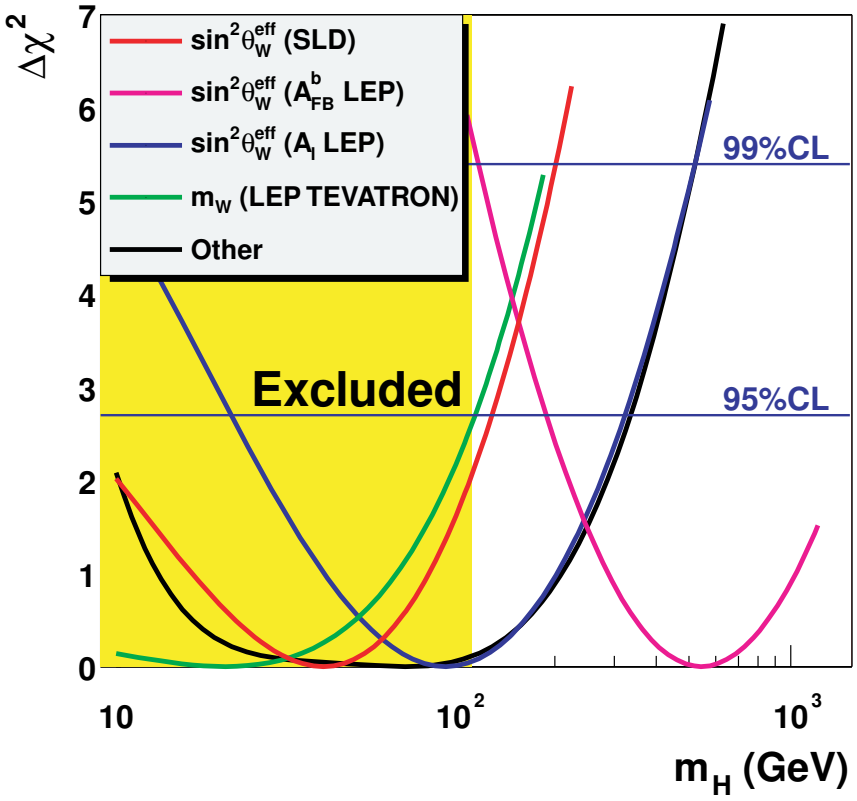

Figure 30: Change in χ^2 as a function of the Higgs mass for various measurements separately. "Other" refers here to all the other electroweak measurements included in our global fit.

- Any new particles are heavy, so that Taylor expansions are appropriate descriptions of the vacuum polarization corrections.

With these assumptions, the total number of independent gauge boson correction terms is six. Using the three precision constants (G_F, M_Z, and α), this leaves three undetermined parameters, which are denoted S, T, and U in the scheme of Peskin & Takeuchi (87). The S parameter is a measure of the weak isospin-conserving new heavy sector. The T parameter is equal to $\alpha^{-1}\Delta\rho$ and is a measure of weak isospin breaking in the heavy sector (for example, the top quark to bottom quark mass splitting). The U parameter introduces small effects, is only relevant for the observable M_W, and is ignored here. A heavy fermion doublet changes the T parameter, which is quadratic in the mass splitting. The standard-model Higgs boson contributes offsets that are logarithmic in the Higgs mass for both S and T, though these effects are opposite in sign.

We performed a fit to the electroweak data, where offsets from S and T = 0 were relative to a reference value of the top quark and Higgs masses, which we chose to be 175 GeV and 100 GeV, respectively. Figure 31 gives the result.

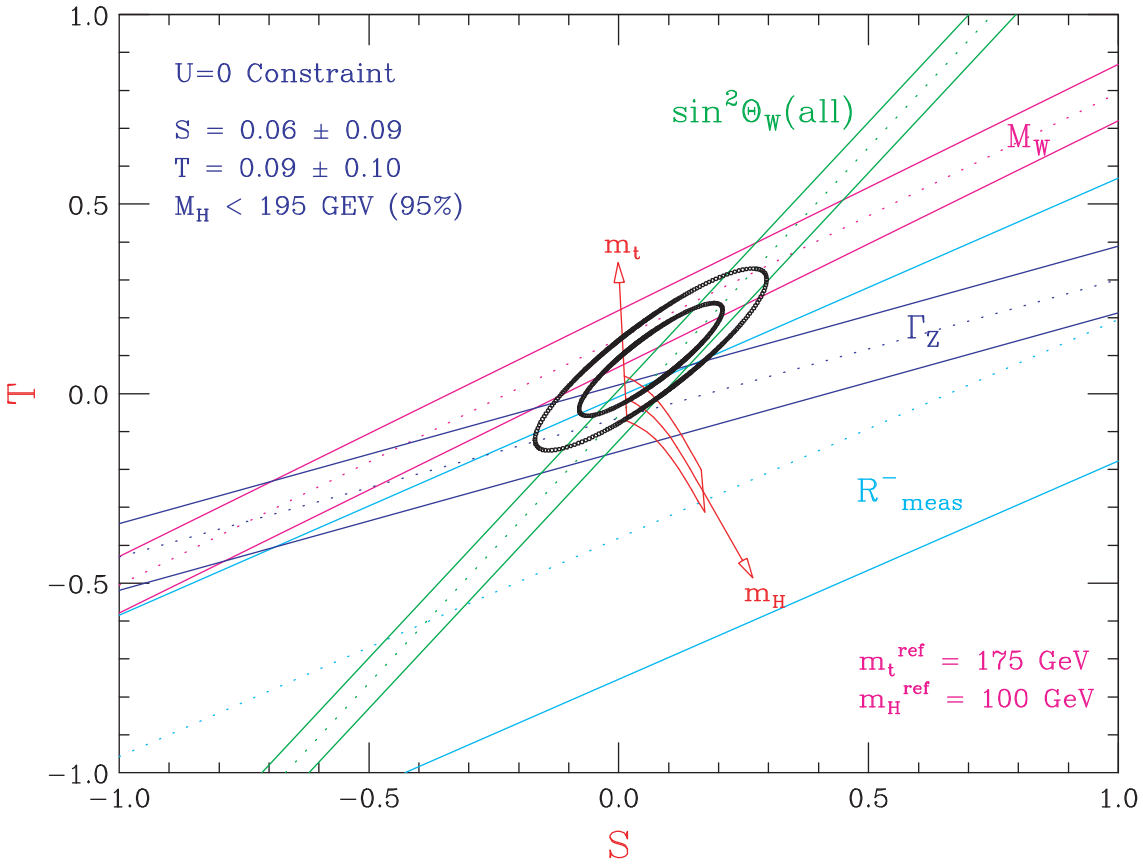

Figure 31: Global electroweak fit in the S and T plane. The ellipses correspond to the 68% and 90% CL contours of the global fit. Four of the contributors to the fit are shown as $\pm 1\sigma$ bands.

The fit ellipse (68% CL and 90% CL contours are shown) is consistent with the banana-shaped region of the S-T plane allowed by the standard model, so long as the Higgs mass is small. The fit result is presently consistent with S and T = 0. Also shown are the $\pm 1\sigma$ constraints for four representative electroweak observables: $\sin^2\theta_W^{\rm eff}$, M_W, Γ_Z, and R^- (from neutrino deep-inelastic scattering), which appear as bands with different slopes. At the present level of precision in the global electroweak data, the S-T analysis has excluded a subclass of the models that propose strong symmetry breaking mechanisms [conventional "technicolor" models (88)] that predict significant deviations from S = 0. The S-T analysis is beginning to probe hypothetical extensions of the standard model, such as supersymmetry. For example, the region of the S-T plane allowed by the minimal supersymmetric model (MSSM) overlaps the light Higgs end of the standard-model zone but also includes larger deviations from T = 0. Some authors have already explored how the precision electroweak data constrain the free parameters of the MSSM (89).

8 CONCLUSIONS

We have reviewed highlights of the Z^0-pole physics program carried out by the SLD collaboration at the SLC. The combination of beam polarization, small beam sizes, and a CCD pixel vertex detector has led to a series of measurements that complement those performed at Fermilab and CERN and that have probed the standard model and its extensions. Many of these measurements provide unique insight into the physics of fundamental interactions. In addition, the novel techniques developed for these measurements have applicability to future colliding beam experiments.

An important result of the precision electroweak program at SLD is that a standard-model Higgs boson, if it exists, should be relatively light. This conclusion is also supported by a fit to the complete set of worldwide precision electroweak data. In particular, these fits indicate that the Higgs boson may be within reach of the Tevatron experiments at Fermilab in the next several years. If the Higgs boson eludes the Tevatron experiments, a much greater reach is expected once the CERN LHC program begins in about 2006. Also important are the SLD electroweak measurements performed with individual lepton and quark flavors. This diverse set of measurements clearly illustrates the versatility of the powerful flavor-separation methods available to an experiment at a linear collider. Finally, studies of B_s^0–$\overline{B}_s^0$ mixing at SLD have contributed significantly to the worldwide effort to constrain the quark mixing matrix and CP violation in the standard model. These played an important role, complementary to the CP violation measurements currently under way.

Looking a bit further ahead, high-energy ($\sim$500 GeV and up) linear collider projects are presently under consideration in the United States, Germany, and Japan. These new collider projects would build on the experience gained from the construction and operation of the SLC and SLD, as well as from the physics results and techniques developed there.

ACKNOWLEDGMENTS

We would like to thank our SLD colleagues for their contributions and for making the collaboration an enjoyable and stimulating environment to work in. We also wish to thank the SLC accelerator physicists and operations personnel for their efforts.

Literature Cited

1. Glashow SL. *Nucl. Phys.* B22:579 (1961); Weinberg S. *Phys. Rev. Lett.* 19:1264 (1967); Salam A. In *Elementary Particle Theory*, ed. N Svartholm, p. 367. Stockholm: Almquist and Wiksell (1968).
2. Langacker P. In *Proc. XXIV Int. Conf. High Energy Phys., Munich, Germany, August 1988*. Berlin, Germany: Springer-Verlag (1988)
3. LEP Collaborations ALEPH, DELPHI, L3, OPAL with LEP Electroweak Working Group and SLD Heavy Flavor and Electroweak Groups. *A Combination of Preliminary Electroweak Measurements and Constraints on the Standard Model*, LEPEWWG/2001-01 (2001)
4. Abe F, et al (CDF Collaboration). *Phys. Rev. Lett.* 73:225 (1994); Abe F, et al (CDF Collaboration). *Phys. Rev. Lett.* 74:2626 (1995); Abachi S, et al (D0 Collaboration). *Phys. Rev. Lett.* 74:2632 (1995); Abachi S, et al (D0 Collaboration). *Phys. Rev. Lett.* 79:1197 (1997); Abe F, et al (CDF Collaboration). *Phys. Rev. Lett.* 79:1992 (1997); Abbott B, et al (D0 Collaboration). *Phys. Rev. Lett.* 80:2063 (1998); Abbott B, et al (D0 Collaboration). *Phys. Rev. D* 58:052001 (1998); Abe F, et al (CDF Collaboration). *Phys. Rev. Lett.* 82:271 (1999); Abbott B, et al (D0 Collaboration). *Phys. Rev. D* 60:052001 (1999); Affolder T, et al (CDF Collaboration). *Phys. Rev. D* 63:032003 (2001)
5. ALEPH, DELPHI, L3, and OPAL Collaborations. *Search for the Standard Model Higgs Boson at LEP*, CERN-EP/2001-055 (2001)
6. Cabibbo N. *Phys. Rev. Lett.* 10:531 (1963); Kobayashi M, Maskawa T. *Prog. Theor. Phys.* 49:652 (1973)
7. Abe K, et al (SLD Collaboration). *Phys. Rev. D* 52:4828 (1995); *Phys. Rev. Lett.* 78:4691 (1997)
8. Abe K, et al (SLD Collaboration). *Phys. Rev. Lett.* 71:2528 (1993); *Phys. Rev. Lett.* 72:3145 (1994); *Phys. Rev. D* 50:5580 (1994); *Phys. Rev. Lett.* 74:1512 (1995); *Phys. Rev. D* 51:962 (1995); *Phys. Rev. D* 52:4240 (1995); *Phys. Rev. Lett.* 75:4173 (1995); *Phys. Rev. D* 53:2271 (1996); *Phys. Lett.* B371:149 (1996); *Phys. Rev. Lett.* 76:4886 (1996); *Phys. Rev. D* 55:2533 (1997); *Phys. Lett.* B386:475 (1996); *Phys. Rev. Lett.* 78:3442 (1997); *Phys. Rev. D* 56:5310 (1997); *Phys. Rev. D* 59:012002 (1999); *Phys. Rev. D* 59:052001 (1999); *Phys. Rev. D* 60:092002 (1999); *Phys. Rev. Lett.* 84:4300 (2000); *Phys. Rev. Lett.* 86:962 (2001); *Phys. Lett.* B507:61 (2001)
9. Abrams GS, et al (Mark II Collaboration). *Phys. Rev. Lett.* 63:724 (1989)
10. Seeman JT. *Annu. Rev. Nucl. Part. Sci.* 41:389 (1991)
11. Phinney N. In *Proc. XX Int. Conf. Linac 2000, Monterey, CA*. Stanford: SLAC (2000)
12. Alley R, et al. *Nucl. Instr. Methods A* 365:1 (1995)
13. Maruyama T, Garwin EL, Prepost R, Zapalac GH. *Phys. Rev. B* 46:4261 (1992); Nakanishi et al. *Phys. Lett.* A158:345 (1991)
14. Levi ME, et al. SLAC-PUB-4921, LBL-26976 (1989); Kent J, et al. SLAC-PUB-4922, LBL-26977 (1989)
15. SLD Collaboration. SLAC-Report-273 (1984)
16. Axen D, et al. *Nucl. Instr. Methods A* 328:472 (1993)
17. Benvenuti AC, et al. *Nucl. Instr. Methods A* 276:94 (1989); 290:353 (1990)
18. Berridge SC, et al. *IEEE Trans. Nucl. Sci.* 39:1242 (1992)
19. Fero MJ, et al. *Nucl. Instr. Methods A* 367:111 (1995)

20. Agnew GD, et al. In *Proc. XXVI Int. Conf. High Energy Phys., Dallas, 1992,* Vol. 2, p. 1862. New York: World Scientific (1992)
21. Abe K, et al. *Nucl. Instr. Methods A* 400:287 (1997)
22. Kalman RE. Trans. ASME J. Basic Eng. March:35–45 (1960)
23. Abe K, et al. *Nucl. Instr. Methods A* 343:74 (1994); Va'vra J. *Nucl. Instr. Methods A* 433:59 (1999)
24. Nelson WR, Hirayama H, Rogers DWO. SLAC-Report-265 (1985)
25. Torrence EC. Ph.D thesis, SLAC-Report-509, p.191-213 (1997)
26. Field RC, Frey R, Woods M, Arodzero A, Zhou J. *IEEE Trans. Nucl. Sci.* 45:670 (1998); Berridge SC, et al. In *Proc. XIII Annual Symp. High Energy Spin Phys., Protvino, Russia,* p. 534 (1998); Onoprienko DV. Ph.D. thesis, SLAC-Report-556, p.53-100 (2000)
27. Swartz ML. *Phys. Rev. D* 014010:58 (1998)
28. Swartz ML, et al. *Nucl. Instr. Methods A* 363:526 (1995)
29. Mulhollan G, et al. SLAC-PUB-7325 (1996)
30. Limberg T, Emma P, Rossmanith R. SLAC-PUB-6210 (1993)
31. Sjöstrand T, et al. *Comput. Phys. Commun.* 82:74 (1994)
32. GEANT 3.21 Program, CERN Application Software Group, CERN Program Library (1993)
33. Jackson DJ. *Nucl. Instr. Methods A* 388:247 (1998)
34. Braunschweig W, et al (TASSO Collaboration). *Z. Phys. C* 38:543 (1988)
35. Abe K, et al (SLD Collaboration). *Phys. Rev. Lett.* 70:2515 (1993); Abe K, et al (SLD Collaboration). *Phys. Rev. Lett.* 73:25 (1994); Abe K, et al (SLD Collaboration). *Phys. Rev. Lett.* 78:2075 (1997); Abe K, et al (SLD Collaboration). *Phys. Rev. Lett.* 84:5945 (2000)
36. Detailed information is available in the following Ph.D. theses: Park H. SLAC-Report-435 (1993); Elia RD. SLAC-Report-429 (1994); Ben-David RJ. Yale U.(UMI-94-33702-mc) (1994); King RC. SLAC-Report-452 (1994); Lath A. SLAC-Report-454 (1994); Torrence EC. SLAC-Report-509 (1997); Onoprienko DV. SLAC-Report-556 (2000)
37. Bardin D, et al. DESY 99-070 (1999)
38. Onoprienko DV. Ph.D. thesis, SLAC-Report-556, p.25-31 (2000)
39. Elia RD. Ph.D. thesis, SLAC-Report-429, p.123-126 (1994)
40. Band HR, Rowson PC, Wright TR. internal memo, SLD-note 268 (2000) http://www-sldnt.slac.stanford.edu/sldbb/SLDNotes/sld-note%20268.pdf
41. Abe K, et al (SLD Collaboration). *Phys. Rev. Lett.* 79:804 (1997)
42. Abe K, et al (SLD Collaboration). *Phys. Rev. Lett.* 86:1162 (2001)
43. Akhundov A, Bardin D, Riemann T. *Nucl. Phys.* B276:1 (1986); Beenakker W, Hollik W. *Z. Phys. C* 40:141 (1988); Lynn BW, Stuart RG. *Phys. Lett.* B252:676 (1990); Bernabéu J, Pich A, Santamaría A. *Phys. Lett.* B363:326 (1991)
44. Hollik W. *Mod. Phys. Lett.* A5:1909 (1990); Boudjema F, Djouadi A, Verzegnassi C. *Phys. Lett.* B238:423 (1990); Djouadi A, et al. *Nucl. Phys.* B349:48 (1991); Boulware M, Finnel D. *Phys. Rev. D* 44:2054 (1991)
45. Hildreth MD. In *Proc. XXXI Rencontres de Moriond "Electroweak Interactions and Unified Theories"*. Gif-sur-Yvette: Ed. Frontieres (1996)

46. de Groot N. Presented at XXXVI Rencontres de Moriond, "Electroweak Interactions and Unified Theories," Mar. 2001, Les Arcs, France; Serbo V. Presented at Int. Europhys. Conf. High Energy Phys., July 2001, Budapest, Hungary
47. Abe K, et al (SLD Collaboration). *Phys. Rev. Lett.* 80:660 (1998)
48. LEP Electroweak Working Group. Summer-2000 summary CERN-EP-2001-021 (hep-ex/0103048) and references therein. Updates for Winter 2001 can be found at http://lepewwg.web.cern.ch/LEPEWWG/plots/winter2001/
49. Abe K, et al (SLD Collaboration). SLAC-PUB-7880. Contrib. paper to Int. Conf. High Energy Phys., 29th, Vancouver, Canada, Aug. 1998
50. Abe K, et al (SLD Collaboration). SLAC-PUB-8951, to be submitted to Phys. Rev. Lett.
51. Abe K, et al (SLD Collaboration). *Phys. Rev. Lett.* 83:3384 (1999)
52. Abe K, et al (SLD Collaboration). *Phys. Rev. Lett.* 81:942 (1998)
53. Abe K, et al (SLD Collaboration). *Phys. Rev. D* 63:032005 (2001)
54. Abe K, et al (SLD Collaboration). SLAC-PUB-8201, SLAC-PUB-8200, SLAC-PUB-8199. Contributed papers to Eur. Phys. Soc. HEP-1999 Conf., Tampere, Findland, July 1999
55. Abe K, et al (SLD Collaboration). *Phys. Rev. Lett.* 83:1902 (1999)
56. Stav JB, Olsen HA. *Phys. Rev. D* 52:1359 (1995); *Phys. Rev. D* 50:6775 (1994)
57. Abbaneo D, et al. *Eur. Phys. J.* C4:2 (1998)
58. Abe K, et al (SLD Collaboration). *Phys. Rev. Lett.* 85:5059 (2000)
59. Abe K, et al (SLD Collaboration). *Phys. Rev. Lett.* 75:3624 (1995)
60. Abe K, et al (SLD Collaboration). *Phys. Rev. Lett.* 79:590 (1997)
61. Abe K, et al (SLD Collaboration). SLAC-PUB-8206 (1999)
62. Bigi II, et al. In *B Decays,* ed. S Stone, p. 132. New York: World Sci. (1994)
63. Neubert M, Sachrajda CT. *Nucl. Phys.* B483:339 (1997)
64. Abe K, et al (SLD Collaboration). *Phys. Rev. D* 62:071101 (2000)
65. Abe K, et al (SLD Collaboration). SLAC-PUB-7896 (1998)
66. Chou AS (SLD Collaboration). SLAC-PUB-8686 (2000)
67. Thom J (SLD Collaboration). To appear in *Proc. Int. Europhys. Conf. High Energy Phys., Budapest, Hungary, July 2001*
68. Buras AJ, Slominski W, Steger H. *Nucl. Phys.* B345:369 (1984)
69. Inami T, Lim CS. *Prog. Theor. Phys.* 65:297 (1981)
70. Gay C. *Annu. Rev. Nucl. Part. Sci.* 50:577 (2000)
71. Groom DE, et al (Particle Data Group). *Eur. Phys. J.* C15:1 (2000)
72. Bernard C. *Nucl. Phys. Proc. Suppl.* 94:159 (2001)
73. Wolfenstein L. *Phys. Rev. Lett.* 51:1945 (1984)
74. Ciuchini M, et al. *JHEP* 0107:013 (2001)
75. Moser HG, Roussarie A. *Nucl. Instr. Methods A* 384:491 (1997)
76. Abe K, et al (SLD Collaboration). SLAC-PUB-8598 (2000)
77. Abe K, et al (SLD Collaboration). SLAC-PUB-8568 (2000)

78. Aubert B, et al (BABAR Collaboration). *Phys. Rev. Lett.* 87:091801 (2001); Abe K, et al (BELLE Collaboration). *Phys. Rev. Lett.* 87:091802 (2001); Affolder T, et al (CDF Collaboration). *Phys. Rev. D* 61:072005 (2000); Barate R, et al (ALEPH Collaboration). *Phys. Lett.* B492:259 (2000); Ackerstaff K, et al (OPAL Collaboration). *Eur. Phys. J.* C5:379 (1998)
79. Takeuchi T, Grant AK, Rosner JL. hep-ph/9409211; also in *Proc. DPF 1994 Conf., Albuquerque, NM, August 1994*, River Edge, NJ: World Scientific (1995)
80. Grünewald M and the LEP Electroweak Working Group. Private communication. See also http://lepewwg.web.cern.ch/LEPEWWG/
81. Bai JZ, et al (BES Collaboration). hep-ex/0102003;Bai JZ, et al. *Phys. Rev. Lett.* 84:594 (2000)
82. Burkhardt H, Pietrzyk B, LAPP-EXP-2001-03 (2001)
83. The central value and error for the cesium result used in the fit is adjusted in accordance with Kozlov MG, Porsev SG, Tupitsyn II. *Phys. Rev. Lett.* 86:3260 (2001); additional information regarding a controversy in the interpretation of the experimental result is discussed in Derevianko A. *Phys. Rev. Lett.* 85:1618 (2000)
84. For an overview of the MSSM and related models, see Gunion JF, Haber HE, Kane G, Dawson S. *The Higgs Hunter's Guide*. Redwood City, CA: Addison-Wesley (1990)
85. Peskin M, Wells JD. SLAC-PUB-8763 (2001)
86. Lynn B, Peskin M, Stuart R. SLAC-PUB-3725 (1985)
87. Peskin M, Takeuchi T. *Phys. Rev. Lett.* 65:964 (1990)
88. Weinberg S. *Phys. Rev. D* 19:1277 (1979); Susskind L. *Phys. Rev. D* 20:2619 (1979)
89. See for example, Erler J, Pierce D. *Nucl. Phys.* B526:53 (1998)